Investigation of pelvic bone fracture mechanism and simulated treatment

by

Mohammad Salem

A thesis submitted in partial fulfillment of the requirements for the degree of

Doctor of Philosophy

Department of Mechanical Engineering
University of Alberta

Abstract

The pelvic bone is one of most stressed bones in the human body due to its essential task of weight-bearing of upper body. However, pelvic bone fractures usually occur as a result of high-rate impact loads, high cycle with low magnitude (e.g., stress fractures) or bone diseases such as pelvic tumors or osteoporosis. Based on these facts, and due to the complexity of injured pelvises for surgeons to treat, the fracture mechanism in this bone and its treatments deserves better understanding. In this research, computer modeling was used to investigate the fracture mechanism in the pelvic bone and to design and optimize the fixation plates of a damaged pelvic bone.

The Finite Element Method (FEM) is a beneficial tool in engineering research to model failure characteristics of solid materials with complex shapes and material properties but not restricted to solid materials. Recently, the extended finite element method (XFEM) employs fracture mechanics to simulate fracture propagation in the bulk materials by allowing cracks to propagate through elements. In this research, the XFEM technique has been implemented to model fracture mechanism in the pelvic bones.

Considering both cortical and cancellous tissues simultaneously in fracture modeling of the bones is one of the requirements in developing a realistic model. Numerous researchers have employed XFEM analysis to model fracture mechanisms in cortical bones on the microscopic and macroscopic scales. However, there are limited studies that modeled fracture in cancellous bone by XFEM analysis. In this research, previously published materials and failure characteristics of cortical bone have been re-implemented on macro-scale level to be utilize in pelvic bone fracture modeling. Modeling the cancellous bone porosity in FE modeling of pelvic

bone was impractical because of the details on the micro-scale level of the bone. Alternatively, an equivalent model was developed to produce a behavior similar to that observed in the micro-scale models.

In order to do so, the experimental results of a published study (Ridha et al. 2013) were used to create a computational model capable of predicting the fracture of one trabecula. The predicted material characteristics of the trabeculae were then utilized in 2D and 3D XFEM models to estimate the behavior of cancellous bone tissue in microscopic scale. Finally, the equivalent model was created based on the obtained material behavior of cancellous bone specimen. The results of the equivalent model were found to be in excellent agreement with the micro-scale XFEM models.

Thus far, material behaviors and failure parameters of cortical and cancellous bones have been estimated. Also, an equivalent model from cancellous tissue in micro-scale level has been developed and evaluated with micro-scale modeling of cancellous specimen. The modeling resulting from cortical and cancellous tissues were integrated into the pelvic bone. Various loading conditions have been investigated to simulate different types of fracture in the pelvic bone.

Finally, the estimated material properties of cancellous and cortical tissues were assigned to a T-shaped damaged bone fixed by a customized bone plate. The fixation plate and screws characteristics were optimized by means of FE analysis (FEA) and the Design of Experiments (DoE) method. In order to do so, the DoE model was developed. Fixation plate thickness, plate material and the number of screws were selected as variables and reduction of stress shielding

and stiffer fixation were considered as model objectives. The ANOVA (analysis of variance) method was employed to determine the significant factors mentioned above, along with their effect values. The fixation plate material and thickness were determined as the first and second effective parameters respectively for design of implants, and their optimized values were found.

The contributions of my work were, developing XFEM models of cancellous bone specimens that are capable of accurately predicting the onset and propagation of cracks under mechanical loading, developing an equivalent constitutive model of cancellous bone to utilize in fracture modeling of bones in macro scale, developing an XFEM model that is capable of predicting different types of fracture in pelvic bone under various loading conditions and evaluating and optimizing the mechanical stability and stress shielding of the fixation system in T-shaped acetabular fracture by conjunction of Finite Element Analysis (FEA) and Design of Experiment (DoE).

Preface

This thesis is an original work by Mohammad Salem. Some parts of this thesis have been or will be submitted for publication as follows:

Chapter 3 of this thesis has been published as Salem, M., Westover, L., Adeeb, S., & Duke, K. (2020). Prediction of failure in cancellous bone using extended finite element method (XFEM). Proceedings of the Institution of Mechanical Engineers, Part H: Journal of Engineering in Medicine, 234(9), 988–999.

Chapter 4 of this thesis has been published as Salem, M., Westover, L., Adeeb, S., and Duke, K. (April 29, 2020). "An Equivalent Constitutive Model of Cancellous Bone with Fracture Prediction." ASME. J Biomech Eng.

Chapter 5 of this thesis is in progress and would be submitted to a scientific journal as M. Salem, L. Westover, S. Adeeb, K. Duke, “Prediction of fracture initiation and propagation in pelvic bones”.

Chapter 6 of this thesis is in progress and would be submitted to a scientific journal as M. Salem, L. Westover, S. Adeeb, K. Duke, “Optimization of fixation plates for T-shaped pelvic bone fractures”.

Dedicated to my Fateme and Ryan

Also dedicated to my family especially my parents

Acknowledgements

First, I would like to express my sincerest gratitude to my supervisors, Dr. Kajsa Duke, Dr. Samer Adeeb and Dr. Lindsey Westover for their supervision, constant support, and excellent and accurate guidance. I gratefully acknowledge the financial support I received from Dr. Kajsa Duke.

Next, I would like to thank my supervisory committee member, Dr. Don Raboud, and to my Ph.D. defense examination committee members, Dr. Hossein Rouhani, Dr. Heidi-Lynn Ploegh and Dr. Zengtao Chen , for their valuable contributions to my work and for their time.

I would like to acknowledge and thank to all of my friends, especially Majid Zare for his favors and joyful times we spent together.

I also would like to thank Dr. Cagri Ayranci and Dr. David Nobes for their supports at the beginning of my Ph.D. program.

Special thanks must be made to Dr. Samer Adeeb whom was my friend and family in this journey. I would like to thank him for his encouragement, expertise, friendship, and kindness. I learned a lot from him, and I am going to be always thankful for this.

Table of Contents

List of Tables

List of Figures

Chapter 1 : Introduction

1.1 Motivation and Problem Statement

The pelvic bone is one of the essential weight-bearing structures and one of the most stressed areas in the human anatomy [1, 2]. Pelvic bone fractures are among the most common clinical problems that occur, due to high-rate impact loads or bone diseases [3]. Due to the complexity of injured pelvises for surgeons to treat, the fracture mechanism of this bone and its treatments deserve a better understanding.

T-shaped pelvic fracture is one of the most complicated and common fractures in frontal motor-vehicle crashes and sideways falls especially among the elderly population [4, 5]. T-shaped fractures are commonly treated through internal fixation with lag screws and reconstruction plates [4-7]. Long-term stable fixation is the essential goal of surgical treatment [4, 6, 7]. However, in some cases the stress shielding occurs in the treated bone as a result of removal of the stress from the bone by an implant. The stress shielding causes the reduction of the bone density around implant and screws and finally loosens the implant in the long-term. The Finite Element Method (FEM) can be one of the greatest tools due to the complexity of injured pelvises for surgeons to find an appropriate fixation system with the maximum stability and minimum stress shielding.

The FEM, by incorporating continuum damage mechanics or fracture mechanics, is a beneficial tool in engineering research to model failure characteristics. Conventionally, traditional FEM utilizes element deletion techniques and continuum damage mechanics to model fracture propagation within bulk materials. More recently, the extended finite element method (XFEM) employs fracture mechanics to simulate fracture propagation in the bulk materials by allowing cracks to propagate through elements rather than simple element deletion.

FEA has been utilized to model the pelvis in numerous applications [6, 8-30]. A considerable number of these research articles are related to evaluation of internal fixation systems and the stability of fixed fracture bones by means of FEA [4, 6, 7, 21, 22, 25-27]. This study [4] evaluated several fixation systems in T-shaped fracture of pelvic bone and obtained the

optimized fixation system for the treatment of an injured bone. A large quantity of studies [31-36] investigated and optimized the fixation plate parameters (e.g., material selection, plate thickness, the number of screws and their optimal distance between the screws) using a combination of Design of Experiments (DoE) and FEA. To the best of our knowledge, there is no study to have optimized the fixation plate characteristics related to a damaged pelvic bone. Moreover, some studies [12, 20, 28-30] used FE models to examine pelvic damage mechanisms in backward falls, sideways falls and lateral impacts. These studies concentrated on the damage of pubic symphysis and sacroiliac joints. To the best of my knowledge, only one study [3] has modeled the crack initiation on the pelvic bone. However, instead of a real bone, a synthetic polyurethane pelvis was utilized to model the fracture [3]. This work is novel in that it is the first finite element model to simulate crack initiation in a based on real bone material properties.

As explained earlier, XFEM technique is becoming more common in biomechanics field. In numerous studies [37-54], XFEM analysis has been employed to carry out several bone fractures on microscopic and macroscopic scales. To the best of our knowledge, there is no study on utilizing XFEM technique to model fracture mechanism and different types of fracture in the pelvic bones. Due to a lack of knowledge about fracture mechanisms in the pelvic bones and according to the complexity of this bone, it needs better investigation.

The pelvic bone (similar to most other skeletal system bones) contains cortical and cancellous bones that are also called compact and trabecular bone, respectively [55]. The cortical bone is the external denser and stronger tissue of the bone and withstands forces, while the cancellous bone is the internal spongy tissue that makes the bone lighter and distributes the imposed loads to the stronger cortical tissue [55]. One of the requirements for implementing an accurate model of pelvic bone fracture is considering fracture mechanisms in the cortical and cancellous tissues.

A large quantity of articles [40-52, 56-58] have employed XFEM analysis to model the fracture mechanism in a cortical tissue. The fracture modeling of cortical bone was conducted by researchers for different purposes. In some studies [41, 43, 44, 46-49, 52, 56-58], the fracture mechanism has been developed to investigate the mechanical characteristics of cortical bones. On the other hand, other studies [40, 45] have utilized the XFEM analysis as an application to model the damage of cortical bones in the process of screw pull-out. In some of materials, the

failure initiation and propagation model is out of the built-in models in ABAQUS software. In these cases, a user subroutine called UDMGINI can be utilized for reaching specific crack initiation criteria out of the built-in models [59]. These studies [40, 51] used user-defined subroutine UDMGINI to define failure criteria of cortical bone.

Modeling the large volume of cancellous tissue porosity through FE modeling of bone requires large computational resources, which renders such models impractical. Alternatively, a macro-scale model can be developed without modeling the porosity of cancellous tissue. However, this macro-scale model can be an equivalent model that is able to produce a behavior similar to that observed in the micro-scale model. There are several studies [60-69] which have implemented various equivalent models to simulate micro-scale bone in a macro-scale. In some of these studies [60, 65, 66], the failure was not considered as part of the equivalent model, and in the other studies [61, 62] damage mechanics (element deletion) was utilized to simulate post yield behavior of the micro-scale bone. However, XFEM technique has some benefits compared to traditional damage mechanics [70-72] as it is able to model and predict fractures in different bones on multi-scale levels [3, 37, 54, 58, 73].

Limited studies [74, 75] have utilized XFEM technique to model failures in cancellous tissue. Tran et al. [74] utilized XFEM to apply a regular mesh to trabecular bone tissue. In their study, the elements that are within the voids can be modeled with small stiffness values in comparison to elements within the solid component of the tissue [74]. XFEM was then used to simulate the boundaries between the different phases without disrupting the mesh [74]. Also, Hammond et al. [75] utilized built-in XFEM models in ABAQUS to demonstrate crack formation in the cancellous bone specimen. To the best of our knowledge, however, there is no study on utilizing XFEM technique to extract material behavior and fracture parameters of cancellous tissue.

In this regard, two main objectives will be followed in current study. The first objective is investigating the fracture mechanism of pelvic bone with cortical and cancellous tissues under various loading conditions. The second objective is proposing and optimizing a custom implant to fix and treat a T-shaped fractured pelvic bone. In the following, the hypotheses and objectives are described in more detail.

1.2 Hypotheses and objectives

To achieve the first objective, the XFEM analysis was implemented on cancellous bone specimens on the micro-scale level (Chapter 3,4). Afterward, an equivalent model was developed based on the obtained material behaviors and failure parameters of cancellous bone specimen in microscopic scale (Chapter4). Additionally, the XFEM model of cortical bone in macroscopic scale was re-implemented by means of previously published models (Chapter 5). Finally, material behaviors and failure characteristics of cortical and cancellous tissues on macro-scale level were assigned to the pelvic bone (Chapter 5). The various loading conditions that cause different types of pelvic bone fracture in frontal motor-vehicle crashes were modeled and investigated (Chapter 5).

For the next outstanding objective of this research, an implant was proposed and designed for fixing the pieces of T-shaped fractured pelvic bone (Chapter 6). Pelvic bone displacement, crack opening and stress in the bone, and fixation plate and screws were examined to find the optimal parameters for reducing the stress shielding and increasing the stability of fixed pelvic bone. To achieve this aim, the DoE technique was utilized together with FE analysis to find the significant factors and improve the implant characteristics (Chapter 6).

Modeling of fracture mechanism in pelvic bone using finite element simulations was based on the following hypothesis and objectives:

Hypothesis of objective 1: Concept of partition of unity (which is explained in chapter 2.3) by incorporating conventional Finite Element Method (FEM) can effectively be implemented to model fracture initiation and propagation in micro- and macro- scale levels of bones (Chapter 3-6).

Objective 1: To investigate pelvic bone fracture mechanisms in various loading conditions (Chapter 3-5):

Specific aim 1. Defining material properties of cancellous bone tissue and performing XFEM modeling of crack formation and growth in a cancellous bone specimen (Chapter 3,4).

Specific aim 2. Extracting material properties of cancellous bone from the results of XFEM modeling to assign to a solid (no-porosity) part with the same dimensions of cancellous bone (Chapter 4).

Specific aim 3. Performing XFEM modeling of the pelvic bone with cortical and cancellous tissues and investigating the loading conditions of pelvic bone in order to model different types of fracture (Chapter 5).

Hypothesis of objective 2: Design of Experiments (DoE) combined to Finite Element Method can be utilized as an experiment alternative to designing and optimizing of fixation plates in an injured pelvis.

Objective 2: To propose a custom implant to fix and treat a fractured pelvic bone (Chapter 6):

Specific aim 4. Modeling a fractured pelvis with fixation plates and optimizing the fixation plate parameters using a combination of DoE and FEA (Chapter 6).

In the final chapter of the thesis, i.e. Chapter 7, the achievements, suggested future works, advantages and disadvantages of using the XFEM technique for fracture modeling in pelvic bone were presented. Chapter 7 also includes the achievements and suggested future works of using DoE technique for optimizing of fixation plates in injured pelvic bones. This thesis progresses from a microscopic level to a macroscopic level to the pelvis and finally the simulation of a clinical application as can be seen in Fig.1.1.

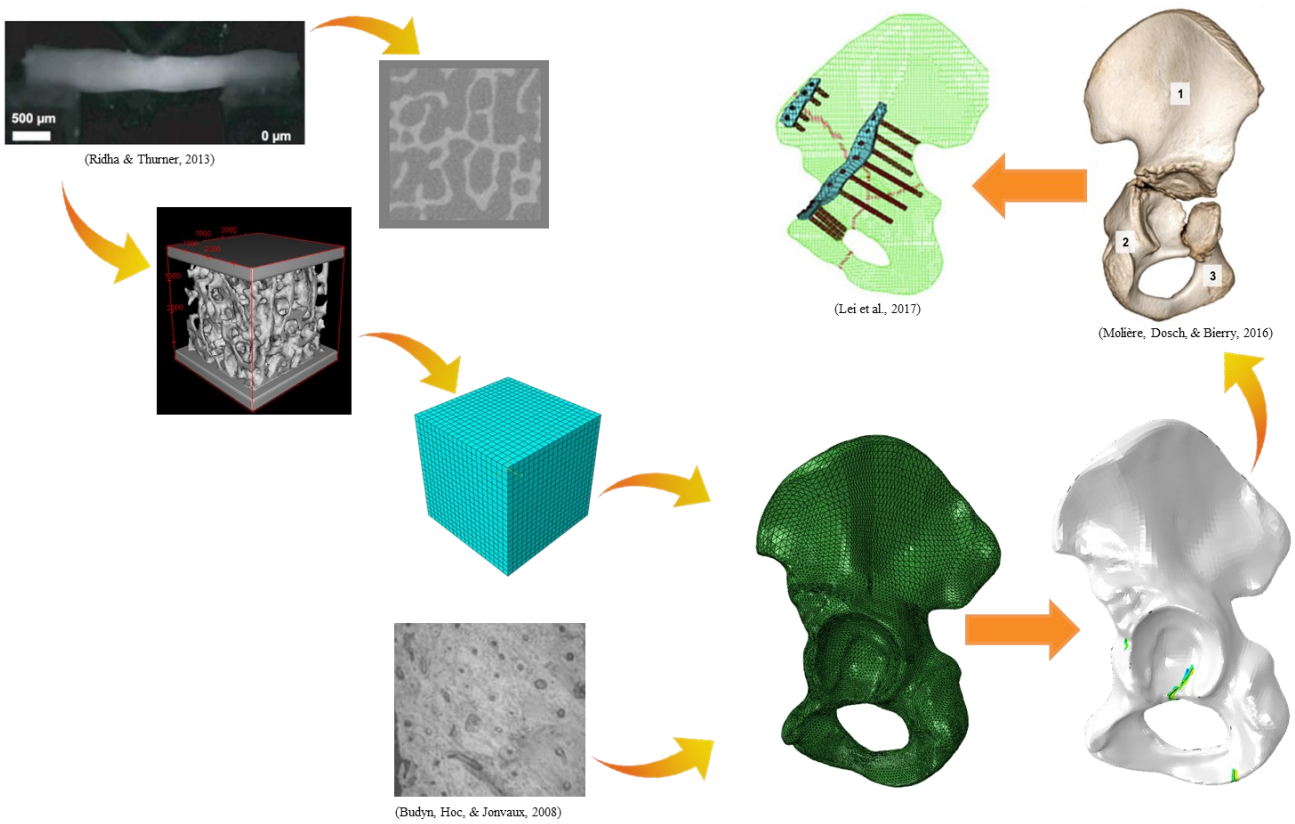

Figure 1.1. Graphical abstract describing the progresses from a microscopic level to a macroscopic level to the pelvis and finally the simulation of a clinical application

Chapter 2 : Literature Review

According to the objectives and the aims of this study, a literature review has been conducted in six sections. First section is dedicated to the pelvic bone and different types of fracture in this bone. In the second section, the studies about FE modeling of pelvic bone have been investigated. Third section is devoted to exploring the failure modeling techniques and the advantages of XFEM technique compared to traditional damage modeling technique. Fourth and fifth sections are allocated to investigate the studies related to cortical and cancellous bones, respectively. Finally, the research related to DoE method related to optimization of implants are explored in sixth section.

2.1 Pelvic bone anatomy and the types of fracture

Pelvic ring has a very important role in human skeleton system by linking the upper body to the lower extremities [8]. Pelvic bone is one of the most stressed areas in the human anatomy according to its location for transferring the upper body weight to the lower limbs and protecting the inner organs of that area [1, 2, 8]. Due to the important role of this bone, it was the center of attention of surgeons and scientists since the early 20^{th} century [8].

The complex anatomy of a pelvic bone is demonstrated in Fig.2.1. As it can be seen, the pelvic bone is formed by three main parts called Ilium, Ischium and Pubis [5]. These three parts fuse together and form a cup-shaped socket known as acetabulum [5]. Damage and fracture of pelvic bone or acetabulum is a common type of fracture [6]. More than half of the fractures in pelvic bones are caused by motor-vehicle crashes [12]. There are different types of fracture in pelvic bones that can be classified in three main groups of A, B and C [5]. Surgeons utilize the simplified anatomy of pelvic bone that is shown in Fig.2.2 for better interpretation of different types of fractures [5]. In Fig.2.2 it can be seen that pelvic bones are made from two columns and two walls that meet at the roof of acetabulum [5]. The fracture type A is related to partial articular fractures of acetabulum [5]. Transverse or T-type fractures are considered as type B of pelvic bone fractures in which a portion of the articular surface of the acetabulum is still connected to the intact ilium [5]. In type C, both columns are fractured, and no portion of the acetabulum is connected to the intact ilium [5].

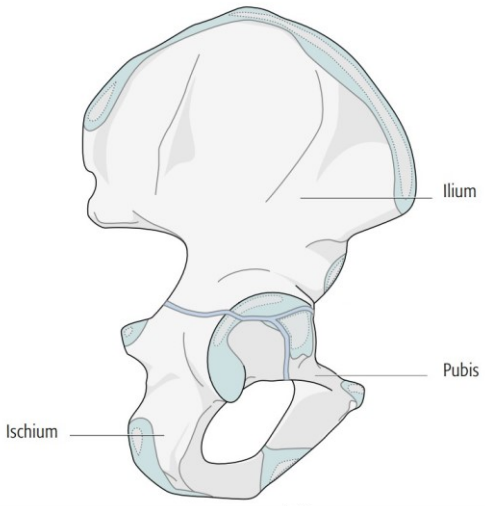

Figure 2.1. Ischium, pubis, and ilium parts of pelvic bone [5]

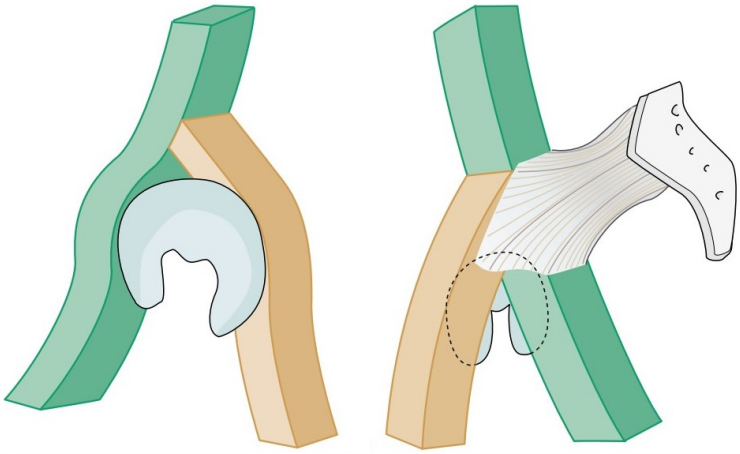

Figure 2.2. Pelvic bone is composed of two columns and walls that meet at the roof of acetabulum[5]

T-shaped fracture classifies as one of the complicated fractures of pelvic bones [5]. 7% of pelvic fractures with two or more fractures within the acetabulum are T-shaped fractures that are designated as type B fractures, as demonstrated in Fig.2.3 [5]. In T-shaped fractures, acetabulum splits vertically (Fig.2.4) [5]. The vertical fracture may enter any part of acetabulum cavity and subdivide the fracture into a T-type fracture as it is shown in Fig.2.4.

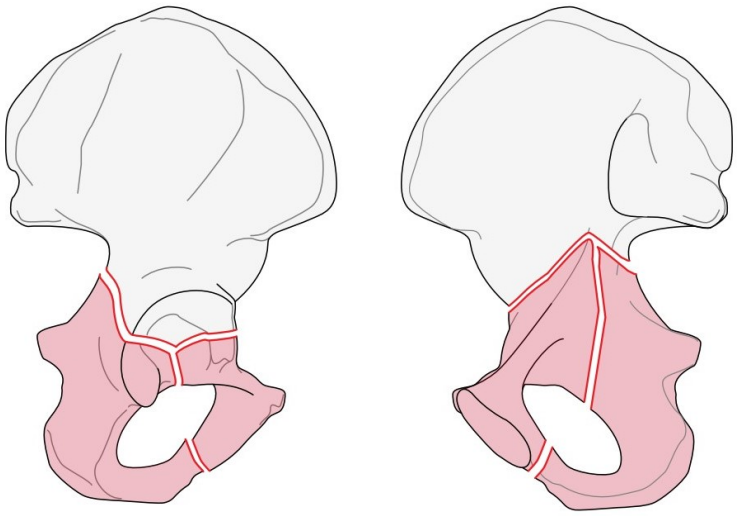

Figure 2.3. T-shaped fracture in pelvic bone [5]

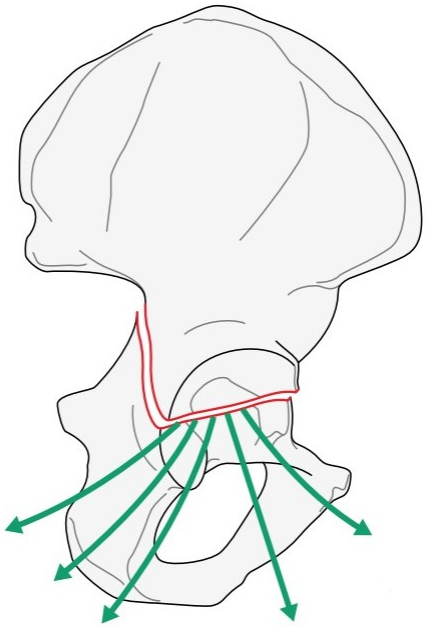

Figure 2.4. Possible directions of the fracture of the T in T-type fractures.[5]

The fixation of T-shaped fracture is explained in [5] which is a reference for the surgeons; also, different types of fracture in pelvic bone and acetabulum are described in this book. The fixation system of T-type fracture with the fixation plate and lag screws can be observed in Fig.2.5 [5]. Also, there are numerous studies [76-82] that have been dedicated to evaluating the functional outcomes of operative treatment of such injuries. However, to the best of our knowledge, there is only one study [4] that has investigated the fixation system of T-type fracture in pelvic bone

by FEA. Fan et al. [4] evaluated three different fixation systems of T-shaped fracture by FEA and obtained the optimized fixation system for treatment of the injured bone. The three fixation systems are demonstrated in Fig.2.6. The obtained results proved that the fixation system shown in Fig.2.6(c) has the best functional criteria [4].

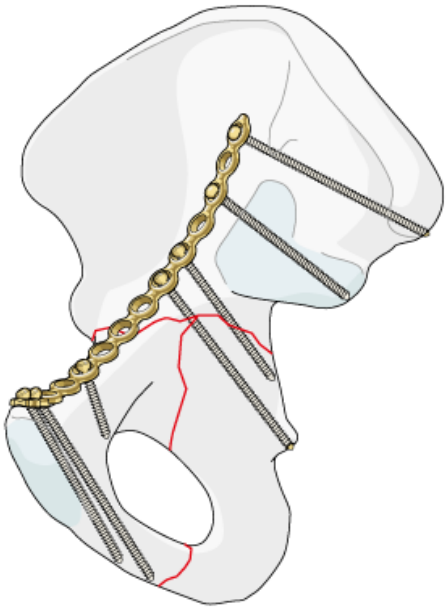

Figure 2.5. Fixation system of T-type fracture[5]

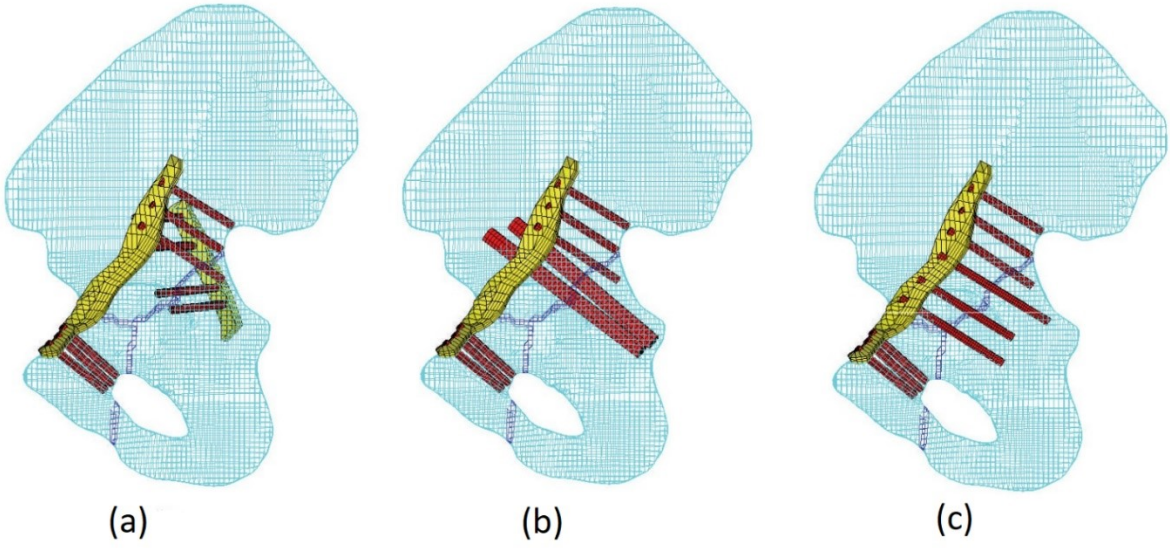

Figure 2.6. Three different fixation systems of T-shaped fracture[4]

2.2 FE modeling of pelvic bone

According to the complex morphology of pelvic bone and its inaccessible location, surgeons and researchers have intended to use FE modeling rather than experiments. In this section, the studies related to FE analysis of pelvis ring and pelvic bone have been investigated. The main purpose of conducting this subsection was a comprehensive coverage of literature related to fracture modeling of the pelvic bone and its fixation system. In the following, the application of related studies has been indicated and a detailed review corresponding to this subject will be published in the future.

These papers [8, 83-86] investigated the effects of boundary conditions on FE results. Phillips et al. [83] claimed that previous finite element studies had extensive simplifications of boundary conditions. Thus, the authors modeled pelvis bones with fixed boundary conditions that were utilized in previous studies and pelvic bones that are supported by muscular and ligamentous boundary conditions to compare the differences between them [83]. Shi et al. [8] studied the synovial joint role of the sacroiliac joint (SIJ) in the human pelvic system. The authors modeled SIJ penetration model and SIJ contacting model. In the first model, interfaces were penetrated together, and the interfaces related to the second model were just in contact with each other. Also, in the second model, the ligaments were modeled as representatives of boundary conditions [8]. Watson et al. [84] developed a series of pelvis FE models to investigate the relationships between the applied boundary conditions and the extracted stress distributions; the authors specifically studied the SIJ and pubic symphysis [84]. Hu et al. [85] used the FE model to analyze the influence of boundary conditions and connection conditions on stress distribution in pelvis ring. Three conditions were modeled in this paper [85]: first model with contact between femur head and acetabulum, another one the surfaces fused together in hip joint connecting area and the last one without proximal femurs [85]. After analyzing of stress distribution in three different models using FEA, Hao et al. [86] concluded that the connect condition of hip joint should not be neglected in FE modeling. In all of these studies [8, 83-86] the FEA was utilized to improve and develop more realistic boundary conditions for the pelvic ring.

The authors of these studies [87-92] have developed a more realistic FE model by considering the ligaments, muscle forces, cortical and cancellous bones, the thickness of cortical and trabecular bones in their FE models. Dalstra et al. [87] presented detailed finite element analyses of the pelvic bone and evaluated stress distributions under physiological conditions. Dalstra et al. [88] developed and validated a three dimensional FE model of pelvic bone. The authors considered cortical and cancellous bones as part of model to develop a more realistic FE model of the pelvic bone [88]. Anderson et al. [89] developed and validated a realistic FE model according to cortical and trabecular bone thicknesses to assess the strain prediction regarding the thicknesses and material properties of bone and cartilage. Ivanov et al. [90] developed an FE model of pelvis ring including the ligaments. The authors assessed the effects of different positions of SIJ to sacrum angulation, which is a physiological motion [90]. In Eichenseer et al. [91] a human pelvis- SIJ and sacroiliac ligaments were modeled. This study [91] aimed to evaluate the ligaments strains and stiffness on motion, displacement, rotation, and stresses of SIJ. In this study [92], an FE model of the pelvis was developed with estimation of joints movement and muscle forces throughout the gait cycle to analyze the stress distribution of pelvis ring while walking normally.

Kuraria et al. and Zant et al. [93, 94] investigated the stress evaluation and fatigue behavior in pelvis and prosthesis. Kuraria et al. [93] developed an FE model to evaluate the stress distribution and fatigue behavior on peak contact force under different loading conditions. Zant et al. [94] evaluated fatigue mechanism and the behavior of cemented prosthesis cup during normal walking and stair climbing.

Watson et al. and Mei et al. [95-97] modeled the reconstructed pelvis and compared the results to the original one. In [95] the FEA was used to compare the strain distribution between a reconstructed hemipelvis bone and the original one. Watson et al. [96] presented an innovative approach to digitize a damaged hemipelvis. They compared the reconstructed pelvis using their proposed technique to the original CT data and validated their proposed method [96]. Mei et al. [97] developed an FE model of the reconstructed pelvic ring to analyze the mechanical stresses on pelvis ring after hemipelvectomy. Also, Kumar et al. [98] developed asymmetric hemipelvis by utilizing some features of Geomagic software, and compared the results to those of mirrored

hemipelvis in order to determine the differences between two sides of pelvis ring. The purpose of this study [98] was to decrease the calculation volume of FE analyzing in case of fracture on one side of pelvis ring.

Frydrýšek et al. and Ali et al. [99, 100] proposed, designed and investigated the capabilities of external fixators. Frydrýšek et al. [100] designed an external fixator and evaluated it by FEA that can be used to stabilize fractures of limbs, pelvis and its acetabulum. Ali et al. [99] used FE model to assess the stiffness of an external fixation of pelvic ring fracture and the parameters that influence mechanical performance of external fixators.

Some researchers evaluated internal fixation systems as well as the stability of complex fractures in hemipelvis bone or pelvic ring by FEA [4, 6, 7, 9, 15, 17, 18, 21, 22, 25-27, 75, 101-117]. One of the most common pelvic ring injuries is type C fracture, and that the fixation of this type of damage was analyzed in these studies [26, 102, 103]. To the best of our knowledge, this study [4] is the only one that utilized FEM to evaluate several fixation systems for T-shaped fracture of pelvic bone. The authors obtained the optimized fixation system (including the optimized number of implants and screws and their placement in the fixation system) for the treatment of an injured bone with T-shaped fracture [4].

These studies [14, 19, 118-125] simulated human pelvis and lower limb to investigate the injury mechanisms in different types of crashes. Kikuchi et al. [118], modeled a human pelvis and lower limb to predict the injuries during the frontal motor-vehicle impact. For simulation of knee-thigh-hip (KTH) complex injuries in frontal motor vehicle crashes, the FE models were developed and bone deformation, articulating joints and soft tissue behavior in the KTH complex were the characteristics that were analyzed by Van Rooij et al. [119]. Ikeda et al. [120] used FE models to predict the different fracture patterns of pelvis ring in pedestrian accidents with SUV/ Mini-Vans. The developed models were capable to accurately predicting the different pattern of pelvic fractures [120]. This is the only study [120] that has predicted the fracture location in the pelvis ring in frontal car crashes. Silvestri et al. [121] developed an FE model of KTH with ligaments and muscles to explore the mechanics of injuries of the KTH during frontal crashes. Shen et al. [122] used the FE model of the pelvis and lower extremities to investigate the injury mechanisms of a ten-year-old child for improving pedestrian protection

for this age group. Snedeker et al. [14] simulated the FE models of a male pedestrian with various impacts and different hood shapes to investigate the shape of hood leading edge in pedestrian-car accidents. In this study [19], an FE model of the pedestrian was created to model the injury mechanisms in side collision accidents. Ma et al. [19] considered the cortical and cancellous bone in their FE modeling. Majumder et al. [123] simulated side impact situation for the pedestrian in automotive accidents. For a realistic simulation, they [123] modeled human pelvis-femur-soft tissue complex and spring-dashpot-mass that represent the whole body. Yue et al. [124] developed an FE model of lower extremity to improve the understanding of KTH injuries mechanisms. Yue et al. [124] considered the frontal and lateral loadings in their FE modeling. Gunji et al. [125] investigated the influence of different parts of human body mass on pelvis injury mechanism on car-occupant crashes through using FEA. They also [125] used four different vehicle models to investigate the influence of loading locations from the hood edge on pelvis injury mechanism.

In these papers [3, 12, 20, 28-30, 126-133], the fractures and injury mechanisms in pelvis were modeled and investigated. The papers [12, 20, 28-30, 126-131] studied pelvic injury mechanisms in backward and sideways falls, and lateral pelvic impacts using FE models. Kim et al. [130] investigated the effects of childhood obesity on pelvic bone fracture risk exposed to falls. Song et al. [131] developed the FE models of vertebrae and pelvis to analyze the dynamic mechanisms of these bones in human falls. These studies [12, 20, 28-30, 126-131] concentrated on the damage of pubic symphysis and sacroiliac joints, and the fracture modeling of the bone was not considered as part of the simulation. Besnault et al. [133] introduced a material model to simulate damage and injury in the human pelvis ring. To the best of my knowledge, only one study [3] has modeled the crack initiation on the pelvic bone. However, instead of a real bone, a synthetic polyurethane pelvis was utilized to model the fracture [3].

2.3 Extended Finite Element Method

The Finite Element Method (FEM), by incorporating continuum damage mechanics or fracture mechanics, is a beneficial tool in engineering research for modeling failure characteristics of complex structures. Conventionally, traditional FEM utilizes element deletion techniques and continuum damage modeling to model fracture propagation within bulk materials. More

recently, the extended finite element method (XFEM) employs fracture mechanics to simulate fracture propagation in the bulk materials by allowing cracks to propagate through elements, rather than simple element deletion.

Researchers have shown that using the element deletion technique of traditional FEM can lead to some physical inaccuracy in the results caused by the removal of some elements [70-72]. Likewise, the accuracy of solutions in the element deletion technique is more dependent on the element size than the element splitting technique of XFEM analysis [70-72]. In XFEM analysis, a crack can be modeled independently from the mesh and can be grown arbitrarily and depend on the solution [59]; furthermore, this technique does not require adaptive remeshing [59]. In biomechanics, XFEM analysis is becoming a common tool for predicting and modeling fracture in different bones on multi-scale levels [3, 37, 54, 58, 73]. In the following, the XFEM technique will be explained in detail.

XFEM is an extension of the finite element method based on the partition of the unity method [59]. In the XFEM framework, discontinuities in an element are enabled by enriching degrees of freedom using a displacement vector function that is shown in Equation 2.1 [59].

$$\mathrm{u} = \sum_{I=1}^{N} N_I(x)\left[u_I + H(x)a_I + \sum_{\alpha=1}^{4} F_\alpha(x)b_I^\alpha\right] \tag{2.1}$$

where $N_I(x)$ is the usual nodal shape function; u_I is the nodal displacement vector; $H(x)a_I$ is the product of the nodal enriched degree of freedom vector, a_I, and the associated discontinuous jump function $H(x)$ across the crack surfaces. $F_\alpha(x)b_I^\alpha$ is the product of the nodal enriched degree of the freedom vector, b_I^α, and the associated elastic asymptotic crack-tip functions, $F_\alpha(x)$. For modeling the propagating (not stationary) crack, the third term on the right-hand side (near-tip asymptotic singularity) of Equation 2.1 is being neglected, and the equation will be simplified to Equation 2.2 [59].

$$u = \sum_{I=1}^{N} N_I(x)[u_I + H(x)a_I] \tag{2.2}$$

All the cracks modeled in this research are propagating cracks, for which Equation 2.2 will be implemented to solve.

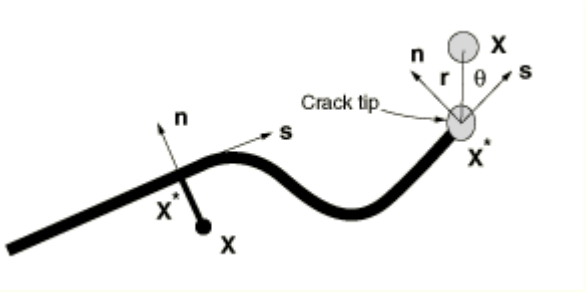

Figure 2.7. Illustration of normal and tangential coordinates for a smooth crack [134]

The discontinuous jump function across the crack surfaces, $H(x)$, is shown in Fig.2.7 and given by Equation 2.3 [59].

$$H(x) = \begin{cases} 1 & \text{if } (x - x^*).n \geq 0, \\ -1 & \text{otherwise,} \end{cases} \tag{2.3}$$

where x is an arbitrary example of Gauss point, x^* is the closest point on the crack to x, and n is the normal unit to the crack at x^*.

Crack propagation is implemented in the element based on the phantom nodes approach (as shown in Fig.2.8) [59]. While the crack is being initiated in an element, the phantom nodes will be located at the same location as the original nodes [59]. The phantom nodes are conjugated with the damage evolution law [59]. When the damage evolution law is satisfied, the crack opening will begin and the phantom nodes will be located independently from the original ones [59].

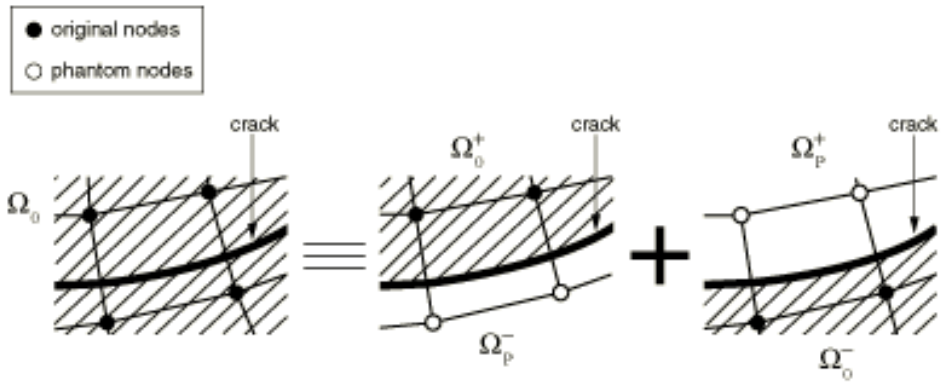

Figure 2.8. The principle of the phantom node method [134]

So far, the XFEM framework is provided only in ABAQUS/Standard [59]. Furthermore, XFEM framework merely supports first-order 2D and 3D stress/displacement solid continuum elements and second-order stress/displacement tetrahedral elements [59].

2.4 Cancellous tissue

One of the requirements for developing an accurate model of bone fracture in the macro-scale is considering the fracture mechanism in the cortical and cancellous tissues on the micro-scale. There are several studies [135-141] which utilized damage mechanics and element deletion technique to model failure in trabecular tissue. However, as explained earlier, XFEM technique is becoming more common in biomechanics field according to its benefits. To the best of our knowledge there is only one study [75] that modeled microcracking in cancellous bone by XFEM model. In that study, Hammond et al. [75] utilized XFEM to demonstrate crack formation in the cancellous bone. Also, XFEM has been utilized in an interesting study by Tran et al. [74] to apply a regular mesh to trabecular bone tissue. Elements that are within the voids can be modeled with small stiffness values in comparison to elements within the solid component of the tissue. XFEM was then used to simulate the boundaries between the different phases without disrupting the mesh[74].

There are two approaches for modeling material properties of bone tissue that have so far been reported in the literature. In some studies, both cortical and cancellous tissues are assumed to be quasi-brittle materials with the same properties at the micro level [142-144]. However, in most research, only the cortical bone is considered to be quasi-brittle, and the cancellous tissue

is assumed to be a ductile material [136, 143-147]. In this thesis, the suitability of both models in an XFEM model setting to predict the reported experimental behavior of cancellous bone is compared.

One of the objectives of our research is to develop a 2D computational model using the built-in XFEM technique in ABAQUS that is capable of predicting the fracture behavior of trabecular tissue. In order to do so, the experimental results of a three-point bending test obtained by Ridha et al. [148] are used to create a computational model capable of predicting the fracture of one trabecula. Ridha et al. [148] conducted three point bending tests on ten single trabeculae which were excised from bovine proximal cancellous bone. The authors employed a custom-made three point bending device in which the two end points were constrained in all directions while a vertical displacement was applied to the specimen at the middle [145, 149]. The resulting load-displacement graph for one trabecula is shown in Fig.2.9 [148]. Using trial and error, the experimental load-displacement graph of Fig.2.9 is used to calibrate the material properties of the trabecula for two material models with brittle and ductile behaviors. The predicted material characteristics of the trabecula are then utilized to predict the strength of the cancellous bone tissue of the forearm along three anatomical axes.

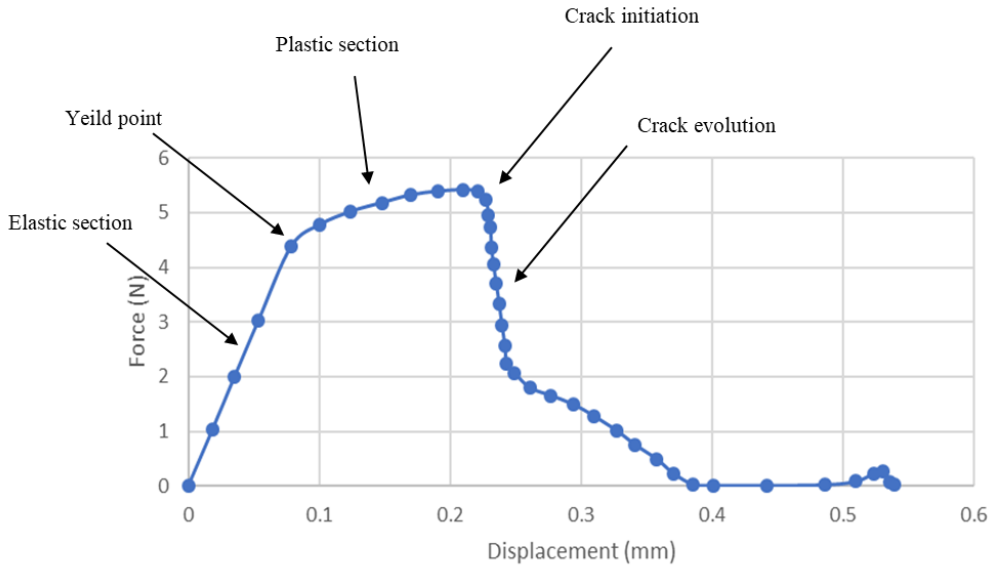

Figure 2.9. Load-displacement graph for a trabecula from three-point bending test [148]

Modeling the large volume of cancellous tissue porosity in FE modeling of bone requires large computational resources which renders such models impractical. Alternatively, a macro-scale

model can be developed in which traditional continuum elements are used to model the trabecular tissue as a continuum without modeling the individual trabeculae provided they produce a behavior similar to that observed in the micro-scale models. There are several studies [60-69] which implemented various constitutive models to simulate micro-scale bone in a macro-scale. In some of these studies [60, 65, 66], the failure was not considered as part of the constitutive model and in the other studies [61, 62] damage mechanics was utilized to simulate post yield behavior of the micro-scale bone. In the majority of the developed constitutive models, only one of the anatomical directions [60-62, 67] is considered. In addition, the behavior of bone under compression [60-62] is considered. Therefore, another objective of our work is to identify and implement a comprehensive macro-scale model that is able to consider the behavior in the different anatomical directions and in both compression and tension.

2.5 Cortical bone

As explained earlier, XFEM has been considered a valuable analytical method in biomechanics because of its potential to predict fractures in bones. Numerous researchers [40-52, 56-58, 148, 150, 151] have employed XFEM analysis to model fracture mechanisms in cortical bones on the microscopic and macroscopic scales. The fracture modeling of cortical bone was conducted by researchers for different purposes. In some studies [41, 43, 44, 46-49, 51, 52, 56-58, 150, 151], the fracture mechanism has been developed to investigate the mechanical characteristics of cortical bones. On the other hand, other studies [40, 45] have utilized the XFEM analysis as an application to model the damage of cortical bones in the process of screw pull-out. In some of materials with the specific behaviors like bone tissues, the failure initiation and propagation model are out of the built-in models in ABAQUS software. In these cases, a user subroutine called UDMGINI can be utilized for reaching specific crack initiation criteria out of the built-in models [59]. These studies [40, 51] used user-defined subroutine UDMGINI to define failure criteria of cortical bone. Since, in this study [40] the failure criteria has been developed in macro-scale level, it has been selected to be re-implemented in this thesis.

The user-defined subroutine UDMGINI of this study [40] has been re-implemented to be utilized as cortical tissue of pelvic bone in fracture modeling. There are four failure criterion equations which are indicated in equations 2.4-2.7 [40]. Once the value of any equation reaches

to 1, fracture is initiated for that criterion. Failure in X, Y and Z directions are determined by equations 2.4-2.6 respectively [40]. In the equation 2.7, when the maximum principle stress reaches to the effective strength, the fracture initiates and propagates to the normal direction of the maximum principal direction [40]. The failure criteria in X and Y directions (equations 2.1 & 2.2 respectively) have been defined in tension and compression, hence six failure parameters are indicated in Table 2.1 [40].

$$Failure\ criterion\ 1: \sqrt{(\frac{\sigma_{11}}{\sigma_{lx}})^2 + (\frac{\sigma_{12}}{\sigma_{lx\tau}})^2 + (\frac{\sigma_{13}}{\sigma_{lx\tau}})^2} = 1 \tag{2.4}$$

$$Failure\ criterion\ 2: \sqrt{(\frac{\sigma_{22}}{\sigma_{ly}})^2 + (\frac{\sigma_{12}}{\sigma_{ly\tau}})^2 + (\frac{\sigma_{23}}{\sigma_{ly\tau}})^2} = 1 \tag{2.5}$$

$$Failure\ criterion\ 3: \sqrt{(\frac{\sigma_{33}}{\sigma_{lz}})^2 + (\frac{\sigma_{13}}{\sigma_{lz\tau}})^2 + (\frac{\sigma_{23}}{\sigma_{lz\tau}})^2} = 1 \tag{2.6}$$

$$\text{Failure } criterion\ 4: \frac{\sigma_p}{\sqrt{\sigma_{lx}{}^2\cos^2\theta + \sigma_{ly}{}^2\sin^2\theta}} = 1 \tag{2,7}$$

Where σ_{lx} and $\sigma_{lx\tau}$ are the axial and shear strengths in X direction respectively, σ_{ly} and $\sigma_{ly\tau}$ are the axial and shear strengths in Y direction respectively and σ_{lz} and $\sigma_{lz\tau}$ are the axial and shear strengths in Z direction respectively. σ_p is the maximum principal stress and $\sigma_{11}, \sigma_{22}\ and\ \sigma_{33}$ are orthogonal normal stresses and $\sigma_{12}, \sigma_{23}\ and\ \sigma_{13}$ are orthogonal shear stresses [40].

Table 2.1. Elasticity, strengths and damage evolution parameters of cortical bone [40]

Mechanical properties		initiation criteria failure strengths (MPa)	
E_{11}MPa	4500	σ_{lx}(tensile)	150
E_{22}MPa	2200	$\sigma_{ly} = \sigma_{lz}$(tensile)	65
E_{33}MPa	2200	σ_{lx}(Compression)	280
G_{12}MPa	1000	$\sigma_{ly} = \sigma_{lz}$(Compression)	213
G_{23}MPa	846	$\sigma_{lx\tau}$	84
G_{13}MPa	1000	$\sigma_{ly\tau} = \sigma_{lz\tau}$	132
ν_{23}	0.3	Evolution criteria (J/m^2)	
		Failure criteria 1	800
		All other failure criteria	300

2.6 Design of Experiments (DoE) in biomechanics

Geometrical configuration and material selection of reconstruction plates and lag screws play a significant role in generating the biomechanical performances such as reliable internal fixation and reduction of stress shielding and implant loosening [31-36, 152]. Screw configurations such as the number of screws, their placement in the locking plates, the length and diameter of screws were investigated in [34]. The shape, thickness and width of the locking plates are the parameters of fixation plate which were optimized in [32, 33]. The optimal material selection and implant design such as using porous structure in the implants have been investigated in [31, 152] for reduction of stress shielding and acceleration of fracture healing. This study [153], utilized the combination of FE model with Taguchi method and probabilistic approach to identify the main input variables and then only modeled the effective variables to determine their effects. They demonstrated the combination of these methods can minimize the computational resources without sacrificing model accuracy. These studies [31-36] investigated and optimized the fixation plate-screws parameters using a combination of DoE and FE analysis. In this study [35] a combination of DoE, FEA and Taguchi method has been utilized to design and optimize a composite fixation plate for a damaged tibia. As previously mentioned,

in this study [4] several fixation systems of T-shaped fracture of pelvic bone have been evaluated and the optimized fixation system (including the optimized number of implants and screws and their placement in the fixation system) for the treatment of an injured bone has been defined. To the best of our knowledge, there is no study to have optimized the characteristics of fixation implant related to a damaged pelvic bone.

Chapter 3 : Prediction of Failure in Cancellous Bone using XFEM

3.1 Abstract

Objective: Develop XFEM models of cancellous bone specimens that are capable of accurately predicting the onset and propagation of cracks under mechanical loading.

Methods: Previously published three-point bending test results of a single trabecula were replicated using two different XFEM approaches (elastic-plastic-fracture; EPF and elastic-fracture; EF) that considered different configurations of the elasto-plastic properties of bone from which the best approach to fit the experimental data was identified. The behavior of a single trabecula was then used in 2D XFEM models to quantify the strength of trabecular tissue of the forearm along three perpendicular anatomical axes.

Results: The EPF model better represented the experimental data in the model of a single trabecula. Considering the 2D trabecular specimens, the EF model predicted higher strength than the EPF model and there was no difference in stiffness between the two models. In general, the specimens exhibited higher failure strain and more ductile behavior in compression than in tension. Additionally, strength and stiffness were found to be higher in tension than compression on average.

Conclusion: With proper parameters, XFEM is capable of simulating the ductile behavior of cancellous bone. The models are able to quantify the tensile strength of trabecular tissue in the various anatomical directions reporting an increased strength in the longitudinal direction of forearm cancellous bone tissue. XFEM of cancellous bone proves to be a valuable tool to predict the mechanical characteristics of cancellous bones as a function of the microstructure.

3.2 Introduction

Most bones in the human skeleton are made of cortical and cancellous tissues [55]. The cortical bone, also termed compact bone, is the denser and stronger tissue, while the cancellous bone,

also termed trabecular bone, is a spongy tissue that is able to distribute the imposed forces to the stronger cortical tissue while maintaining a lighter bone structure [55].

Bone fractures usually occur as a result of high-rate impact loads, or bone diseases such as osteoporosis. Damage in a bone appears in the form of microcracks, and the accumulation of microcracks leads to bone fracture [154]. While there are some empirical relationships that relate the stiffness and strength to the micro-structure, there is still a need to develop models that are capable of predicting the mechanical properties as a function of the trabecular structure.

The Finite Element Method (FEM), by incorporating continuum damage mechanics or fracture mechanics, is a very beneficial tool in engineering research to model failure characteristics of solid materials. Conventionally, traditional FEM utilizes element deletion techniques and continuum damage modeling to model fracture propagation within bulk materials. More recently, the extended finite element method (XFEM) employs fracture mechanics to simulate fracture propagation in the bulk materials by allowing cracks to propagate through elements rather than simple element deletion.

Researchers have shown that using the element deletion technique of traditional FEM can lead to some physical inaccuracy in the results caused by the removal of some elements [70-72]. Likewise, the accuracy of solutions in the element deletion technique is more dependent on the element size than the element splitting technique of XFEM analysis [70-72]. In XFEM analysis, a crack can be modeled independently from the mesh and can be grown arbitrarily and dependent on the solution [59]; furthermore, this technique does not require adaptive remeshing [59]. In biomechanics, XFEM analysis is becoming a common tool for predicting and modeling fracture in different bones on multi-scale levels [3, 37, 54, 58, 73].

One of the requirements for implementing an accurate model of bone fracture is considering fracture mechanisms in the cortical and cancellous tissues. There are several studies [135-138, 155, 156] which utilized damage mechanics and element deletion technique to model failure in bone tissues. However, as explained earlier, XFEM technique is becoming more common in biomechanics field according to its benefits. Numerous researchers [40-50, 52, 56-58, 148] have employed XFEM analysis to model fracture mechanisms in cortical bones on the microscopic

and macroscopic scales. However, to the best of our knowledge there is only one study [75] that modeled microcracking in cancellous bone by XFEM analysis. Hammond et al. [75] utilized built-in XFEM models in ABAQUS to demonstrate crack formation in the cancellous bone specimen. Also, XFEM has been utilized in an interesting study by Tran et al. [74] to apply a regular mesh to trabecular bone tissue. Elements that are within the voids can be modeled with small stiffness values in comparison to elements within the solid component of the tissue. XFEM was then used to simulate the boundaries between the different phases without disrupting the mesh[74].

There are two approaches for modeling material properties of bone tissue that have so far been reported in the literature. In some studies, both cortical and cancellous tissues are assumed to be quasi-brittle materials with the same properties at the micro level [142-144]. However, in most research, only the cortical bone is considered to be quasi-brittle, and the cancellous tissue is assumed to be a ductile material [136, 143-147]. In this paper, the suitability of both models in an XFEM model setting to predict the reported experimental behavior of cancellous bone is compared.

The objective of our study is to develop a 2D computational model using the built-in XFEM technique in ABAQUS that is capable of predicting the fracture behavior of trabecular tissue. In order to do so, the experimental results of a three-point bending test obtained by Ridha et al. [148] are used to create a computational model capable of predicting the fracture of one trabecula. Using trial and error, the experimental load-displacement graph in [148] is used to calibrate the material properties of the trabecula for two material models with brittle and ductile behaviors. The predicted material characteristics of the trabecula are then utilized to predict the strength of the cancellous bone tissue of the forearm along three anatomical axes.

3.3 Methods

3.3.1 Comparison with Experimental Results

Ridha et al. [148] conducted three point bending tests on ten single trabeculae which were excised from bovine proximal cancellous bone. The details of their work has been published

and will be summarized here for completion. The average segment length and the average diameter were reported to be 2.52 mm and 0.56 mm, respectively. The authors employed a custom-made three point bending device in which the two end points were constrained in all directions while a vertical displacement of 600µm was applied to the specimen at the middle [145, 149]. The resulting load-displacement graph for one trabecula is shown in Fig.3.1 [148].

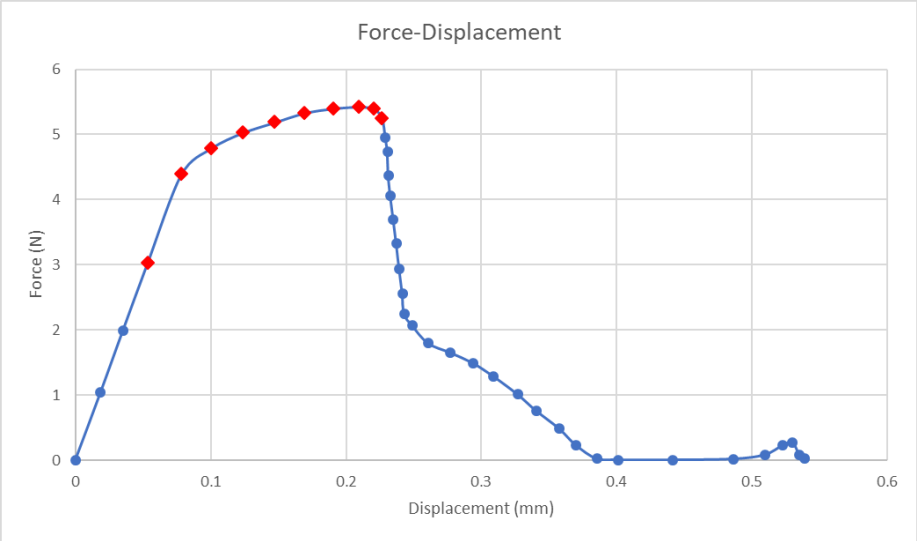

Figure 3.1. Experimental Load-displacement graph for a single trabecula in a three point bending test [148]. Red Diamonds represent points on the graph used for optimization of material properties.

3.3.2 XFEM analysis of a single trabecula

Based on the description in [148] the tested trabecular segment had a length of 2.5mm and a variable thickness shown in Fig.3.2. A screenshot of trabecula's geometry from [148] was imported and redrawn in Solidworks. The reported overall length of 2.5mm [148] was used to scale the picture to the appropriate dimensions . All the simulations were solved as 2D plane-stress problems with an out-of-plane thickness of 480µm which was chosen based on the average thickness of the trabecula in Fig.3.2. A 600µm displacement was applied vertically (Y direction in Fig.3.2) to the two nodes surrounding the middle point. The two nodes surrounding the two support points are fully constrained in all directions (Fig.3.2). To avoid infinite stresses in the model, two nodes were selected to define displacement in the middle and two nodes were constrained for each individual support.

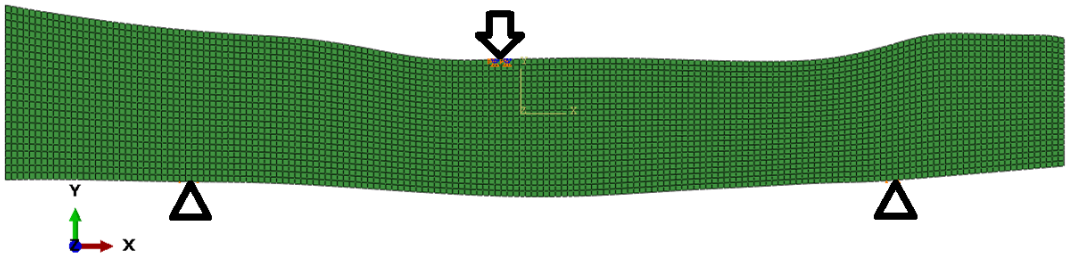

Figure 3.2. Geometry of one single trabecula and boundary conditions reimplemented in ABAQUS [148]

The XFEM framework built-into the general purpose finite element analysis software ABAQUS/Standard was utilized [59]. All simulations were conducted based on static equilibrium. The XFEM framework merely supports first-order 2D and 3D stress/displacement solid continuum elements and second-order stress/displacement tetrahedron elements [59]. Thus, CPS4 (4-node bilinear plane stress quadrilateral) elements were selected in all simulations. An initial mesh sensitivity study revealed that the obtained load-displacement curve (load at constrained supports and displacement at the nodes surrounding the middle point) for an average mesh size of 0.02mm differed from that obtained with the mesh size of 0.015mm by less than 2%. We opted to use the finer mesh of 0.015mm for the analysis of the results. The whole trabecula section is defined as the enrichment zone, which allows XFEM to initiate and propagate a crack anywhere within this region. Rather than defining the location of the initial crack, the XFEM framework allows the prediction of the crack initiation location as the load is applied based on the defined damage parameters. This option was utilized in this model.

In order to find the best set of material properties that are capable of replicating the experiments, two different sets of material properties for the trabecular bone tissue were chosen. The first set was termed elastic-plastic-fracture (EPF) in which the bone was assumed to behave elastically up to a limit followed by a plastic behavior, followed by fracture. The second set was termed elastic-fracture (EF) where the bone was assumed to behave elastically up to fracture [142-144]. For both material sets, the initial elastic behavior was described by an isotropic material model with Young's modulus and Poisson's ratio. Poisson's ratio was taken as 0.3 according to previous studies [147-149, 157]. The value of Young's modulus was varied until the best fit to the elastic portion of the experimental load-displacement curves was obtained numerically. The values of Young's modulus and Poisson's ratio were then fixed in further analyses.

In the EPF model, von-Mises plasticity with a constant slope for the plastic portion was utilized. An initial yield strain ε_y and plastic slope E_p were considered and varied to achieve the best fit between the load-displacement graphs of the experiments and the model. The related yield stress σ_y was obtained by multiplying the yield strain by the Young's modulus. In the first iteration of the optimization procedure ε_y was taken as 0.6% according to [136, 148] while E_p was taken as 5% of the elastic portion slope according to [136]. After each simulation the red diamond points of Fig.3.1 were compared to the corresponding points obtained using the EPF model. The loads corresponding to the displacement of the marked points in Fig.3.1 were obtained from the model using linear interpolation. The objective function minimized to find the best set of parameters was:

$$S = \sum_{i=1}^{n} (y(x_i) - y_i)^2, \tag{3.1}$$

where S is the sum of the squares of the errors, $y(x_i)$ is the load obtained from the EPF model corresponding to displacement x_i and y_i is the value of the experimental load.

Based on previous studies [136, 137, 148, 158-162], the maximum principal strain criterion was used for the initiation of cracks in the XFEM procedure for both the EPF and the EF models. In the EPF model, the maximum principal strain was varied to obtain a failure load identical to the point where the load drops in Fig.3.1. Since the load-displacement shows a very steep decline after the maximum load is attained, a relatively small value was chosen for the fracture energy in the EPF model.

For the EF model, the maximum principal strain and the fracture energy were varied to minimize the error between the experimental and numerical load-displacement graphs as described previously.

3.3.3 XFEM analysis on a segment of cancellous bone

After finding the material properties of a single trabeculae, the geometry of trabecular tissue was modeled to find the macroscopic behavior of the tissue. The Gross Anatomy Laboratory at

the University of Calgary provided micro-CT scan data of cancellous bone of human cadaver forearms [163]. ImageJ software was utilized to convert the μ-CT scan data into 3D STL geometry. Afterward, the data was imported to the Geomagic software to prepare a cropped cubic specimen with side lengths of 2.5mm. The 3D geometry of the cadaver radius and the cropped specimen are illustrated in Fig.3.3. The specimen was positioned such that the X and Y directions represent the anatomical transverse directions while the Z direction is the anatomical longitudinal direction (Fig.3.3). The material properties obtained from the single trabecula model were then used for the trabeculae within the cancellous bone model. In particular, elastic and plastic behaviors and damage evolution parameters including Max. principal strain and fracture energy were assigned to the cancellous bone specimen.

All simulations in the present study were conducted assuming a 2D plane-stress state. Four different slices in the XY-plane and four different slices in the ZY-plane were modeled (Fig.3.4), with each slice having a thickness of 625μm. The middle section of each slice was constructed from the 3D geometry and imported to the ABAQUS software [164-166]. Isolated parts of the cross-section were removed from the analysis.

The areas of the trabecular components of samples XY1, XY2, XY3, and XY4 were equal to 1.91, 1.66, 1.82 and 1.77 mm^2 respectively. Similarly, for the samples ZY1, ZY2, ZY3, and ZY4 the areas of the solid portion were equal to 1.95, 1.68, 1.22, and 1.85 mm^2 respectively. The solid fraction was calculated by dividing the area of the trabecular components by the area of square from which the specimen as extracted (2.5x2.5=6.25 mm^2). The solid fractions of samples XY1, XY2, XY3, and XY4 were equal to 0.31, 0.27, 0.29, and 0.28, respectively and for the samples ZY1, ZY2, ZY3, and ZY4 were equal to 0.31, 0.27, 0.2, and 0.3, respectively.

In all simulations, one side of the specimen in a particular direction was fully constrained and a displacement was applied on the other side of the specimen to the point where the load drops in load-displacement graph. The transverse (XY) specimens were loaded separately in the X and Y directions to determine the mechanical behavior in both transverse (medial-lateral and anterior-posterior) directions while the ZY specimens were loaded in the Z-direction to determine the longitudinal behavior in the proximal-distal direction (Fig.3.3). Each specimen was loaded in both tension and compression.

The element type and the other model parameters were set up using the same approach as explained in the previous section for the single trabecula. The same mesh sensitivity study was conducted for the 2D XFEM models of cancellous specimen. The load-displacement graphs revealed that the obtained load-displacement curve for an average mesh size of 0.015mm differed from that obtained with the mesh size of 0.01mm by less than 2%. We opted for reporting the results for the finer mesh. To develop a realistic model, several enrichment zones were defined for each 2D cancellous bone cross-section to allow for simultaneous initiation and propagation of multiple cracks. To develop a realistic model, 10 enrichment zones were defined for the cancellous bone specimen to allow for simultaneous initiation and propagation of multiple cracks. This was considered appropriate as the maximum number of simultaneous cracks that was observed in the models was 6. Selecting elements in such a complex geometry like trabecular tissue is time-consuming. In order to do so, all elements of the bone specimen were selected as one element set and the input file of the model was written. Afterward, the input file was edited, and the element set was split to ten element sets with an almost equal number of elements. Each element set was then defined as one enrichment zone. An initial crack location was not defined; the XFEM framework predicted the crack initiation location based on the developed stresses and strains and the defined damage parameters. The estimated material properties of the two material models (EPF, EF) for a trabecula segment were assigned to the cancellous bone tissue. A piece of input file of failure modeling (EPF model) in Cancellous Bone using XFEM is available in Appendix A.

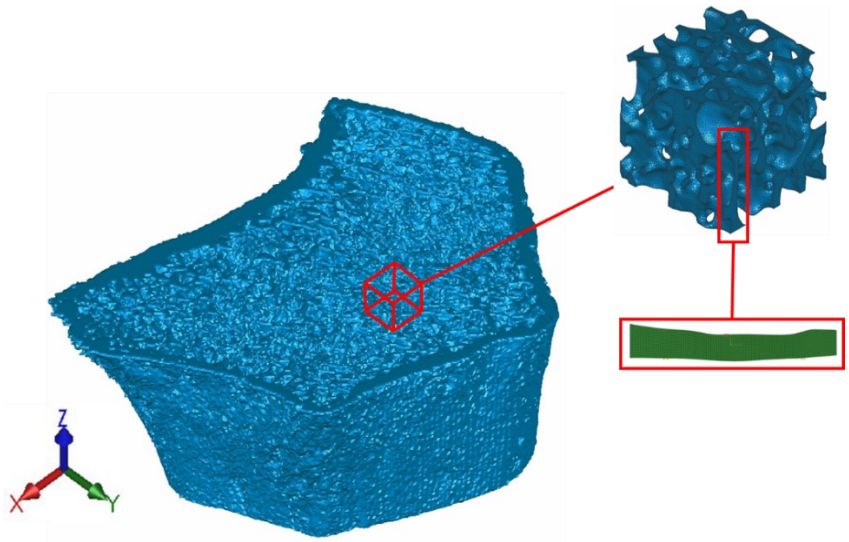

Figure 3.3. 3D geometry of radius used to create the geometry and mesh of the cancellous bone specimen

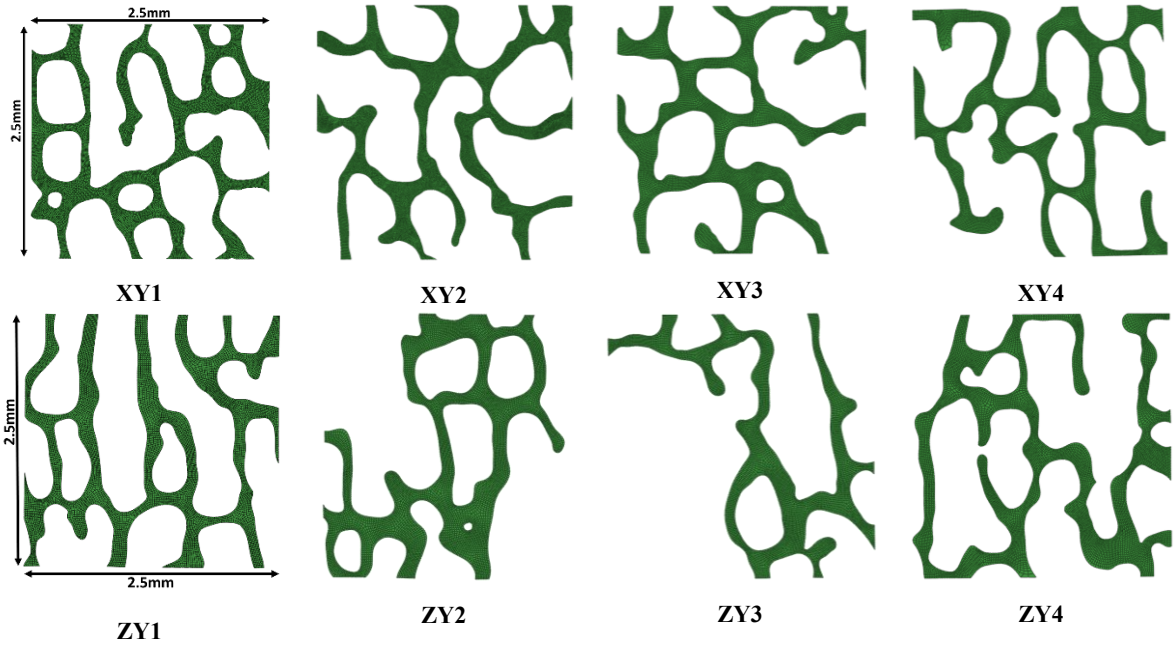

Figure 3.4. 2D sections of cancellous bone specimen in XY and ZY planes (All sections have the same size)

The load-displacement behavior for each material model was extracted for each cancellous specimen slice and the stress-strain curves were determined. The loads were calculated by summing nodal reaction forces on the fully constrained side of specimen. The bulk stresses were calculated by dividing the loads by the specimen cross-sectional area (2.5 mm × 625μm = 1.56 mm^2). The strains were calculated by dividing the displacement in a specific direction by the initial length of the specimen (2.5 mm).

The tensile and compressive strength for each material model in each direction was obtained as well as the averages along all axes. To determine the strength of the specimen in each direction for both material models, the maximum forces in each direction (for all section planes) were added together and divided by the section area. Additionally, the stiffness was determined for each condition from initial slope of the stress-strain curve. The strength and stiffness values for each material model were compared with the solid fraction in each specimen slice to determine if a correlation exists between these parameters.

3.4 Results

3.4.1 XFEM analysis of a single trabecula

For both EPF and EF models, the value of Young's modulus was estimated to be 4160MPa. The initial slope of both the EPF and the EF models almost exactly matched the initial experimental slope of the load-displacement graph (Fig.3.5).

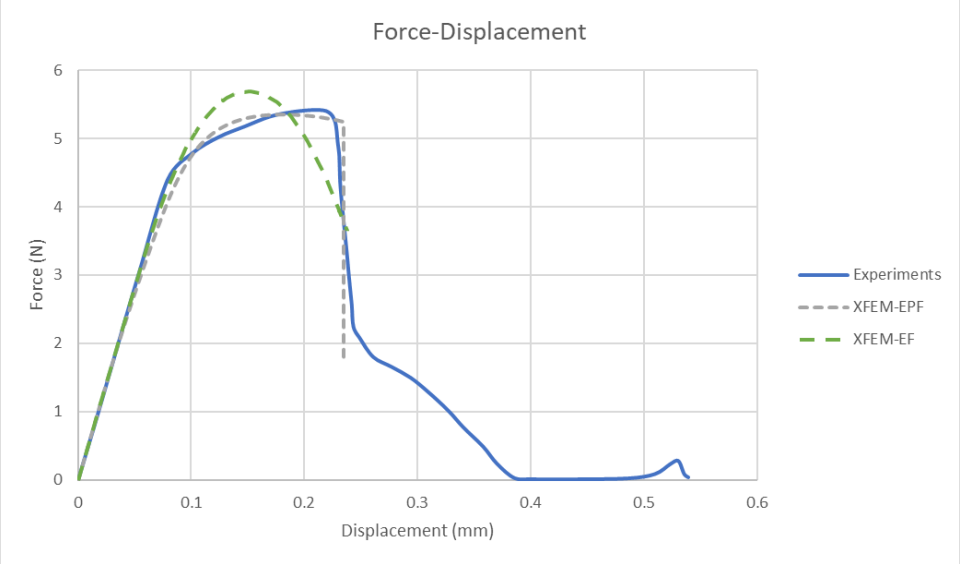

Figure 3.5. A comparison of load-displacement graphs of two material models with experiment graph

For the EPF model, the estimated σ_y, ε_y, and E_p were computed as 166.5MPa, 0.04 and 17.5MPa, respectively. The value of the maximum principal strain that causes fracture was estimated as 0.38. The fracture energy in the EPF model was taken as 10^{-2} mJ/mm^2 which is small value and enabled the model to simulate the sudden drop in the load beyond the ultimate load (Fig.3.5). The predicted ultimate plastic strain and stress for the material were calculated to be 0.34 and 172.5MPa, respectively.

For the EF model, the maximum principal strain and the fracture energy were varied to minimize the error between the experimental and numerical load-displacement graphs. The estimated maximum principal strain and the fracture energy to produce the best fit where found to be 0.03 and 9.2 mJ/mm^2, respectively.

The estimated material properties of both material models are shown in Table 3.1. A comparison between the load-displacement graphs of EPF and EF models and the experimental graph is illustrated in Fig.3.5. Also, the fractures in the trabecula for each material model are illustrated in Fig.3.6. As mentioned earlier, the errors of EPF and EF graphs compared to the experimental graph were obtained based on equation 3.1 and for the ten red diamond points that were marked in Fig.3.1. The final values for the objective function obtained for the EPF and EF models were 0.17 and 3.46, respectively. As can be observed in Fig.3.5, the combination of the ductile plasticity model and brittle XFEM model (EPF) was able to replicate the experimental graph much more smoothly than the EF model whose only source of ductility was the fracture energy parameter require in the XFEM model.

Table 3.1. Estimated material properties of two material models using trial and error

Material Behaviors		EPF	EF
Damage Evolution (XFEM) parameters	Max principal strain	0.38	0.03
	Fracture Energy (mJ/mm^2)	0.01	9.20
Elastic	Young's Modulus (MPa)	4160*	4160*
	Poisson's Ratio	0.3*	0.3*
Plastic	Yield Stress (MPa)	166.5**	-
	Ultimate stress (MPa)	172.5	-
	Yield Strain	0.04	-
	Ultimate Plastic Strain***	0.34	-

*These parameters were fixed based on the initial slope of the model.
**Obtained by multiplying the yield strain by the Young's modulus
***Plastic strain value corresponding to the ultimate stress

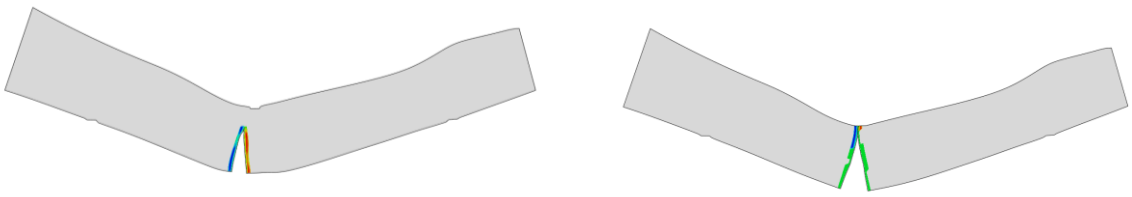

XFEM-EPF model **XFEM-EF model**

Figure 3.6. Crack propagation in trabecula using the two different material models

3.4.2 Results of XFEM analysis of cancellous tissue

The stress-strain curves in both tension and compression for each of the X, Y, and Z-directions are shown in Figs.3.7-3.9, respectively. Each figure contains both the EPF behavior and the EF behavior and each subfigure shows the results for the four different specimen slices. It can be seen from the figures that the specimens tend to exhibit brittle failure under tensile loading. This behavior is consistent in the three anatomical directions and in both material models. Under tension, the stress-strain curves are linear until failure where there is a sudden drop in the stress. Conversely, the under compressive loading the specimens tend to exhibit a more ductile failure. In these cases, there is a clear plateau in the stress-strain curve before failure and again this is consistent across the different directions and across the two material models. It can also be noted from the figures that the failure strain is higher in compression than in tension in the majority of the cases.

Compression

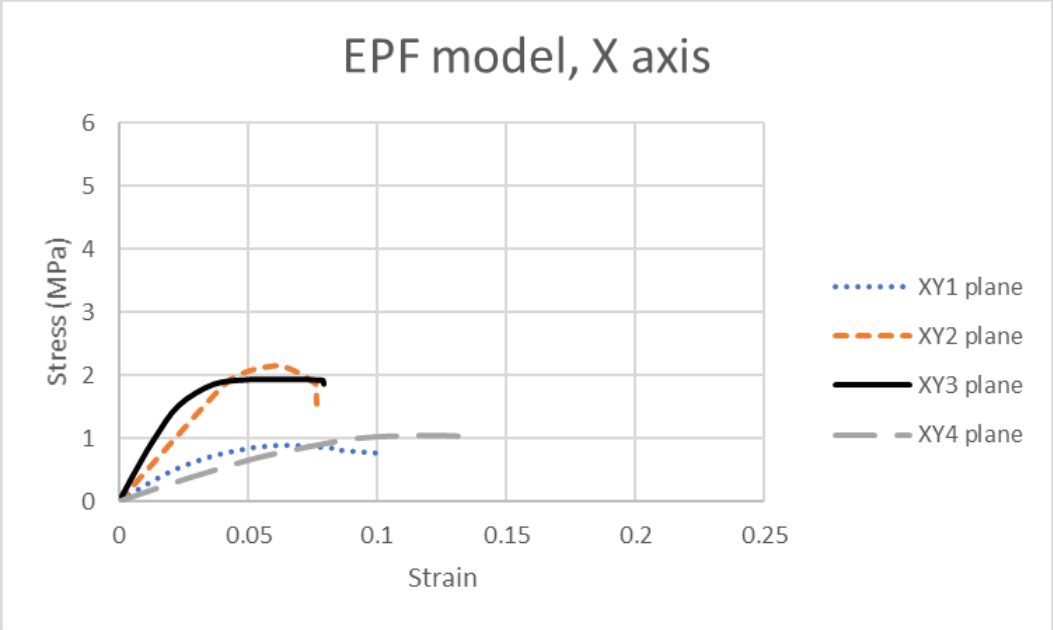

Compression

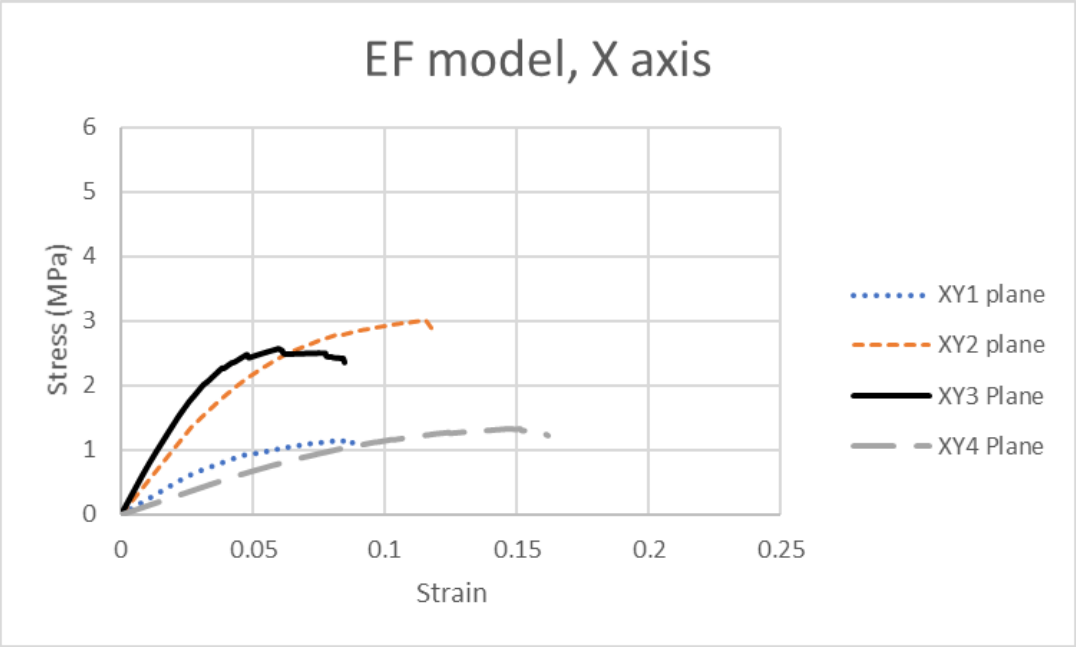

Tension

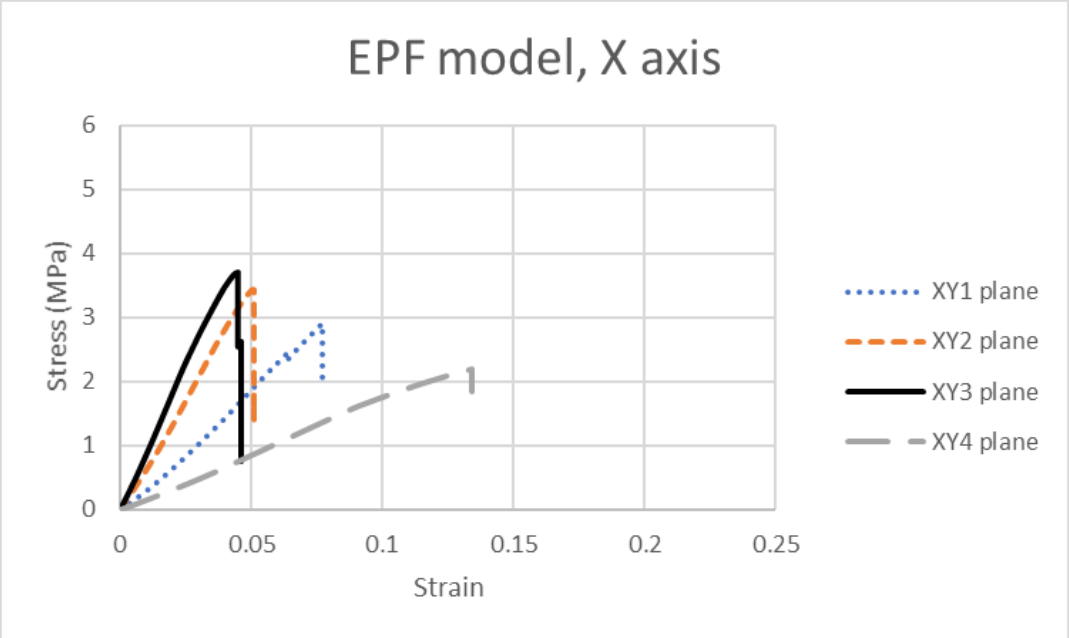

Tension

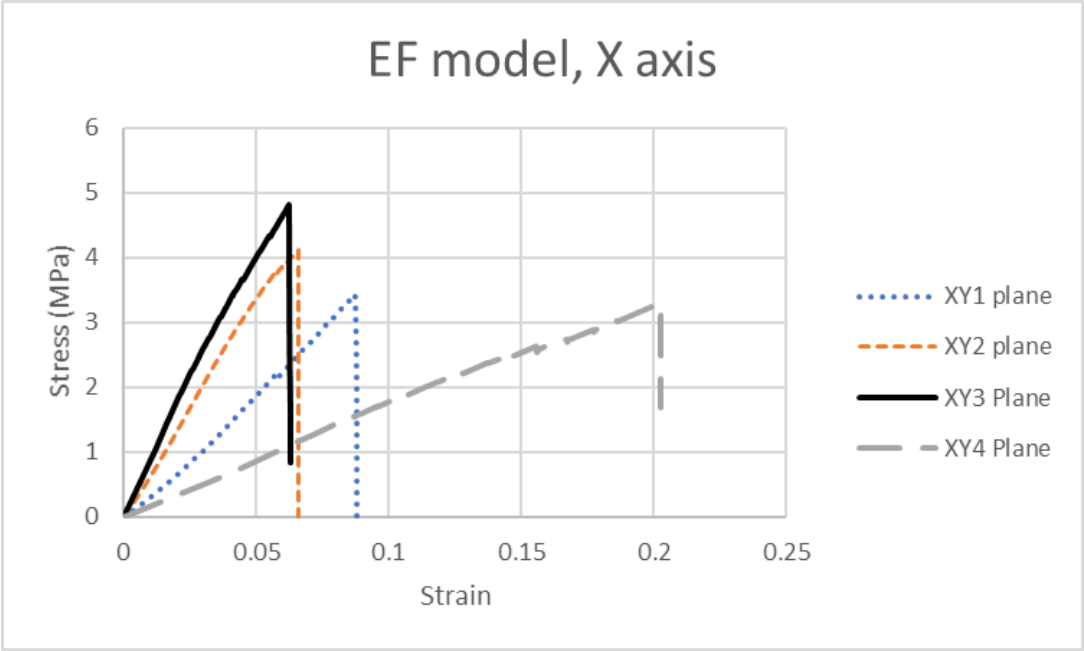

Figure 3.7. Stress-strain curves in the X-direction for compression and tension for both the EPF and EF models

Compression

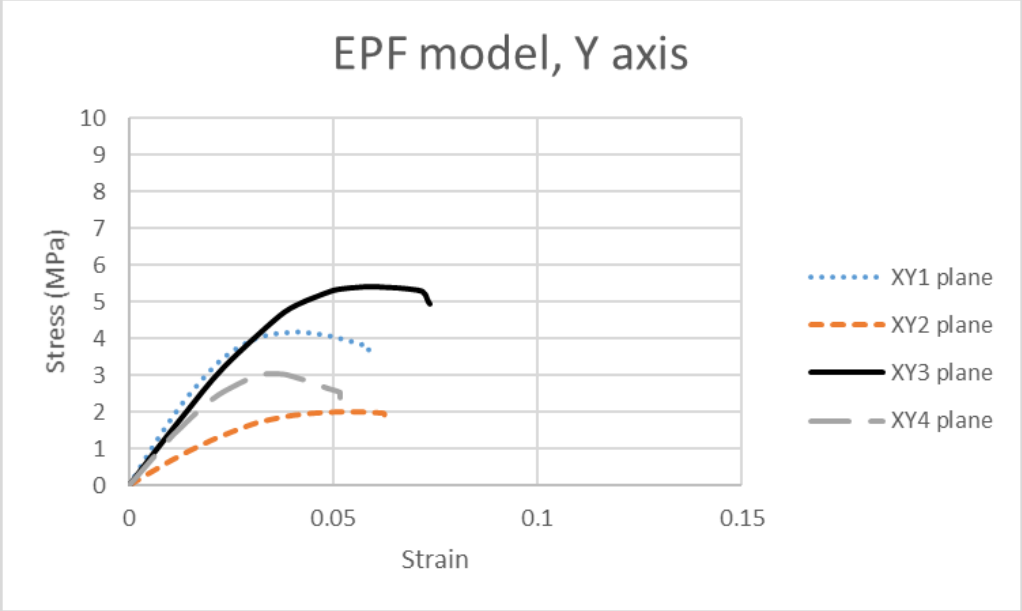

Compression

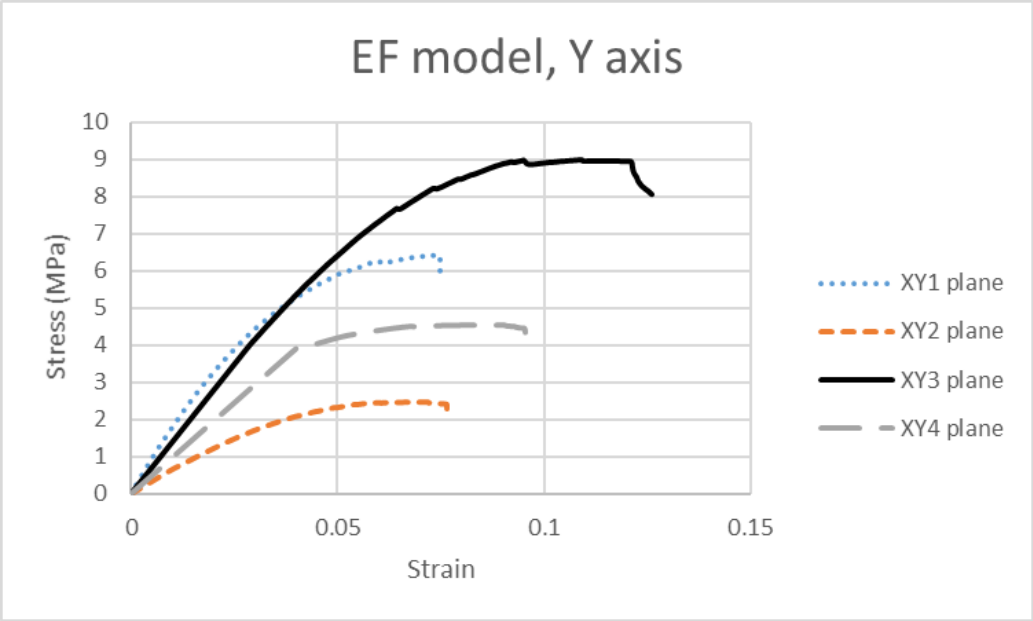

Tension

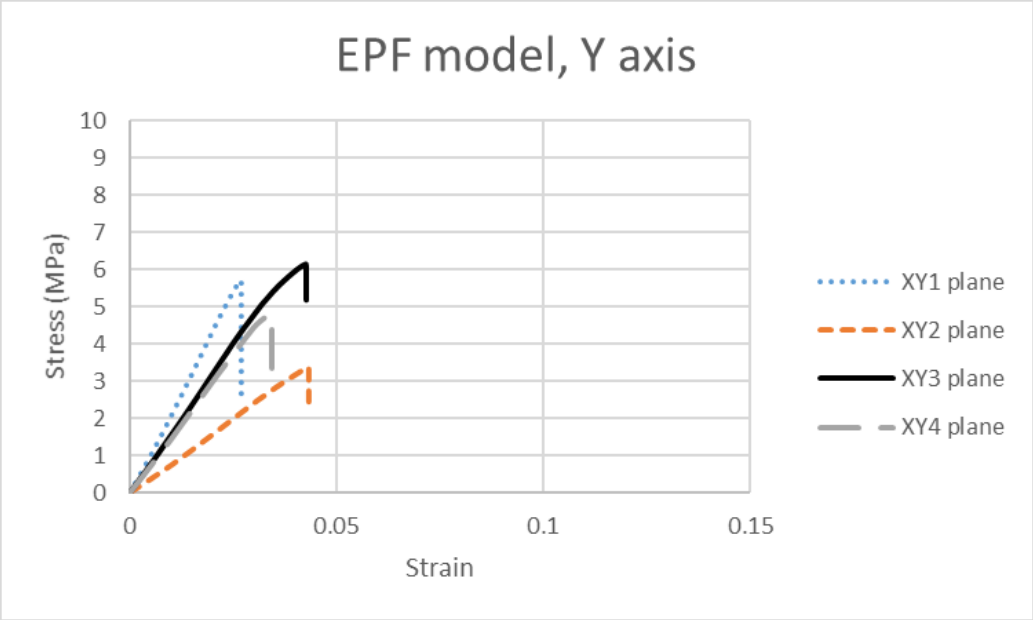

Tension

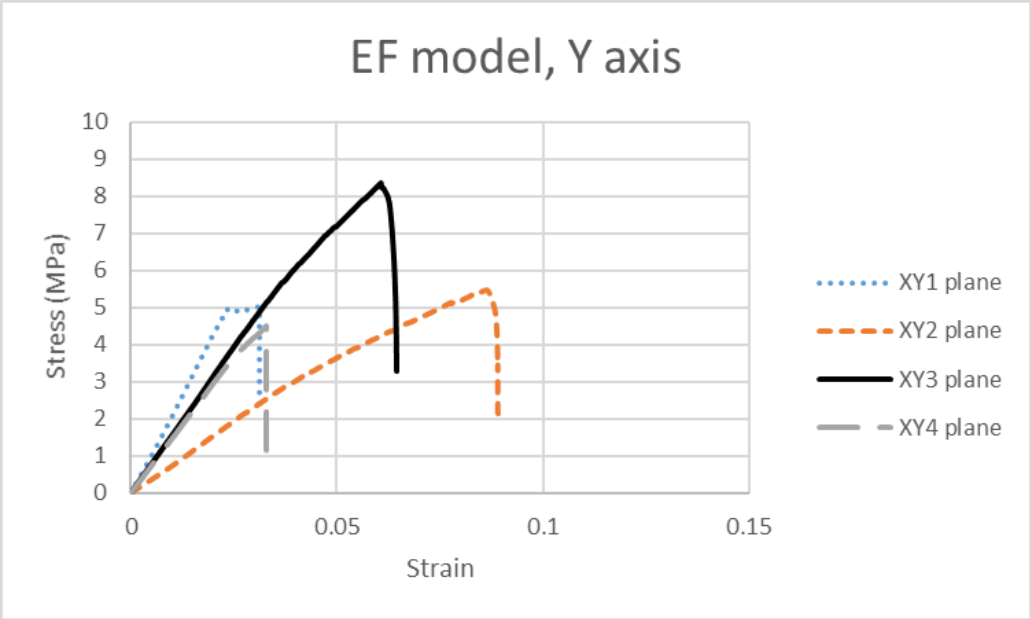

Figure 3.8. Stress-strain curves in the Y-direction for compression and tension for both the EPF and EF models

Compression

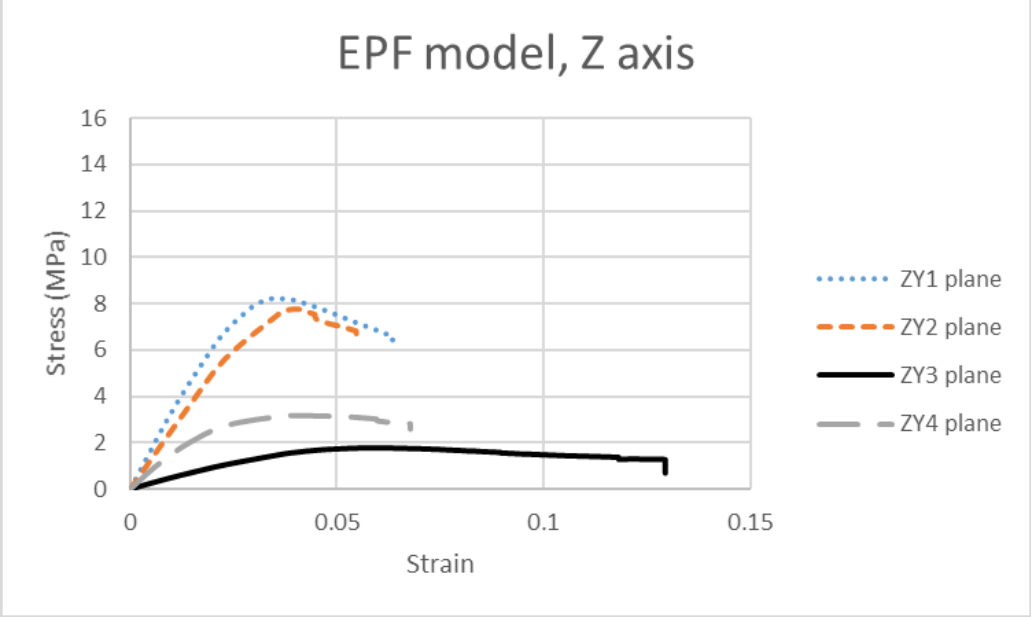

Compression

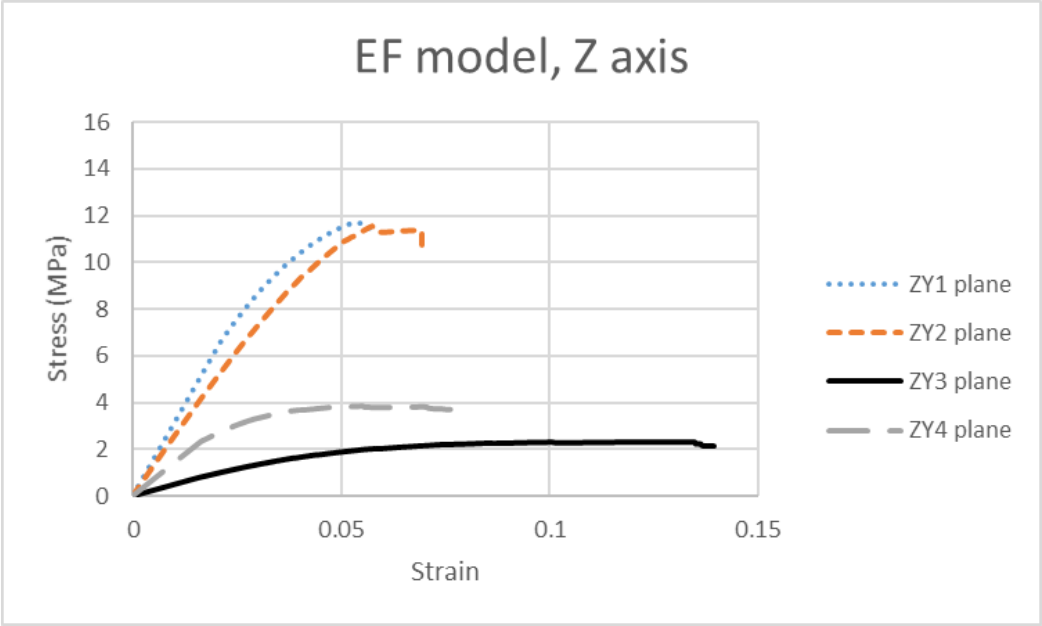

Tension

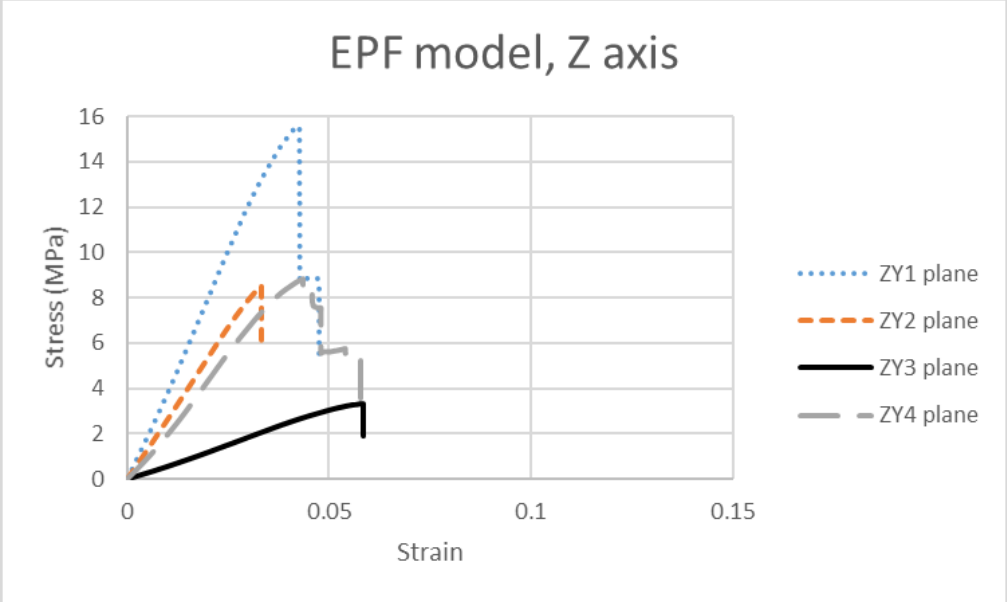

Tension

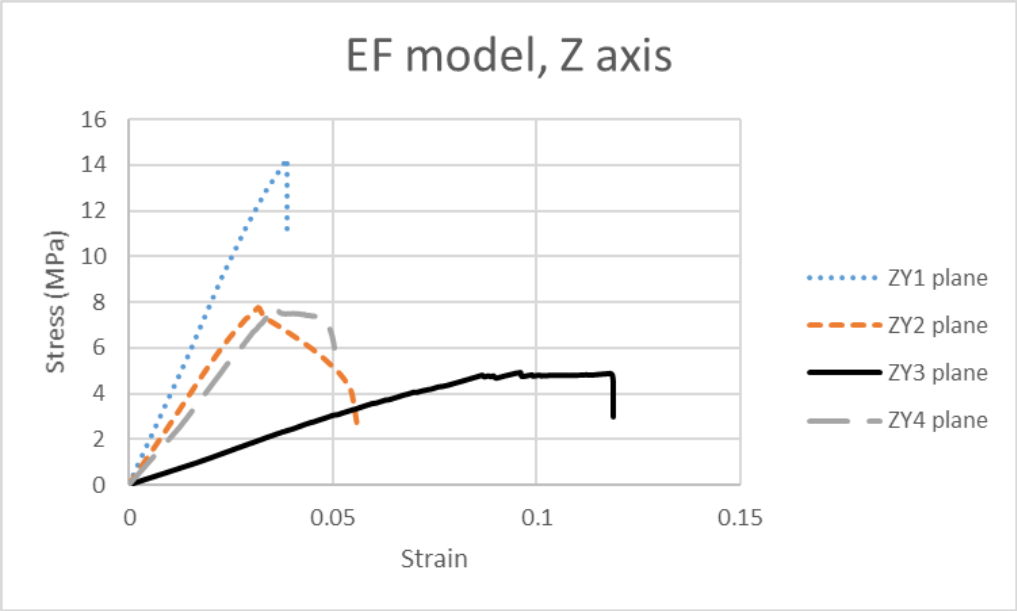

Figure 3.9. Stress-strain curves in the Z-direction for compression and tension for both the EPF and EF models

The tensile and compressive strength and stiffness values are shown for each material model in the X, Y, and Z-directions in Tables 3.2-3.4. In each direction, the strength tends to be higher in tension than in compression. Additionally, the strength determined from the EF model tends to be higher than that obtained from the EPF model with the exception of the tensile strength in the Z (longitudinal) direction. For both tension and compression and both material models, the strength in the X (medial-lateral) and Y (anterior-posterior) directions tends to be relatively close with the Y-direction values being slightly higher. The strength in the Z-direction (proximal-distal) tends to be much higher with the exception of specimen ZY3 which has the lowest solid surface fraction.

On average, the stiffness tends to be higher in tension than in compression for each direction and each material model. In contrast to the strength, there appears to be no difference in stiffness between the two material models. There appears to be a large difference in the stiffness values between the different directions with the average stiffness increasing from the X-direction, to the Y-direction, to the Z-direction. It can be noted from tables that there is a high variability in the stiffness across the different specimens (high standard deviation values) and there is a large variability across the different directions with a range of 39.2 – 188.1 MPa in compression and

a range of 50.8 – 253.3 MPa in tension. This may indicate that the full 3D network of trabeculae needs to be considered to provide a more accurate representation of the specimen stiffness.

Table 3.2. X-Direction Compression and Tension Strength and Stiffness for the EPF and EF Models

Compression				
	X direction Strength (MPa)		X direction Stiffness (MPa)	
	EPF	EF	EPF	EF
Section XY1	0.89	1.15	23.70	23.80
Section XY2	2.15	3.00	45.80	51.10
Section XY3	1.93	2.57	73.40	70.10
Section XY4	1.05	1.33	14.10	13.80
Average (SD)	1.51 (0.63)	2.01 (0.91)	39.2 (26.4)	39.7 (25.7)
Tension				
	X direction Strength (MPa)		X direction Stiffness (MPa)	
	EPF	EF	EPF	EF
Section XY1	2.89	3.43	31.90	32.10
Section XY2	3.44	4.12	65.60	65.90
Section XY3	3.69	4.82	90.10	88.70
Section XY4	2.20	3.29	15.60	16.70
Average (SD)	3.06 (0.66)	3.92 (0.70)	50.8 (33.5)	50.9 (32.5)

Table 3.3. Y-Direction Compression and Tension Strength and Stiffness for the EPF and EF Models

Compression				
	Y direction Strength (MPa)		Y direction Stiffness (MPa)	
	EPF	EF	EPF	EF
Section XY1	4.17	6.41	172.60	168.80
Section XY2	1.99	2.49	61.70	62.20
Section XY3	5.41	8.98	140.90	139.10
Section XY4	3.03	4.53	118.30	97.40
Average (SD)	3.65 (1.47)	5.60 (2.76)	123.4 (46.8)	116.9 (46.8)
Tension				
	Y direction Strength (MPa)		Y direction Stiffness (MPa)	
	EPF	EF	EPF	EF
Section XY1	5.72	5.02	208.73	207.95
Section XY2	3.37	5.47	79.10	74.75
Section XY3	6.12	8.38	157.90	156.10
Section XY4	4.79	4.51	147.70	147.60
Average (SD)	5.00 (1.22)	5.85 (1.73)	148.4 (53.3)	146.6 (54.8)

Table 3.4. Z-Direction Compression and Tension Strength and Stiffness for the EPF and EF Models

Compression				
	Z direction Strength (MPa)		Z direction Stiffness (MPa)	
	EPF	EF	EPF	EF
Section ZY1	8.25	11.67	312.21	309.28
Section ZY2	7.78	11.54	247.81	251.89
Section ZY3	1.77	2.32	46.67	47.71
Section ZY4	3.17	3.86	145.90	141.30
Average (SD)	5.24 (3.26)	7.35 (4.96)	188.1 (116.6)	187.5 (116.4)
Tension				
	Z direction Strength (MPa)		Z direction Stiffness (MPa)	
	EPF	EF	EPF	EF
Section ZY1	15.55	14.25	399.60	392.70
Section ZY2	8.56	7.77	269.10	266.30
Section ZY3	3.31	4.94	58.30	58.90
Section ZY4	8.82	7.83	214.10	211.00
Average (SD)	9.06 (5.02)	8.70 (3.94)	235.3 (141.3)	232.2 (138.3)

Comparing the solid surface fraction values (reported in the Methods) with the strength and stiffness reported in Tables 3.2-3.4, there appears to be no direction correlation between these parameters. However, the solid surface fraction values for all sections except ZY3 are nearly the same with a range of only 0.04 (0.27 – 0.31). It can be noted that section ZY3 has a lower solid surface fraction (0.20) and was also found to have a lower strength and stiffness compared to the other Z-direction values (Table 3.4). Specimens with a larger variation in the microstructure allowing for a larger range of surface fraction values should be analyzed to determine if correlations exist with either strength or stiffness.

Fig.3.10 shows and example stress distribution in the XY4 section using the EPF model with tension applied in the X (Fig.3.10a) and Y (Fig.3.10b) directions. It can be seen that a major part of the stress is distributed only in some regions of the cross-section as opposed to across the entire section. This suggests that alignment of the trabecula contribute to the strength in each direction in addition to the solid surface fraction.

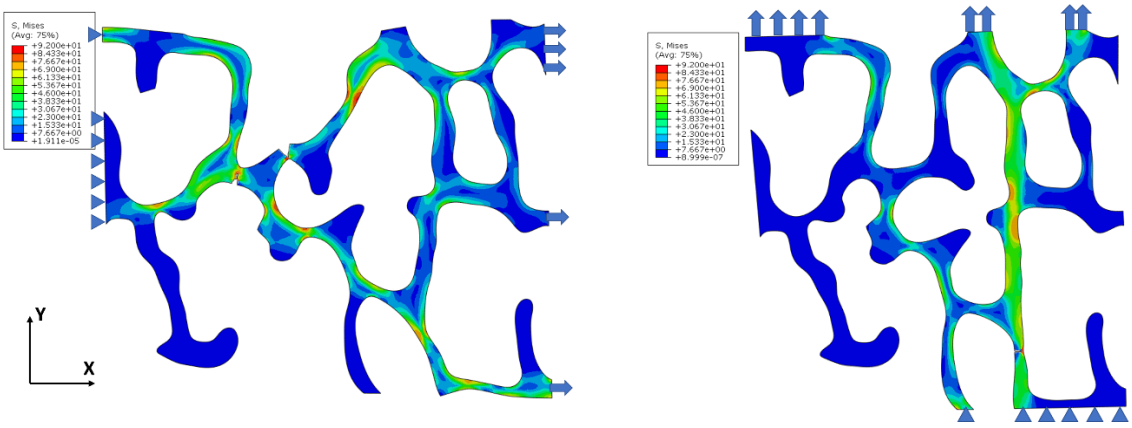

(a) **(b)**

Figure 3.10. (a) Von-Mises stress in a model loaded in the X direction (XY4 section, EPF model) (b) Von-Mises stresses in a model loaded in the Y direction (XY4 section and EPF model) (stresses in MPa)

3.5 Discussion

In this study, a single trabecula was modeled under bending using XFEM to determine material properties through calibration with previously published experimental work. The estimate material properties were then employed in two material models, namely an elastic-plastic-fracture (EPF) model and an elastic-fracture (EF) model in XFEM to predict the behavior of 2D trabecular specimens.

From the XFEM model of a single trabecula, the Young's modulus was determined to be 4.16 GPa using both the EPF and EF models. The stiffness values reported in literature for a single trabecula have a large variability and may depend on various factors such as site and orientation [167, 168]. The results obtained here are consistent with the lower spectrum of the range of values reported by Yamada et al. [169] for a single trabecula in bovine cancellous bone (4.5 – 23.6 GPa) and within the range reported by Szabo et al. [170] (1.13 - 16.46 GPa). The maximum tensile strain at failure was determined to be 0.38 (Table 3.1) which lies within the range reported in literature (0.1422 – 0.6165)[170]. The Yield stress found here (166.5 MPa; Table 3.1) is within the range of values reported by [171] for human trabecula under bending from older donors (157.1 $\pm$ 21.8 MPa), while the ultimate stress found here (172.5 MPa) is lower than that reported by [171] (252.29 $\pm$ 39.13) for the same donors.

The EPF model was able to replicate the experimental behavior much better than the EF model (Fig.3.5). The reason behind the success of the EPF model can be explained by investigating the force-displacement curves. In particular, the load displacement curve is elastic followed by a “ductile” or “yielding region”, followed by a sudden drop. This can be achieved better by utilizing a plasticity model followed by XFEM with low fracture energy. The EF model however, has a ductile behavior but is not capable of replicating the yielding region shown experimentally.

Although EPF model is better suited to replicate the obtained experimental behavior, simulations run using this model it can exhibit convergence difficulties due to the associated strain-softening, stiffness degradation, and unstable cracks propagation [37, 59, 172-174]. The structural response will be nonlinear and non-smooth by fracture [59]. Furthermore, the ductile or quasi-brittle materials with nonlinear behaviors make the converging conditions worse compared to brittle materials with linear behaviors. In the present study, simulations run using the EF model exhibit faster convergence due to assumption of brittle behavior of cancellous bone tissue. In simulations with larger samples, in 3D XFEM or with finer mesh the convergence of EPF model might be more difficult and EF model can be an appropriate replacement for ductile material models. From the results of both material models, it can be concluded that a ductile model is better suited to model a single trabecula rather than quasi-brittle. In [142-144], it is concluded that cancellous tissue is quasi-brittle material with the same mechanical properties of cortical tissue at the micro level. However, in most of studies [136, 143-147], it is considered and shown that cancellous tissue is a ductile material. Based on our results, we agree with the latter conclusion.

There are two approaches for modeling material properties of bone tissue that have so far been reported in the literature. In some studies, both cortical and cancellous tissues are assumed to be quasi-brittle materials with the same properties at the micro level [142-144]. However, in most research, only the cortical bone is considered to be quasi-brittle, and the cancellous tissue is assumed to be a ductile material [136, 143-147]. In this paper, the results support the contention that cancellous bone in micro-scale shows ductile behaviors rather than quasi-brittle behavior. We found these papers [175, 176] describing the trabecular bone ductility. However,

to the best of our knowledge, we have not found any references that relate the ductile behavior to the material composition of the trabecular bone.

The single trabecular model was then employed to model the behavior of a trabecular network in 2 dimensions. The compression and tension behavior of the specimens were examined in three anatomical axes. In general, it was observed that the failure strains tend to be higher in compression than in tension (Figs.3.7-3.9), which is consistent with behavior reported by [161]. Additionally, the stress-strain curves in compression showed a more ductile failure of the structure compared to the tensile behavior. This is consistent with the result reported by [177] where it was noted that there was a more abrupt decline in the stress under tension than compression.

Røhl et al. [177] reported no significant difference in stiffness values under tension and compression with mean Young's modulus values of 483 MPa and 485 MPa, respectively. The stiffness values determined here in the three anatomical directions were much lower than those reported in literature (Tables 3.2-3.4) and varied in both direction as well as tensile/compressive behavior. This suggests that the full 3D network should be considered to more accurately capture the stiffness of cancellous bone. It is interesting to note that there was no difference in the stiffness values predicted between the two material models considered.

The ultimate strength of cancellous bone reported by Røhl et al. [177] was 2.22 ± 1.42 MPa in compression and 2.54 ± 1.18 MPa in tension. These are close to the values determined here for strength in the X-direction (1.51 – 3.92 MPa; Table 3.2) and on the same order of magnitude as values determined in the Y and Z-directions (3.65 – 5.85 MPa; Table 3.3 and 5.24 – 9.06 MPa; Table 3.4). In this study, we estimated the strength to be higher in tension than in compression, which is consistent with Røhl et al. [177]; however, this trend is opposite to the behavior reported by Keaveny et al. [161]. The predicted forces obtained using the EF model were almost always greater than those predicted using the EPF model. This difference can be related to plastic behavior of EPF model compared to EF model with only elastic behavior.

According to previous studies [147, 157, 178-181], mechanical characteristics including elastic modulus and ultimate strength are different in various directions based on the volume fraction

or density of specimens, fabric orientation of the bone and anatomical locations of the specimens. The tensile test of seven cancellous bone specimens are conducted in [182] and the reported maximum, minimum and average tensile strength are 24.62MPa, 10.28MPa and 18.56MPa, respectively. A comparison of reported strength and the strength in table 4.4 demonstrates that the strength values obtained in this study are in the good agreement with those reported in [182]. Also, in [147, 157] it is experimentally shown that the strength in the longitudinal direction (Z direction in our study) is 159% greater than transverse directions (X and Y directions) which is what we observed in our study. This study [178], proved the same hypothesis, greater strength in longitudinal direction compared to transverse direction, based on fabric orientation of cancellous bone tissue in longitudinal and transverse directions.

In the current study, our aim was to find the best model that would fit the experimental behavior of cancellous bone. This study presents the first 2D XFEM model to predict strength and stiffness of cancellous bone as a function of the structure. The solid surface fraction in this study comprised a narrow range so it was difficult to directly correlate this parameter with the strength and stiffness values; however, in the Z-direction it was noted that the specimen with the lowest solid surface fraction indeed had the lowest strength and stiffness. This technique presented here shows promise to be able to model the behavior of trabecular bone.

It is important to note that the size of our micro-scale models (2.5cm^3) is smaller than the size of specimens in the reported experiments, which often range between 5 and 10 mm [146, 183, 184]. Also, the results were obtained from one specimen and should be extended to several larger specimen from various anatomical locations. To the best of our knowledge and as mentioned in the Abaqus documentation, crack branching in one element is not possible. Also, crack propagation in an element that already is separated to two elements is not possible. However, propagation of multiple cracks simultaneously is possible in Abaqus. Future work will implement the technique in 3D and will apply the technique to trabecular structures with varying density to correlate tensile and compressive strength and stiffness with density. Finally, the results of 2D and 3D XFEM models will be compared together as well as to the results of experimental tests conducted in our lab.

Chapter 4 : An equivalent constitutive model of cancellous bone with fracture prediction

4.1 Abstract

Objective: To simulate the mechanical and fracture behaviors of cancellous bone in three anatomical directions and to develop an equivalent constitutive model.

Method: Micro-scale XFEM models of a cancellous specimen were developed with mechanical behaviors in three anatomical directions. An appropriate ABAQUS macro-scale model replicated the behavior observed in the micro-scale models. The parameters were defined based on the intermediate bone material properties in the anatomical directions and assigned to an equivalent non-porous specimen of the same size. The equivalent model capability was analyzed by comparing the micro- and macro- models.

Results: The hysteresis graphs of the micro-scale model show that the modulus is the same in loading and unloading; similar to the metal plasticity models. The strength and failure strains in each anatomical direction are higher in compression than in tension. The micro-scale models exhibited an orthotropic behavior. Appropriate parameters of cast iron plasticity model were chosen to generate macro-scale models that are capable of replicating the observed micro-scale behavior of cancellous bone.

Conclusion: Cancellous bone is an orthotropic material that can be simulated using a cast iron plasticity model. This model is capable of replicating the micro-scale behavior in FE analysis simulations without the need for individual trabecula, leading to a reduction in computational resources without sacrificing model accuracy. Also, XFEM of cancellous bone compared to traditional FEM proves to be a valuable tool to predict and model the fractures in the bone specimen.

4.2 Introduction

One of the requirements for implementing an accurate model of bone fracture is considering fracture mechanisms in the cortical and cancellous tissues. In a macro-scale model, it is not practical to include the porous microstructure of cancellous bone, because of the huge volume of details on the micro-scale level of cancellous bones. Several studies [40-50, 52, 56-58, 148] have modeled fracture mechanisms in cortical bone at the macro- and micro-scales. However, to the best of our knowledge there is only one study [75] that modeled microcracking in cancellous bone by FE modeling. In that study, Hammond et al. [75] utilized Extended Finite Element Method (XFEM) to demonstrate crack formation in the cancellous bone.

Modeling the large volume of cancellous tissue porosity in FE modeling of bone requires large computational resources which renders such models impractical. Alternatively, a macro-scale model can be developed in which traditional continuum elements are used to model the trabecular tissue as a continuum without modeling the individual trabeculae provided they produce a behavior similar to that observed in the micro-scale models. There are several studies [60-69] which implemented various constitutive models to simulate micro-scale bone in a macro-scale. In some of these studies [60, 65, 66], the failure was not considered as part of the constitutive model and in the other studies [61, 62] damage mechanics was utilized to simulate post yield behavior of the micro-scale bone. However, the XFEM technique has some benefits compared to traditional damage mechanics [70-72] as it is able to model and predict fractures in different bones on multi-scale levels [3, 37, 54, 58, 73]. In the majority of the developed constitutive models, only one of the anatomical directions [60-62, 67] is considered. In addition, only the behavior of bone under compression [60-62] is considered. The objective of our work is to identify and implement a comprehensive macro-scale model that is able to consider the behavior in the different anatomical directions and in both compression and tension.

In this paper, 3D XFEM models of micro-scale cancellous bone were developed in which precise material properties of trabeculae were input. These models were used to generate the “macro-scale” material behavior along with the hysteresis loops associated with loading and unloading in both tension and compression. Finally, a built-in “equivalent” material model was

selected based on the obtained material behavior and the hysteresis graphs of cancellous bone specimen.

4.3 Methods

4.3.1 3D XFEM modeling of trabecular tissue

The XFEM framework built-into the general purpose finite element analysis software ABAQUS/Standard [59] was utilized to develop the 3D model. The Gross Anatomy Laboratory at the University of Calgary provided micro-CT scan data of cancellous bone of human cadaver forearms. ImageJ software was utilized to convert the μ-CT scan data into 3D STL geometry. Afterward, the data was imported into the Geomagic software to prepare a cropped cubic specimen with side lengths of 1.75 mm. The 3D geometry of the cadaver radius and the cropped specimen are illustrated in Fig.4.1. The specimen was positioned such that the X and Y directions represent the anatomical transverse directions, while the Z direction is the anatomical longitudinal direction (Fig.4.1).

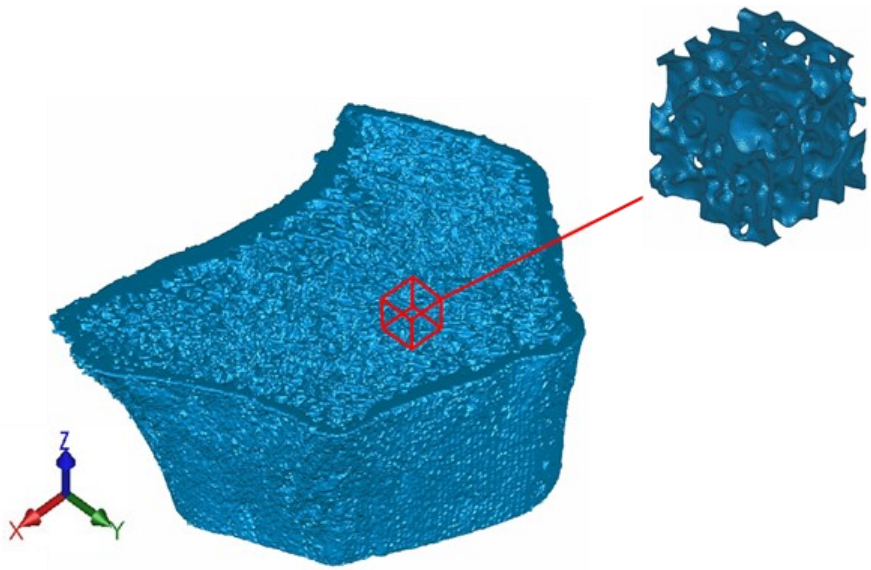

Figure 4.1. 3D geometry of radius and cancellous bone specimen

The material properties of cancellous bone and other XFEM parameters were assigned to the bone geometry as reported in Table 4.1. The material properties and XFEM parameters were obtained from a previous study [185]. The objective of this study [185] was to develop a 2D computational model using the built-in XFEM technique in ABAQUS that is capable of

predicting the fracture behavior of trabecular tissue. In order to do so, the experimental results of a three-point bending test obtained by Ridha et al. [148] were used to create a computational model capable of predicting the fracture of one trabecula. Using trial and error, the experimental load-displacement graph in [148] was used to calibrate the material properties of the trabecula for two material models with brittle and ductile behaviors. The predicted material characteristics of the trabecula were then utilized to predict the strength of the cancellous bone tissue of the forearm along three anatomical axes.

Table 4.1. Estimated material properties assigned to the 3D XFEM model [185]

Material Behaviors							
Damage Evolution (XFEM) parameters		Elastic		Plastic			
Max principal strain	Fracture Energy (mJ/mm^2)	Young's Modulus (MPa)	Poisson's Ratio	Yield Stress (MPa)	Ultimate stress (MPa)	Yield Strain	Ultimate Plastic Strain
0.38	0.01	4160	0.3	166.5	172.5	0.04	0.34

The finite element mesh consisted of 79295 C3D4 (4-node linear tetrahedron) elements with an average size of 0.03mm [59]. The chosen mesh size of 0.03m was considered adequate for the simulation since the average thickness of the trabecula was 0.1 which resulted in having 3 elements per thickness; an opposite number of elements to model crack propagation through the trabeculae. In addition, an initial mesh sensitivity study showed that the obtained stress-strain curve for a mesh size of 0.04mm differed from that obtained with the mesh size of 0.03mm by less than 5%. We opted for the finer mesh of 0.03mm which wasn't too onerous computationally. To develop a realistic model, 20 enrichment zones were defined for the cancellous bone specimen to allow for simultaneous initiation and propagation of multiple cracks. This was considered appropriate as the maximum number of simultaneous cracks that was observed in the model was 5. Selecting elements in such a complex geometry like trabecular tissue is time-consuming. In order to do so, all elements of the bone specimen were selected as one element set and the input file of the model was written. Afterward, the input file was edited, and the element set was split to several element sets with an almost equal number of elements. Each element set was then defined as one enrichment zone.

In all simulations, one side of the specimen in a particular direction was fully constrained and a displacement was applied on the other side of the specimen until the load dropped in the load-displacement graph. The behavior of the specimen was investigated in both tension and compression.

The load-displacement behavior for each direction in tension and compression was extracted and the stress-strain curves were determined. The loads were calculated by summing nodal reaction forces on the fully constrained side of the specimen. The bulk stresses were calculated by dividing the loads by the specimen cross-sectional area ($1.75\ mm \times 1.75\ mm = 3.0625\ mm^2$). The strains were calculated by dividing the displacement in a specific direction by the initial length of the specimen (1.75 mm).

The initial slope of the stress-strain curves in tension and compression were estimated to obtain the value of Young's modulus in the anatomical directions. The yield point was determined by a straight line parallel to the initial slope of the curve but offset by 0.2% from the origin on the strain axis. The yield strength and strain were estimated by the projection lines from the yield point to the stress and strain axis, respectively. The maximum stress on the stress axis was considered as the ultimate strength and the strain of the point at which the stress has a sudden drop was considered as the failure strain. The Poisson's ratio of the bone specimen was defined in each individual direction from the ratio of lateral to axial strain in tension and compression.

4.3.2 Hysteresis model

The developed 3D XFEM models were modified to extract the hysteresis graphs of the bone specimen. All model parameters were set up using the same approach as explained in the previous section. The XFEM model of the bone specimen in each anatomical direction was loaded cyclically between tension and compression. The applied displacement was reversed at various points in the loading process between the yield and failure points. The points were selected based on the failure strain in each direction as well as tension and compression. Unloading was then performed at one third of, two thirds of, and exactly at the failure strain. The unloading in the X direction was applied at strain values of 0.028, 0.040 and 0.055 in tension and the strain values of 0.063, 0.126 and 0.189 in compression. The unloading in the Y

direction was applied at strain values of 0.043, 0.063 and 0.080 in tension and the strain values of 0.050, 0.099 and 0.149 in compression. The unloading in the Z direction was applied at strains of 0.046, 0.051 and 0.057 in tension and strains of 0.075, 0.100 and 0.143 in compression.

4.3.3 Equivalent model

After finding the material properties of micro-scale cancellous specimen, a constitutive model with similar mechanical characteristics of the bone was selected from built-in material models of ABAQUS software. The intermediate behavior of the three anatomical directions of the bone specimen was used to estimate the parameters of the equivalent material model.

The XFEM framework was utilized to define failure in the equivalent model. The XFEM parameters were chosen so that failure in the equivalent model was similar to that in the micro-scale model. A cube with the same size of bone specimen (1.75mm) with no porosity was used for the geometry of the equivalent model (Fig.4.2). The cube was then meshed by C3D8R (8-node linear brick, reduced integration, hourglass control) elements. The whole cube is defined as the enrichment zone, which allows XFEM to initiate and propagate a crack anywhere within this region. The micro-scale cancellous specimen and the equivalent (macro-scale) specimen with defined boundary conditions and loading in the Y direction are shown in Fig.4.2.

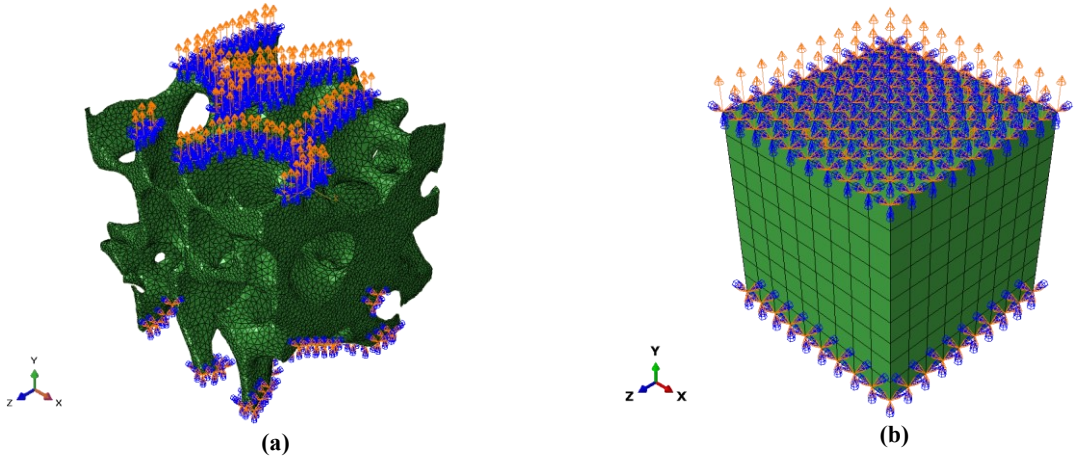

(a) **(b)**

Figure 4.2. Micro-scale cancellous specimen (a) and equivalent model (b)

The “Max Principal strain” criterion was utilized as the damage initiation criterion in the equivalent FE model. In the ABAQUS built-in crack initiation criteria, a compressive strain

does not initiate damage in an enriched element [59]. To define crack initiation criteria by simultaneous tensile and compressive strain and to use different strain in tension and in compression for failure in the equivalent model, a user-defined subroutine UDMGINI was implemented and applied to the model. The subroutine code is added in Appendix B. Also, A piece of input file of failure modeling in 3D Cancellous Bone using XFEM is available in Appendix C.

The stress-strain graph of the equivalent model in the tensile and compressive directions were then extracted and compared to that of the micro-scale model with the intermediate material properties of the three anatomical directions. The error between the stress-strain graphs were computed using equation 4.1 at discrete points throughout the loading process where linear interpolation was used when the exact values were not present.

$$S = \sum_{i=1}^{n} (y(x_i) - y_i)^2, \tag{4.1}$$

where S is the sum of the squares of the errors, $y(x_i)$ is the stress obtained from the equivalent model graph corresponding to strain x_i and y_i is the stress value of the micro-scale bone graph.

4.4 Results

In this section, the results are reported in three subsections. First, the results of 3D XFEM model of the trabecular tissue are presented, which include (i) stress-strain curves in three anatomical directions; (ii) Young's modulus; and (iii) stresses and strains at yield and failure points. Second, the results of hysteresis models including the hysteresis graphs and an interpretation of the graphs are reported. Third, the results of equivalent model are explained, which include the material model that has been used in the equivalent model, the material properties that have been assigned to the model, and finally a comparison of stress-strain curves of equivalent model versus micro-scale model.

4.4.1 3D XFEM modeling of trabecular tissue

The stress-strain graphs in the X (medial-lateral), Y (anterior-posterior) and Z (longitudinal) directions in tension and compression were extracted and are shown in Fig.4.3. Also, crack initiation and the extent of cracking at failure in the micro-scale models in the three loading directions are shown in Fig.4.4. It can be observed from the figure that the cracks, not surprisingly, initiated at thinner tissue members of the cancellous specimen. Fig.4.4 also shows that the cracks initiated in one area, and then spread out over the sample. Initiation of cracks in the specimen was not accompanied by a discernible effect on the overall stress-strain curve of the specimen (Fig.4.3). However, integration of several cracks and their simultaneous propagating caused a gradual decrease in the slope of the stress-strain curve followed by a sudden drop which we considered as the failure point (Fig.4.3).

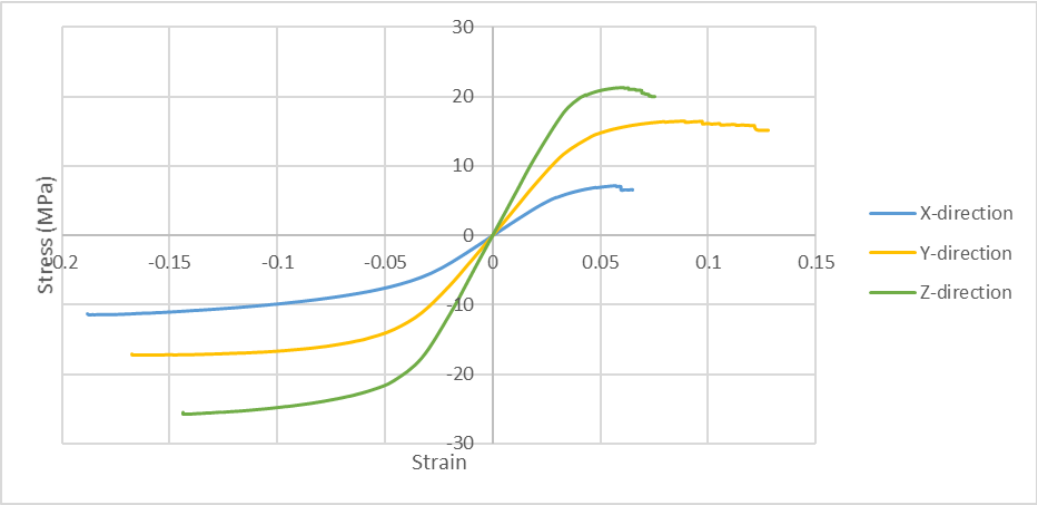

Figure 4.3. Stress-Strain in all anatomical directions in tension and compression

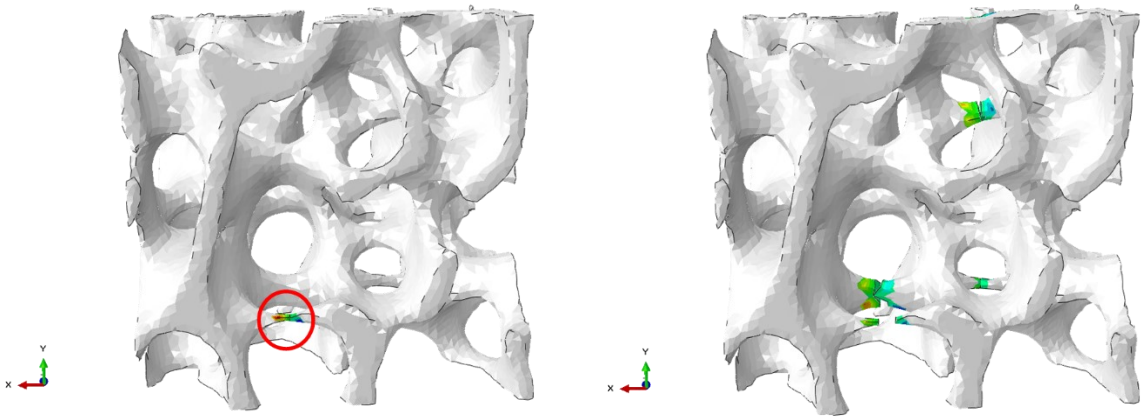

(a) (b)

X-Tension

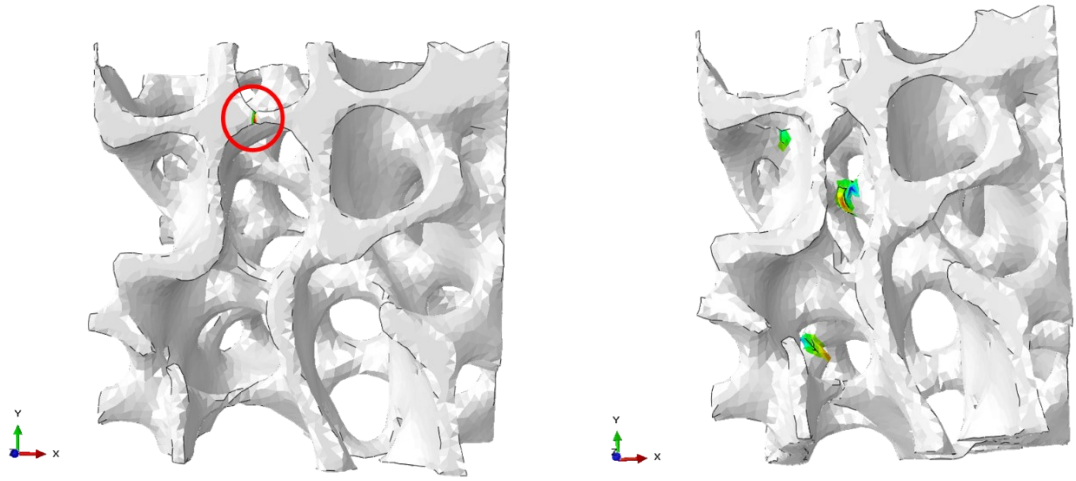

(c) (d)

X-Compression

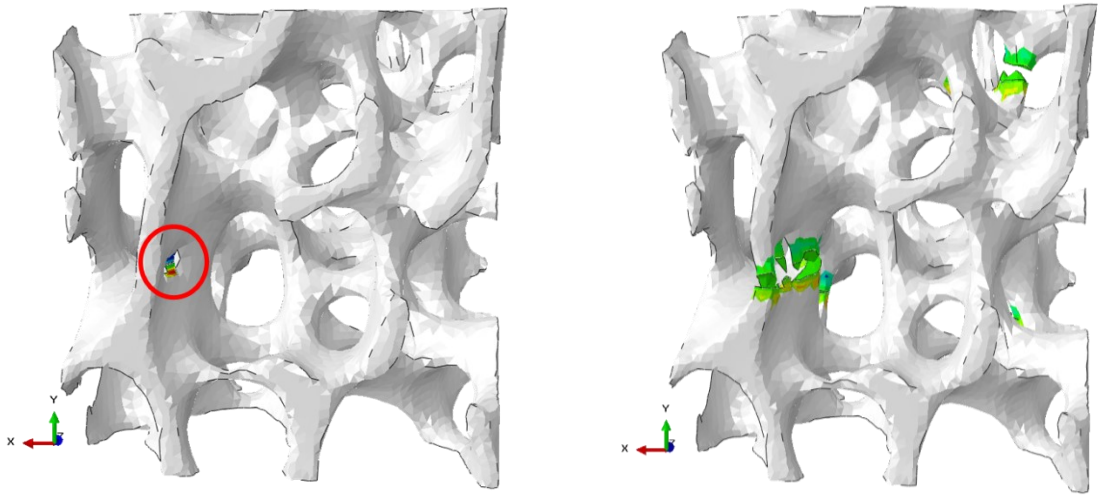

(e) (f)

Y-Tension

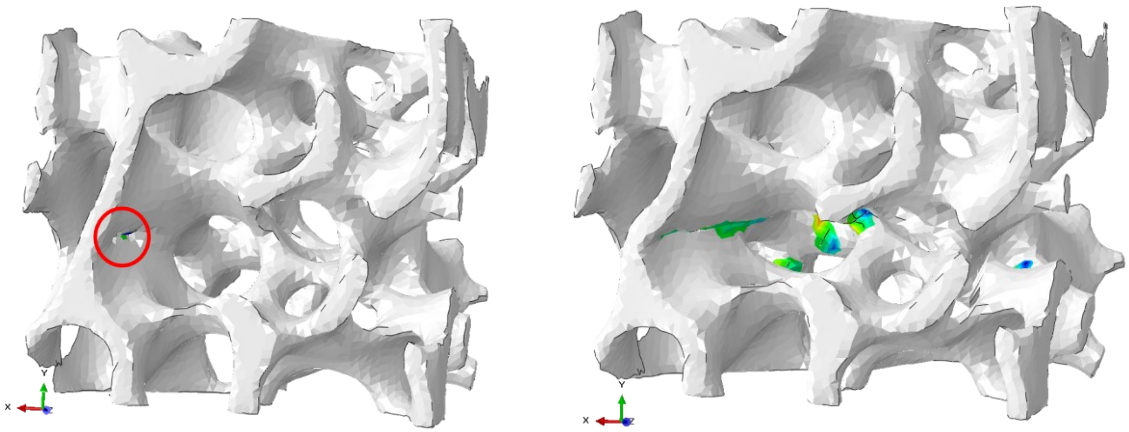

(g) (h)

Y-Compression

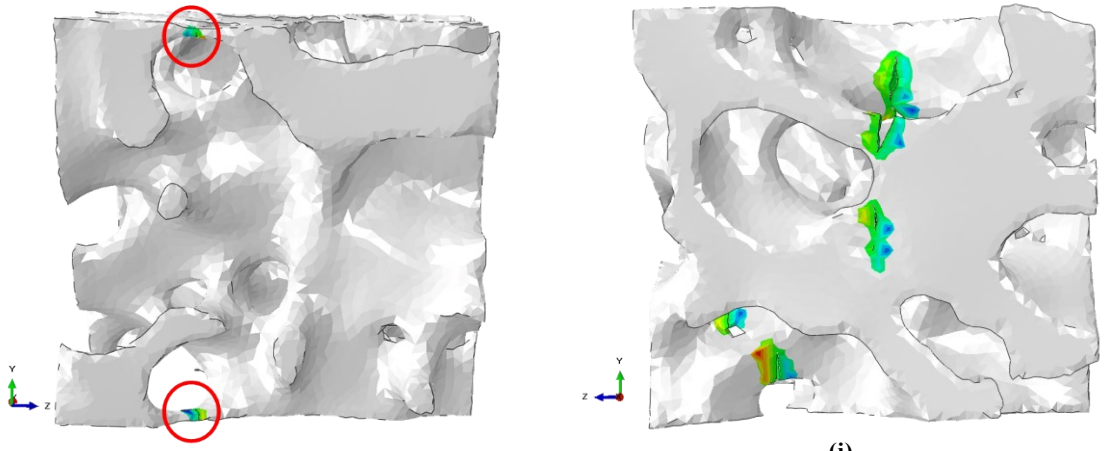

(i) (j)

Z-Tension

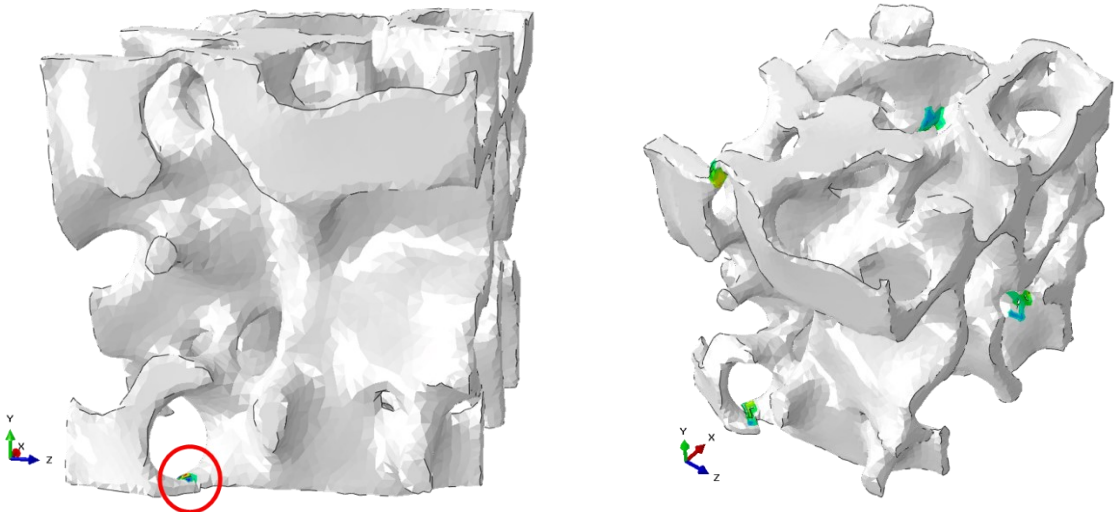

(k) (l)

Z-Compression

Figure 4.4. Crack formation in cancellous specimen in all axes at two loading stages (a),(c),(e),(i),(k) initial crack (b),(d),(f),(h),(j),(l) failure point

As it can be seen in Fig.4.3, the initial slope of each curve is the same in tension and compression, implying the material has the same stiffness. The estimated stiffness in the X, Y and Z directions were computed as 205MPa, 370MPa and 570MPa respectively. The stiffness in the Z direction is 178% higher than that in X direction and 54% higher than in Y directions. The yield strength and strain were estimated as described previously and are indicated in Table 4.2. It was observed that the yeild strength and strain were almost the same in tension and compression. Also, the same trend of stiffness values can be seen for the yield strength of X, Y and Z directions. The yield strength in the Z direction is 228% higher than that in X direction, and 50% higher than that in Y direction. The yield strain in the Y and Z directions are almost the same and slightly higher than that in X direction.

The ultimate strength and failure strain in each anatomical direction in tension and compression were estimated and are reported in Table 4.3. It can be noted from Fig.4.3 and Table 4.3 that the ultimate strength tends to be higher in compression than in tension and it tends to be higher in the longitudinal Z direction than the transverse Y and X directions. The compressive strength in the X direction is 60% higher than the tensile strength in the same direction. This pattern is repeated for the Y and Z directions with values of 5% and 21% respectively. The tensile strength in the Z direction is 196% higher than the X direction and 29% higher than the Y direction. Also, the compressive strength in Z direction is 123% higher than the X direction and 48% higher than the Y direction. It can be observed from the Fig.4.3 and Table 4.3 that the failure strain is higher in compression than in tension. In contrast to the ultimate strength, there appears to be no specific pattern in failure strains from X, Y and Z directions. In tension, the failure strain of the Y direction is 54% higher than X direction and 49% higher than Z direction. However, in compression the failure strain in the X direction is 12% higher than the Y direction and 31% higher than the Z direction.

The Poisson's ratio of the bone specimen was obtained for each direction as explained in the Methods section and indicated in Table 4.4. It can be seen that the computed Poisson's ratio values in tension and compression are almost the same.

Table 4.2. Estimated stiffness and yeild point strength and strain of trabecular tissue

Axis	Stiffness (MPa)	Tension		Compression	
		Yeild Strength (MPa)	Yeild strain	Yeild Strength (MPa)	Yeild strain
X	205	5.41	0.029	5.45	0.029
Y	370	12.14	0.034	11.30	0.033
Z	570	17.72	0.033	17.75	0.033

Table 4.3. Estimated mechanical behaviors of cancellous specimen by 3D XFEM model

Axis	Tension		Compression	
	Ultimate Strength (MPa)	Failure strain	Ultimate Strength (MPa)	Failure strain
X	7.2	0.057	11.5	0.188
Y	16.5	0.068	17.3	0.166
Z	21.3	0.059	25.7	0.143

Table 4.4. Estimated Poisson's ratio in each coordinate planes

Tension						Compression					
ν_{xy}	ν_{xz}	ν_{yz}	ν_{yx}	ν_{zx}	ν_{zy}	ν_{xy}	ν_{xz}	ν_{yz}	ν_{yx}	ν_{zx}	ν_{zy}
0.17	0.08	0.14	0.22	0.20	0.23	0.16	0.08	0.13	0.22	0.20	0.23

4.4.2 Hysteresis model

In order to find the best material model that behaves similar to the cancellous tissue, the hysteresis graphs were extracted and investigated. The hysteresis graphs of cancellous specimen in X, Y and Z directions are shown in Fig.4.5-4.7. As can be seen in the figures, Young's modulus of the specimen in all directions were determined to be the same in loading and unloading, which is similar to the traditional metal plasticity model. Also, the strength and failure strains are higher in compression than tension, which is a characteristic of the material model of the gray cast iron [59]. This characteristic of cancellous bone can be modeled by the cast iron plasticity model as reported in the literature [161].

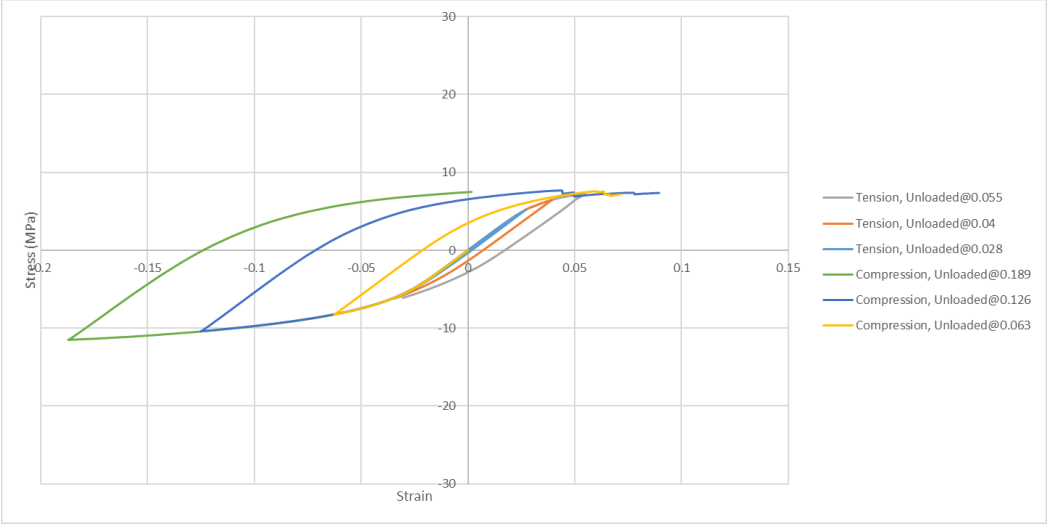

Figure 4.5. Hysteresis graph of cancellous specimen in X direction

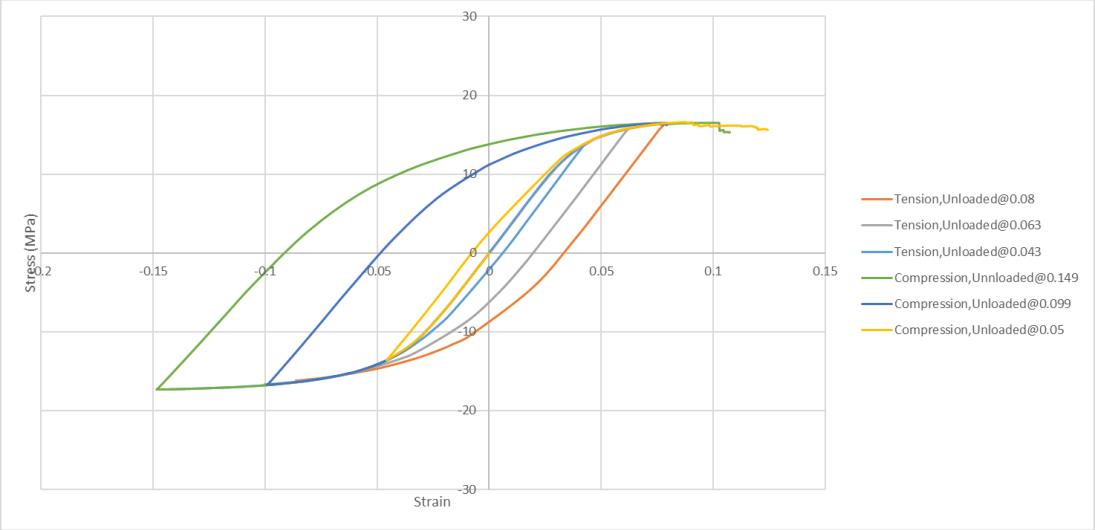

Figure 4.6. Hysteresis graph of cancellous specimen in Y direction

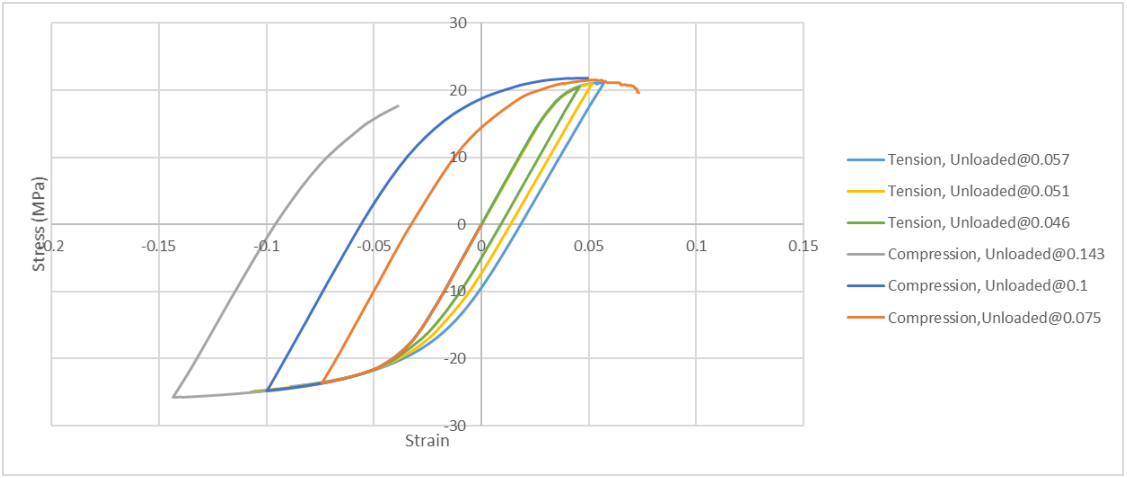

Figure 4.7. Hysteresis graph of cancellous specimen in Z direction

4.4.3 Equivalent model

The cast iron plasticity model was selected to for the equivalent FE model. Cast iron plasticity can be used for isotropic materials with the same behaviors in all directions. However, it can be noted from the Fig.4.3 that cancellous bone is an orthotropic material with different material behaviors in X, Y and Z directions. To utilize the cast iron plasticity model for the equivalent model, the intermediate values of behaviors from the three anatomical axes were estimated and assigned to the model.

As it can be observed in Fig.4.3, the stress-strain curve in the Y direction represented the intermediate values and those values were chosen (Table 4.5). The failure strain was calculated as the average value of failure strains along all directions and computed to be 0.068 in tension and 0.166 in compression. These values (0.068 and 0.166) were defined as maximum principal strain in tension and compression respectively. The fracture energy in both tension and compression were taken as 1 mJ/mm^2 which is a small value and enabled the model to behave in a brittle manner once the fracture strain is attained simulating a sudden drop in the load beyond the ultimate load. The other parameters are the values obtained from the Y direction model which are indicated in Tables 4.2,4.3 and 4.4.

Table 4.5. Material properties and XFEM parameters of the equivalent FE model

Damage Evolution (XFEM) parameters	Tension		Compression	
	Max principal strain	Fracture Energy (mJ/mm^2)	Max principal strain	Fracture Energy (mJ/mm^2)
	0.068	1	0.166	1
Elastic	Young's modulus (MPa)		Poisson's ratio	
	370		0.18	
Cast iron plasticity parameters	Tension				Compression			
	Yield Stress (MPa)	Ultimate stress (MPa)	Yield Strain	Ultimate Plastic Strain	Yield Stress (MPa)	Ultimate stress (MPa)	Yield Strain	Ultimate Plastic Strain
	12.14	16.04	0.0345	0.0335	11.3	17.3	0.033	0.133

The material properties from Table 4.5 were assigned to the equivalent model. The stress-strain curves of the equivalent model versus the micro-scale model are shown in Fig.4.8. The fractured specimen of the equivalent model in tension and compression are shown in Fig. 9(a) and (b), respectively. The output variable STATUSXFEM in Fig.4.9 shows the status of the enriched elements. The value of 1.0 (red) in Fig.4.9 means the enriched element is completely cracked and 0.0 (blue) means the element contains no crack. The value of STATUSXFEM lies between 1.0 and 0.0 if the element is partially cracked.

The sum of the squared error (Equation 4.1) of the equivalent model graph compared to the micro-scale model graph was obtained to be 40.61 for the sixteen points that are marked (red diamonds) in Fig.4.8.

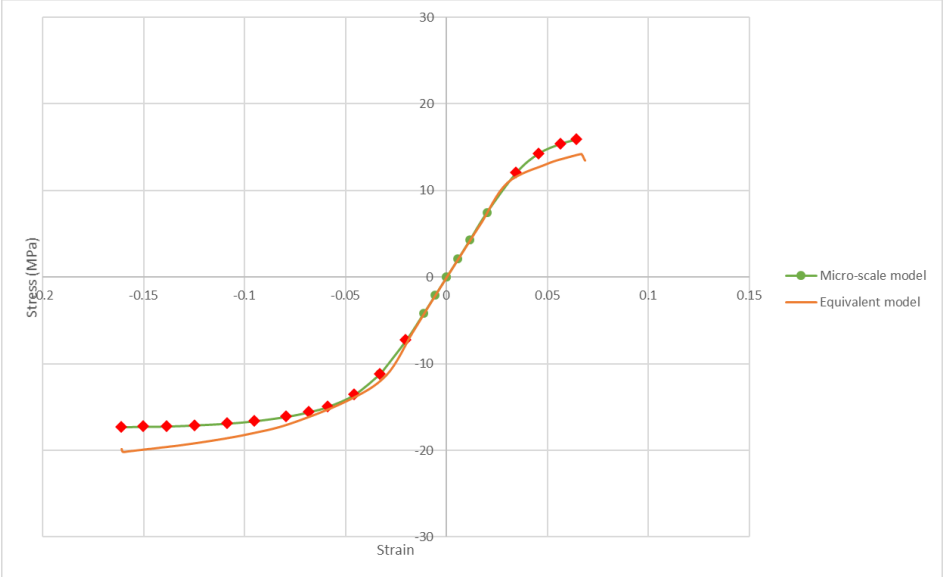

Figure 4.8. Stress-Strain curves of equivalent model vs. micro-scale model

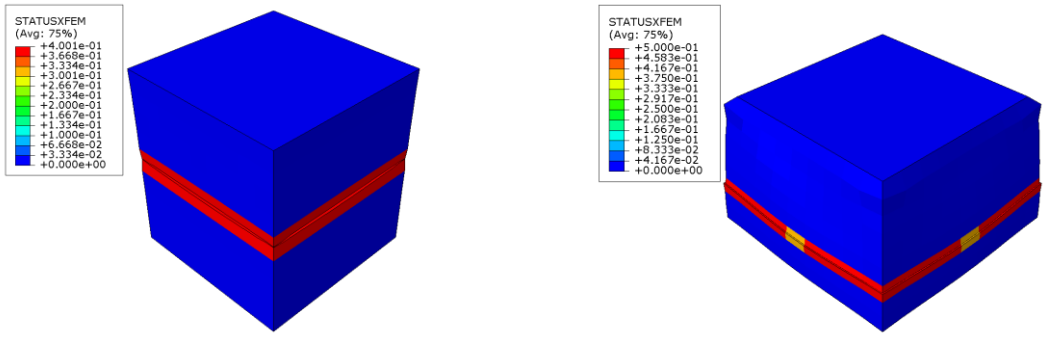

(a) **(b)**

Figure 4.9. Fractured specimen in equivalent model by (a) tensile loading (b) compressive loading

4.5 Discussion

In this study, 3D XFEM "micro-scale" models of cancellous bone specimens were developed. The material behaviors of the bone specimen along all anatomical directions were estimated and the intermediate values of material properties were determined. Additionally, the hysteresis graphs of the specimen were extracted to find the best material model similar to the micro-scale bone. Cast iron plasticity was then selected as a material model to develop an equivalent macro-model. The parameters of the cast iron plasticity model were then selected based on the intermediate material properties of cancellous bone and were assigned to the equivalent macro model. The stress-strain curves of the equivalent model versus those of the micro-scale bone specimen were compared to each other and demonstrated a good agreement.

The assigned material properties to the 3D micro-scale XFEM model were selected based on our previous work [185], in which 2D micro-scale XFEM models were developed to estimate material behaviors of trabecular tissue. In the previously developed 2D XFEM model, it was observed that the failure strains tend to be higher in compression than in tension [185], which is consistent with the results from the 3D XFEM model. Additionally, in the 2D XFEM model the trends of the strength and average stiffness values in the anatomical directions were consistent with the observations in the 3D XFEM model (Z direction were higher than Y direction and both values were higher than X direction. Conversely, in the 2D XFEM model of [185], the strength was estimated to be higher in tension than in compression, which is opposite to the trend of the 3D XFEM model. Also, in the 2D XFEM model, the average stiffness tends to be higher in tension than in compression for each direction while the 3D models estimated similar stiffness in tension and compression. In 2D XFEM model, the ultimate strength determined in the X, Y and Z-directions was 1.51 – 3.92 MPa, 3.65 – 5.85 MPa and 5.24 – 9.06 MPa, respectively [185]. As indicated in Table 4.3, the ultimate strength values in the 3D XFEM model were determined to be 7.2 MPa, 16.5 MPa and 21.3 MPa in the X, Y and Z directions, respectively, and such values are higher than the estimated ones in 2D XFEM model. The differences in the results of 2D and 3D modeling can be explained by the full network of trabecula in 3D compared to the in-plane network of trabeculae in 2D modeling. The 3D modeling is more realistic, and is expected to produce accurate results albeit at a much higher computational cost

From the 3D XFEM models of cancellous bone specimen, the Young's moduli in X, Y and Z directions were determined to be 2.05GPa, 3.7GPa and 5.7GPa respectively and they were equal in compression and tension. The stiffness values reported in the literature for the trabecular specimen have a large variability and may depend on various factors such as site and orientation. The results obtained here are consistent within the range of values reported by Ulrich et al. [186] for cancellous bone of human femoral head (3.5-8.6GPa). These results are also within the range of values reported by Hou et al. [187] (5.7±1.6GPa) and the reported values by Keaveny et al. [161] (4.45±2.57GPa for Proximal tibia and 4.4±12.71GPa for Proximal femur).

The graphs of Fig.4.3 demonstrated that the strength in compression tends to be higher than in tension, which is consistent with previous reports in the literature [136, 146, 157, 159, 161, 188]. The ultimate strength was determined to be in the range of 7.2-21.3MPa in tension and 11.5-25.7MPa in compression (Table 4.3) which are in the range of values reported by Keaveny et al. (7.63-23.1MPa in tension and 6.95-42.7MPa in compression) [159]. Also, the ultimate strength found by Verhulp et al. [182] was reported to be in range of 10.28-24.62MPa which is in a good agreement with the strength values obtained in the current study. The tensile and compressive yield strengths found here were similar and were in the range of 5.4-17.7MPa which lies within the ranges reported by Keaveny et al. [159] for the same donors as mentioned for yield strengths (6.9-22MPa in tension and 5.72-31.8MPa in compression). The range of tensile and compressive strains at failure were determined to be 0.057-0.088 and 0.143-0.188 respectively (Table 4.3) which are higher than those reported by Keaveny et al. for tension (0.0085-0.0187) and for compression (0.0115-0.0283)[159]. Also, the tensile and compressive yield strain found here (0.0285-0.0345) are higher than those reported by Keaveny et al. [159] (0.0067-0.0086 in tension and 0.0089-0.0142 in compression).

According to previous studies [147, 157, 178-181], mechanical characteristics including elastic modulus and ultimate strength are different in various directions based on the density of specimens, fabric orientation of the bone and anatomical locations of the specimens. Ford and Keaveny [179] determined the elastic modulus in the longitudinal and transverse directions to be in the range of 704-3700MPa and 306-1300MPa, respectively. A comparison of reported

stiffness values and those values shown in Table 4.2 reveals that the stiffness in the transverse direction (Y direction in our study) is in the range of reported values and the stiffness in the longitudinal direction (Z direction) is lower than those reported by Ford and Keaveny [179]. The same trend holds for the strength in longitudinal and transverse directions. In previous studies [66, 70] it was experimentally shown that the strength in the longitudinal direction (Z direction) is 159% greater than transverse directions (X and Y directions), which agrees with our results. Also, Shim et al. [3], determined greater strength in longitudinal direction compared to transverse direction, based on fabric orientation of cancellous bone tissue in the longitudinal and transverse directions.

The hysteresis loops of cancellous bone in loading and unloading cycles follow the same initial slope (i.e. Young's modulus), which is similar to the metal plasticity model. Also, the strength and failure strain are higher in compression than in tension, which can be seen in gray cast iron [59] which was also reported by Keaveny et al. [161, 189, 190].

The stress-strain curves in Fig.4.3 revealed that the cancellous bone is an orthotropic material with various behaviors in three anatomical directions, and such result is consistent with [147, 157, 178-181]. However, the cast iron plasticity model can be used for isotropic materials with the same behaviors in all directions [55]. To utilize the built-in material model for developing the equivalent specimen, the cancellous bone was considered to be initially isotropic with the intermediate material properties from three axial directions, which is a limitation of the present work. To evaluate the accuracy of the equivalent model, the stress-strain graphs of micro-scale bone and equivalent model were extracted and compared. The error of equivalent model compared to the micro-scale bone model demonstrated that the model has the potential to be a valuable tool for predicting the mechanical characteristics of a large-scale bone when it is not practical to include the porous microstructure of cancellous bone in the modeling.

In closing, the mechanical and failure behaviors of cancellous bone in three anatomical directions was developed with an equivalent constitutive model to predict the mechanical characteristics of cancellous bone. This was modeled using a 3D XFEM with cast iron plasticity model. This model is capable of replicating the micro-scale behavior without the need for modeling individual trabecula. This leads to a significant reduction in the required

computational resources without sacrificing the required model accuracy. Also, XFEM of cancellous bone compared to traditional FEM is able to predict and model the fractures in the bone specimen.

It is important to note that the size of our micro-scale models (1.75cm^3) is smaller than the size of specimens in the reported experiments, which often range between 5 and 10 mm [146, 183, 184]. Modeling larger specimens using our technique would require large computational resources and is considered impractical at this stage. Future work could investigate size effect by considering larger specimens.

The idea of using cast iron plasticity to model trabecular bone has been used previously by a few researchers [189, 190]. However, one of the limitations of this model is that it describes the mechanical response of a solid metal material with tension-compression strength asymmetry-its behavior under multiaxial compressive loading needs to be investigated further. In particular, the behavior in tension is governed by the maximum principal stress while the behavior in compression is governed by the pressure independent von Mises stress.

One of the recommendations arising from this study is extending the cast iron plasticity model to orthotropic materials and incorporating any observed pressure dependent failure criteria. Future work can then focus on calibrating the model for trabecular bone specimens and implementing it in a commercial finite element software-For example using UMAT in ABAQUS.

Chapter 5 : Prediction of fracture initiation and propagation in pelvic bones

5.1 Abstract

Objective: To develop an XFEM model that is capable of predicting different types of fracture in pelvic bone under various loading conditions.

Method: Previously published mechanical and failure characteristics of cortical and cancellous tissues have been implemented and assigned to an intact pelvic bone with specified cortical and cancellous tissues. Various loading conditions, including changing load direction and combining on different directions, have been applied to the acetabulum and different types of fracture (e.g., anterior/posterior wall fracture and transverse fracture) in pelvic bone have been modeled. The predicated types of fracture and the maximum force at fracture have been compared to those acquired from previously published experimental tests.

Results: The outputs of this approach contain types of fracture; also, the maximum force at fracture point have been compared to the previously published experimental tests of pelvic bone fracture. Anterior/posterior wall fracture and transverse fracture are the most common types of fractures in the simulations. The types of fracture that have been modeled were similar to the fractures in the experimental tests. Additionally, the maximum fracture force in the tests was defined to be 5.7kN. This value was estimated to be 18.6kN in the XFEM models.

Conclusion: The results revealed that different types of fracture in the pelvic bones can be caused by the various loading conditions in unstable conditions of high-rate impact loads. With proper mechanical and failure behaviors of cortical and cancellous tissues, XFEM model of pelvic bone is capable of predicting the fracture in the bone. Also, the XFEM models of cancellous and cortical tissues can be assigned to other bones in human body skeleton so that the failure mechanism in such bones can be investigated.

5.2 Introduction

Pelvic ring has a very important role in the human skeleton system as it links the upper body to the lower extremities [8]. The pelvic bone is one of the most stressed areas in the human anatomy due to its location for transferring the upper body weight to the lower limbs and for protecting the inner organs of that area [1, 2, 8]. Due to its important role, this bone has been the center of attention of surgeons and scientists since the early 20th century [8]. Because of the complex morphology of pelvic bone and its inaccessible location, surgeons and researchers have opted to use FE modeling for investigating rather than experiments.

Damage and fracture of the pelvic bone or acetabulum is a common type of fracture [6]. More than half of the fractures in pelvic bones are caused by motor-vehicle crashes [12]. Previous studies have simulated the human pelvis and lower limbs to investigate the injury mechanisms in different types of crashes [14, 19, 118-125]. Kikuchi et al. [118], modeled a human pelvis and lower limb to predict the injuries during the frontal motor-vehicle impact. For simulation of knee-thigh-hip (KTH) complex injuries in frontal motor vehicle crashes, the FE models were developed and bone deformation, articulating joints and soft tissue behavior in the KTH complex were analyzed by Van Rooij et al. [119]. Also, Silvestri et al. [121] developed an FE model of KTH with ligaments and muscles to explore the mechanics of injuries of the KTH during frontal crashes. Ikeda et al. [120] used FE models to predict the different fracture patterns of pelvic ring in pedestrian accidents with SUV/ Mini-Vans. The models developed by Ikeda et al. [120] were capable of accurately predicting different patterns of pelvic fractures and their study was the only one found to predict the fracture location in the pelvic ring in frontal car crashes.

In other previous studies, the fractures and injury mechanisms of pelvic bones in falls were modeled and investigated [3, 12, 20, 28-30, 126-133]. Many of these papers studied pelvic injury mechanisms in backward falls, sideways falls and lateral pelvic impacts using FE models [12, 20, 28-30, 126-131]. Kim et al. [130] investigated the effects of childhood obesity on pelvic bone fracture risk exposed to falls. Song et al. [131] developed FE models of the vertebrae and the pelvis to analyze the dynamic mechanisms of these bones in human falls. The majority of the studies discussed here concentrated on the damage of the pubic symphysis and

sacroiliac joints, while the fracture modeling of the bone was not considered as part of the simulation [12, 20, 28-30, 126-131]. Besnault et al. [133] introduced a material model to simulate damage and injury in the human pelvis ring. To the best of our knowledge, only one study has modeled the crack initiation on the pelvic bone [3]. However, instead of a real bone, a synthetic polyurethane pelvis was utilized to model the fracture [3].

The objective of the current study was to predict the types of fracture and model fracture initiation and propagation in pelvic bones under various loading conditions. The objectives were achieved through the following specific aims: extended finite element method (XFEM) models of pelvic bone were developed in which precise material properties and fracture characteristics of cancellous and cortical tissues were considered as model inputs. Various loading conditions were applied to the acetabulum in order to model the different types of fractures in pelvic bone. The outputs of this approach contain maximum force at fracture point; also, the types of fracture have been compared to the previously published experimental tests of pelvic bone fracture.

5.3 Methods

5.3.1 Fracture in cortical and cancellous tissues in macro-scale level

In previous studies, fracture of cancellous and cortical tissues on a macro-scale level have been modeled by the XFEM technique [40, 191]. The material properties and failure parameters of cancellous bone are mentioned in Table 5.1 [191]. In the previous work by our group [191], the "Max Principal strain" criterion was utilized as the damage initiation criteria. In ABAQUS built-in models of crack initiation criteria, a compressive strain does not initiate damage in an enriched element [59]. Salem et al. [191] implemented a user-defined subroutine UDMGINI to define crack initiation criteria by simultaneous tensile and compressive strain. This allows us to also use different strains in tension and in compression for failure.

Table 5.1. Material properties and failure parameters of cancellous tissue [191]

Damage Evolution (XFEM) parameters	Tension		Compression	
	Max principal strain	Fracture Energy (mJ/mm^2)	Max principal strain	Fracture Energy (mJ/mm^2)
	0.068	1	0.166	1
Elastic	Young's modulus (MPa)		Poisson's ratio	
	370		0.18	
Cast iron plasticity parameters	Tension		Compression	
	Yield Stress (MPa)	Ultimate stress (MPa)	Yield Strain	Ultimate Plastic Strain
	12.14	16.04	0.0345	0.0335

Compression			
Yield Stress (MPa)	Ultimate stress (MPa)	Yield Strain	Ultimate Plastic Strain
11.3	17.3	0.033	0.133

Moreover, in the previous work by Feerick et al. [40] a user-defined subroutine UDMGINI has been implemented for the cortical bone to utilize four failure criterion equations which are indicated in Equations 5.1-5.4. Once the value of any equation reaches 1, fracture is initiated for that criterion. Failure in the X, Y and Z directions are determined by Equations 5.1-5.3, respectively [40]. In Equation 5.4, when the maximum principle stress reaches the effective strength, the fracture initiates and propagates in the normal direction of the maximum principal direction [40]. The failure criteria in the X and Y directions (Equations 5.1 & 5.2 respectively) have been defined in tension and compression; hence, six failure parameters are indicated in Table 5.2 [40].

$$Failure\ criterion\ 1: \sqrt{(\frac{\sigma_{11}}{\sigma_{lx}})^2 + (\frac{\sigma_{12}}{\sigma_{lx\tau}})^2 + (\frac{\sigma_{13}}{\sigma_{lx\tau}})^2} = 1 \tag{5.1}$$

$$Failure\ criterion\ 2: \sqrt{(\frac{\sigma_{22}}{\sigma_{ly}})^2 + (\frac{\sigma_{12}}{\sigma_{ly\tau}})^2 + (\frac{\sigma_{23}}{\sigma_{ly\tau}})^2} = 1 \tag{5.2}$$

$$Failure\ criterion\ 3: \sqrt{(\frac{\sigma_{33}}{\sigma_{lz}})^2 + (\frac{\sigma_{13}}{\sigma_{lz\tau}})^2 + (\frac{\sigma_{23}}{\sigma_{lz\tau}})^2} = 1 \tag{5.3}$$

$$Failure\ criterion\ 4: \frac{\sigma_p}{\sqrt{{\sigma_{lx}}^2 cos^2\theta + {\sigma_{ly}}^2 sin^2\theta}} = 1 \tag{5.4}$$

Where σ_{lx} and $\sigma_{lx\tau}$ are the axial and shear strengths in X direction, respectively; σ_{ly} and $\sigma_{ly\tau}$ are the axial and shear strengths in Y direction, respectively; and σ_{lz} and $\sigma_{lz\tau}$ are the axial and shear strengths in Z direction, respectively. σ_p is the maximum principal stress; $\sigma_{11}, \sigma_{22}\ and\ \sigma_{33}$ are orthogonal normal stresses; and $\sigma_{12}, \sigma_{23}\ and\ \sigma_{13}$ are orthogonal shear stresses [40].

Table 5.2. Elasticity, strengths and damage evolution parameters of cortical bone [40]

Mechanical properties		initiation criteria failure strengths (MPa)	
Young's modulus (MPa)	4500	σ_{lx}(tensile)	150
Poisson's ratio	0.3	$\sigma_{ly} = \sigma_{lz}$(tensile)	65
		σ_{lx}(Compression)	280
Evolution criteria (J/m^2)		$\sigma_{ly} = \sigma_{lz}$(Compression)	213
Failure criteria 1	800	$\sigma_{lx\tau}$	84
All other failure criteria	300	$\sigma_{ly\tau} = \sigma_{lz\tau}$	132

5.3.2 3D XFEM modeling of pelvic bone

The XFEM framework built-into the general purpose finite element analysis software ABAQUS/Standard (Dassault Systemes Simulia Corp, Providence, RI, USA) was utilized to develop the 3D model [59]. CT-scan data of an intact pelvic bone (left hemi-pelvis) was utilized and converted to the 3D mesh part by Materialise Mimics software (Materialise NV, Leuven, Belgium). The cortical and cancellous tissues were specified from CT-scan data in the mesh part. The created mesh part in Materialise Mimics software with the specified cancellous and cortical tissues is illustrated in Fig.5.1. The mesh part was imported to the Abaqus software as an input file. The re-implemented fracture modeling of cancellous and cortical bones from the previous section were assigned to the pelvic bone.

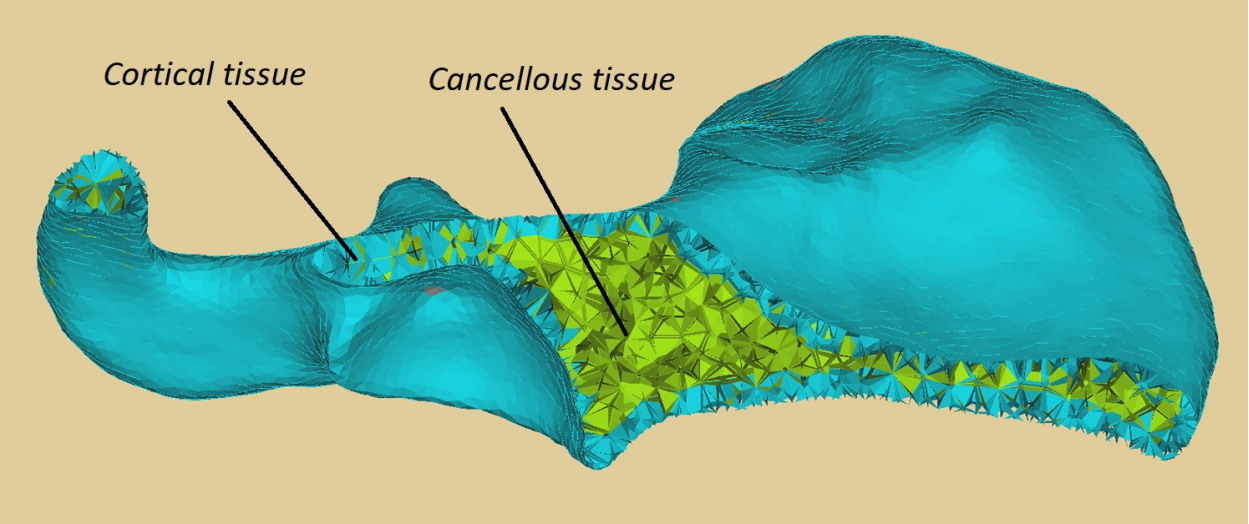

Figure 5.1. Intact pelvic bone with specified cortical and cancellous tissues

C3D4 (4-node linear tetrahedron) elements were selected in all simulations [59]. To develop a realistic model, several enrichment zones were defined for the pelvic bone to allow for simultaneous initiation and propagation of multiple cracks. Selecting elements in such a complex geometry like the pelvic bone is time-consuming. In order to do so, all elements of the bone were selected as one element set and the input file of the model was written. Afterward, the input file was edited, and the element set was split into several element sets with an almost equal numbers of elements. Each element set was then defined as one enrichment zone.

The hemi-pelvis is supported by two locations in human body skeleton: sacro-iliac and pubis symphasis joints [192]. The sacro-iliac joint has strong ligaments and interlocking surfaces, thus, its movement is negligible [192]. Also, a sensitivity study was conducted on boundary conditions at pubis symphysis joint and the results revealed negligible differences on the outputs [192]. In the current paper, the pelvic bone was fixed at the sacro-iliac and pubis symphasis joints by fully constraining these nodes in all simulations [192]. The loading on pelvis was specified as a constant velocity (1 m/s) applied to the nodes of acetabulum as illustrated in Fig.5.2(a) [193, 194]. This makes the assumption of quasi static loading. The direction of the applied velocity was varied to model the different types of fracture (e.g., anterior/posterior wall fracture and transverse fracture). The local coordinate system was set up as shown in Fig.5.2(b) to apply the loads in main groups of shear, compression, and their combination [195]. The velocity in Y and Z directions represent shear loads on acetabulum, and the velocity in X direction represents a compressive load. Furthermore, combined directional

loading (i.e. loading in both the X and Y directions simultaneously) was also investigated. Totally 11 simulations have been run that the loading direction in each simulation is indicated in Table 5.3. The load-displacement graph of the pelvic bone was extracted for each simulation. The loads were calculated by summing nodal reaction forces on the fully constrained areas of pelvic bones. The simulations were terminated at the point where the load dropped in load-displacement graph or when the time-increment became too small for the simulation to continue. In the latter cases, the crack initiation was captured, but the models did not fully fracture. The output variables of interest were the location and pattern of fracture initiation and the maximum fracture force.

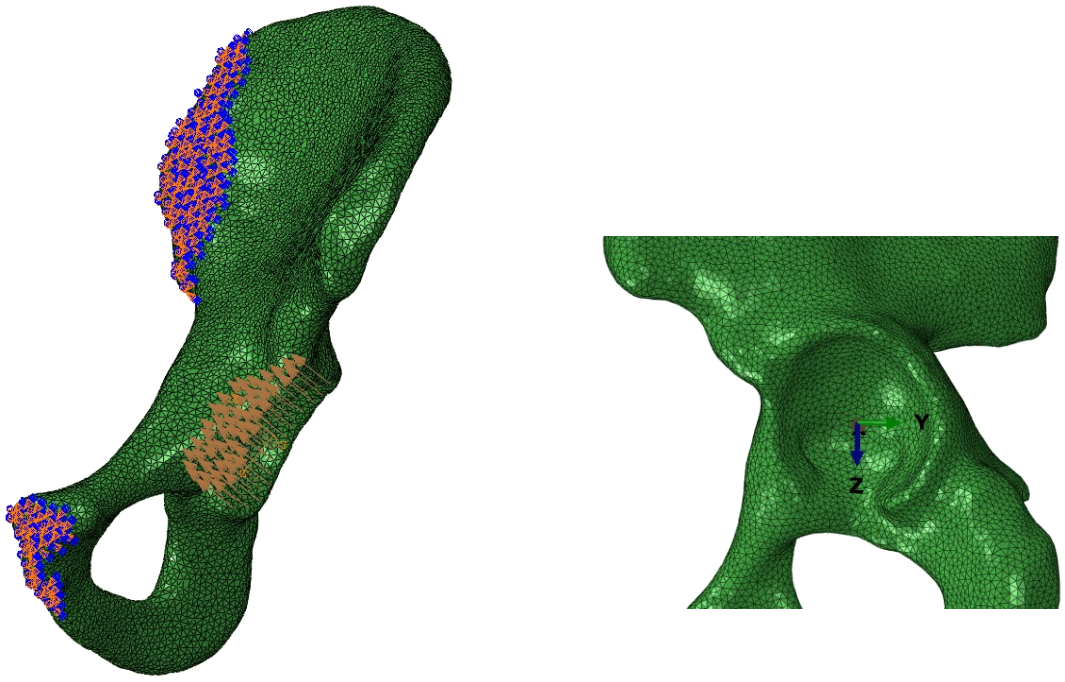

(a) **(b)**

Figure 5.2. (a) Applied boundary and loading conditions to the pelvic bone; (b) defined local coordinate system

Table 5.3. Loading direction in each simulation

Run NO.	1	2	3	4	5	6	7	8	9	10	11
Loading direction	+Z	-Z	+Y	-Y	+X	+X,+Z	+X,-Z	+X,+Y	+X,-Y	+Z,+Y	+Z,-Y

5.4 Results

Different types of fractures were obtained from the modeling in various loading conditions, as shown in Fig.5.3(a)-(k). The direction of applied velocity in each simulation is illustrated in Fig.5.3. The STATUSXFEM in Fig.5.3 shows the status of the enriched elements. The value of 1.0 for STATUSXFEM means the enriched element is completely cracked and 0.0 means that the element contains no crack. The value of STATUSXFEM lies between 1.0 and 0.0 if the element is partially cracked. Further, the load-displacement graphs of pelvic bone were extracted and illustrated in Fig.5.4(a). To fully fracture the pelvic bone model would require large computational resources, which was impractical in this study. As it can be seen in Fig.5.4, only three of simulations reach to the fracture drop point in the load-displacement graphs. In the rest of the simulations, the time increment became too small (in order of 10^{-35}) and the simulation run was aborted by the software before reaching to the drop point in the load-displacement graph. The maximum fracture force among all simulations was computed to be 18.6kN with the velocity applied in the +Z and +Y directions. As it can be observed in Fig.5.3(a)-(k), the anterior/posterior wall fracture and transverse fracture are the most common types of fractures in the simulations. There are 6 anterior/posterior wall fractures and 6 transverse fractures from the outputs of simulations.

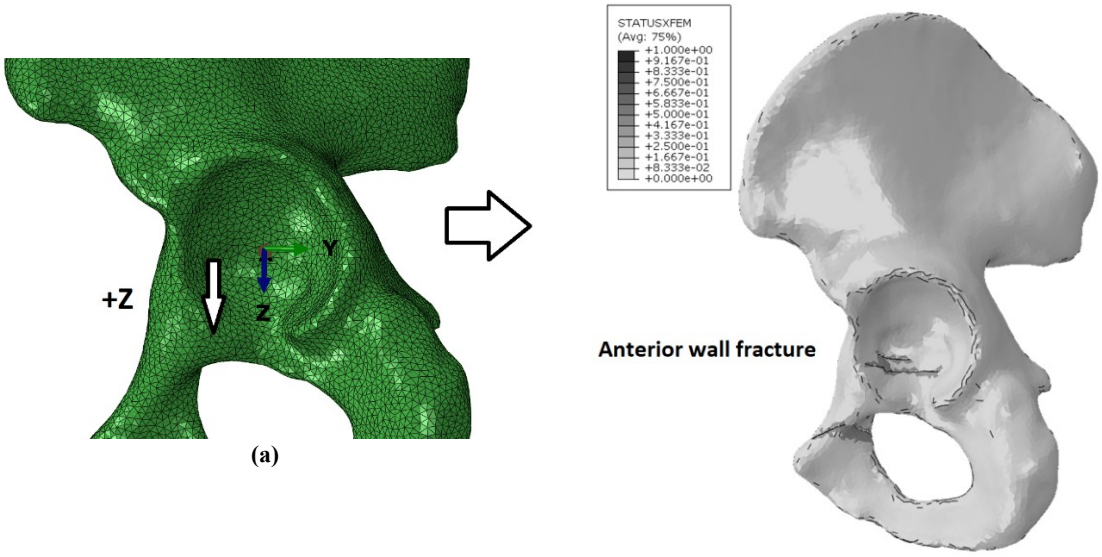

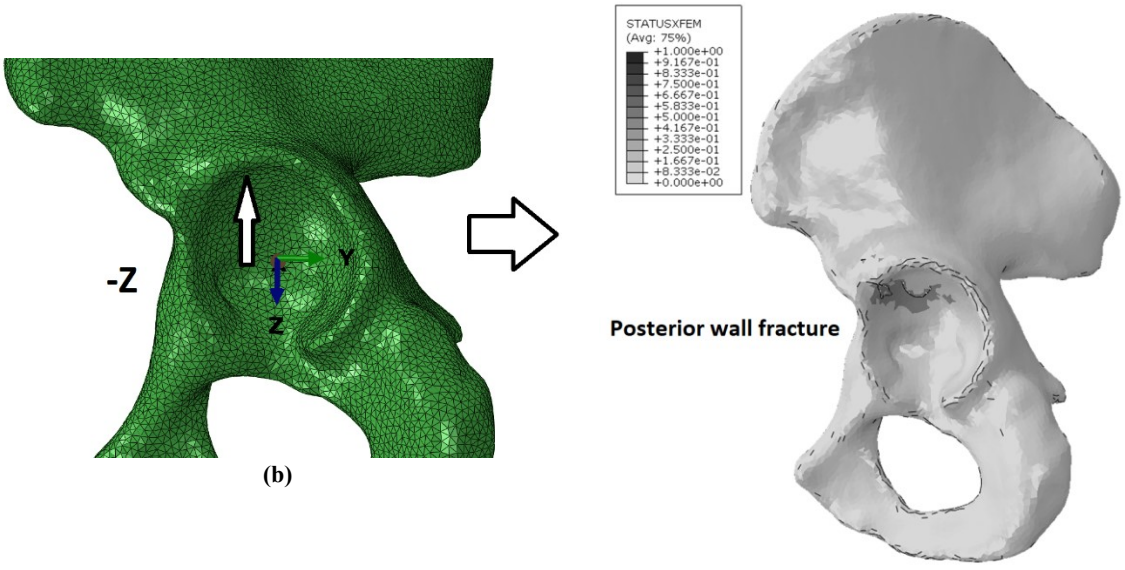
-Z
Y
Z
STATUSXFEM
(Avg: 75%)
+1.000e+00
+9.167e-01
+8.333e-01
+7.500e-01
+6.667e-01
+5.833e-01
+5.000e-01
+4.167e-01
+3.333e-01
+2.500e-01
+1.667e-01
+8.333e-02
+0.000e+00
Posterior wall fracture

(b)

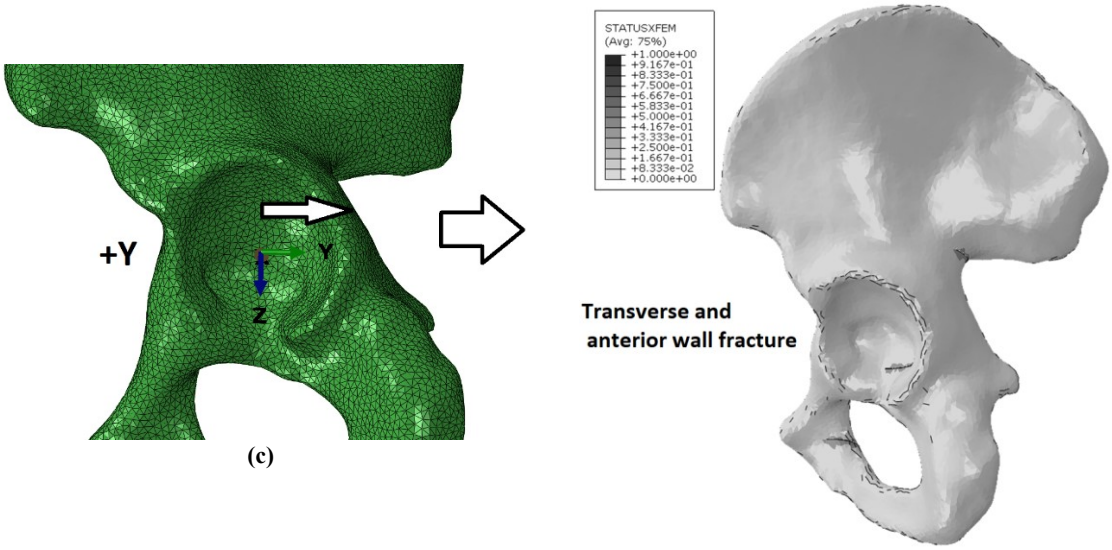
+Y
Y
Z
STATUSXFEM
(Avg: 75%)
+1.000e+00
+9.167e-01
+8.333e-01
+7.500e-01
+6.667e-01
+5.833e-01
+5.000e-01
+4.167e-01
+3.333e-01
+2.500e-01
+1.667e-01
+8.333e-02
+0.000e+00
Transverse and
anterior wall fracture

(c)

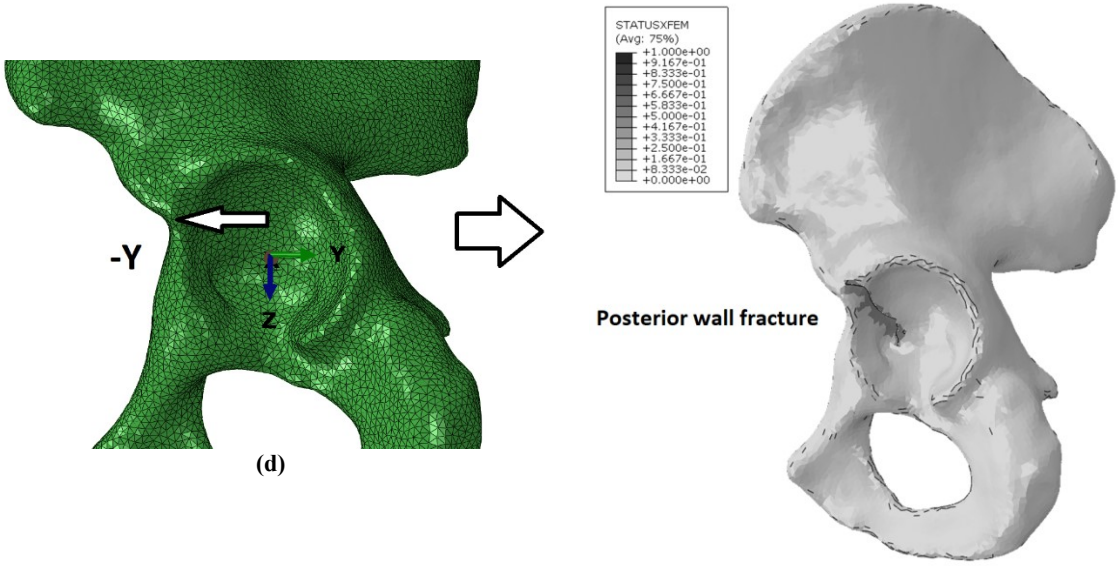
-Y
Y
Z
STATUSXFEM
(Avg: 75%)
+1.000e+00
+9.167e-01
+8.333e-01
+7.500e-01
+6.667e-01
+5.833e-01
+5.000e-01
+4.167e-01
+3.333e-01
+2.500e-01
+1.667e-01
+8.333e-02
+0.000e+00
Posterior wall fracture

(d)

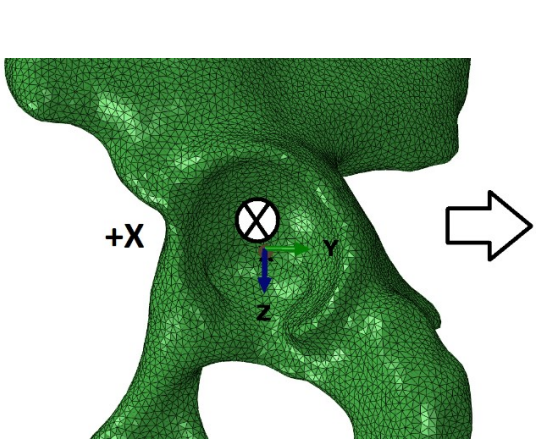
+X
Y
Z

(e)

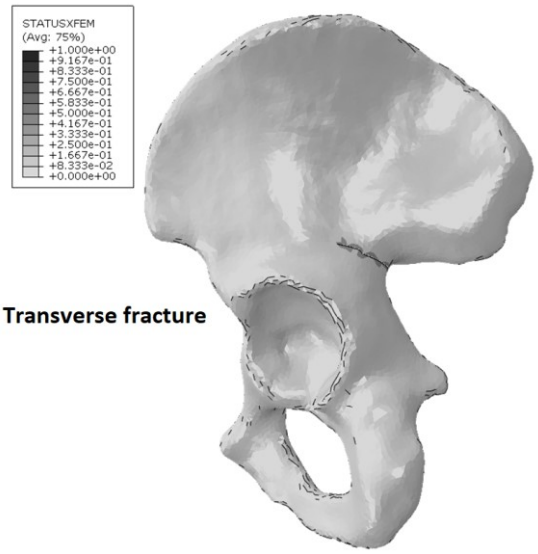
STATUSXFEM
(Avg: 75%)
+1.000e+00
+9.167e-01
+8.333e-01
+7.500e-01
+6.667e-01
+5.833e-01
+5.000e-01
+4.167e-01
+3.333e-01
+2.500e-01
+1.667e-01
+8.333e-02
+0.000e+00
Transverse fracture

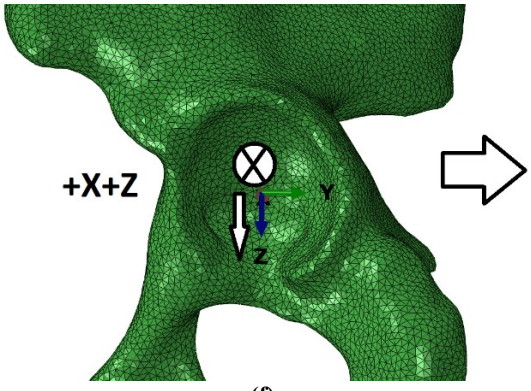
+X+Z
Y
Z

(f)

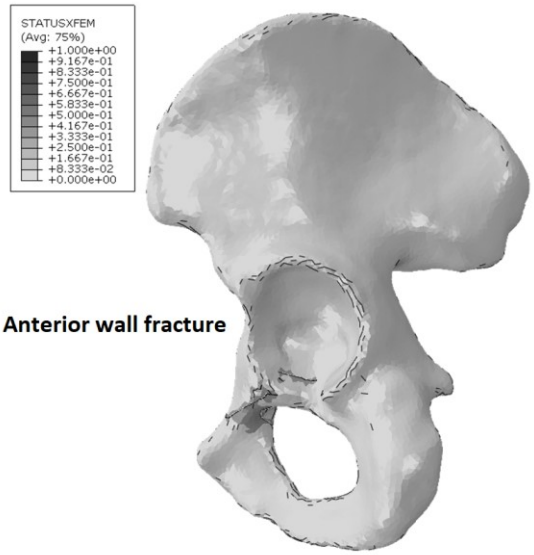
STATUSXFEM
(Avg: 75%)
+1.000e+00
+9.167e-01
+8.333e-01
+7.500e-01
+6.667e-01
+5.833e-01
+5.000e-01
+4.167e-01
+3.333e-01
+2.500e-01
+1.667e-01
+8.333e-02
+0.000e+00
Anterior wall fracture

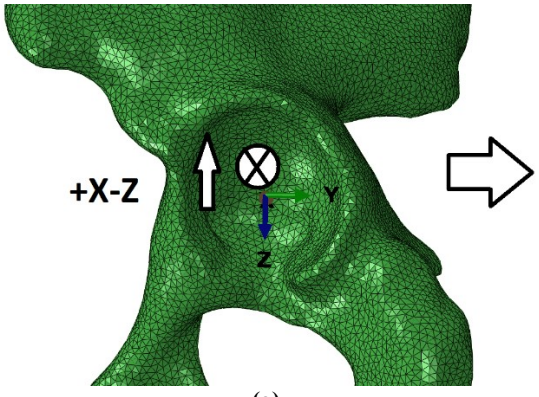
+X-Z
Y
Z

(g)

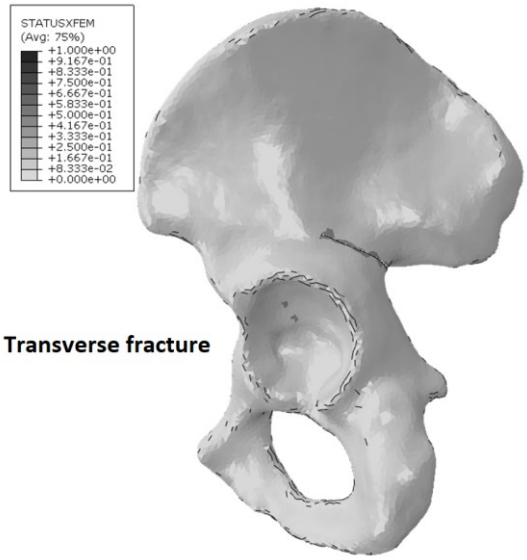
STATUSXFEM
(Avg: 75%)
+1.000e+00
+9.167e-01
+8.333e-01
+7.500e-01
+6.667e-01
+5.833e-01
+5.000e-01
+4.167e-01
+3.333e-01
+2.500e-01
+1.667e-01
+8.333e-02
+0.000e+00
Transverse fracture

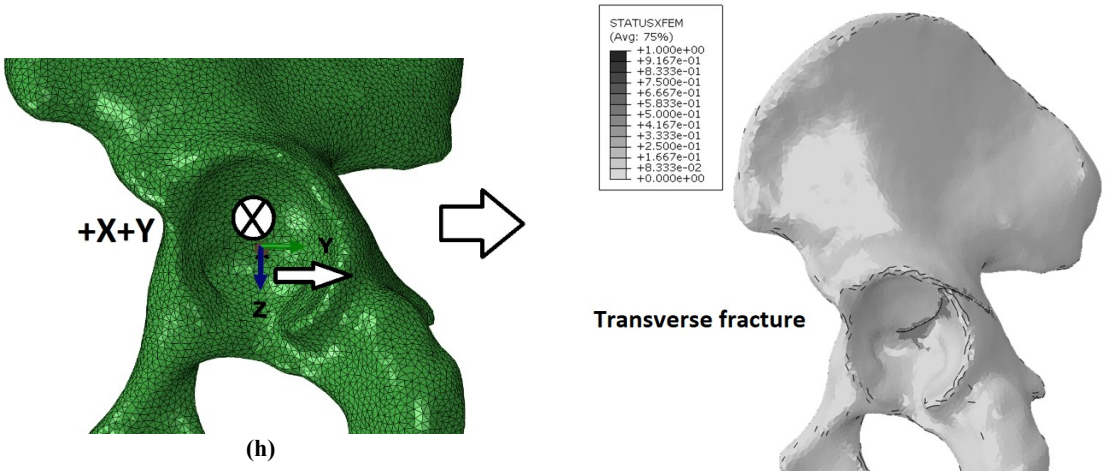
+X+Y
Y
Z
STATUSXFEM
(Avg: 75%)
+1.000e+00
+9.167e-01
+8.333e-01
+7.500e-01
+6.667e-01
+5.833e-01
+5.000e-01
+4.167e-01
+3.333e-01
+2.500e-01
+1.667e-01
+8.333e-02
+0.000e+00
Transverse fracture

(h)

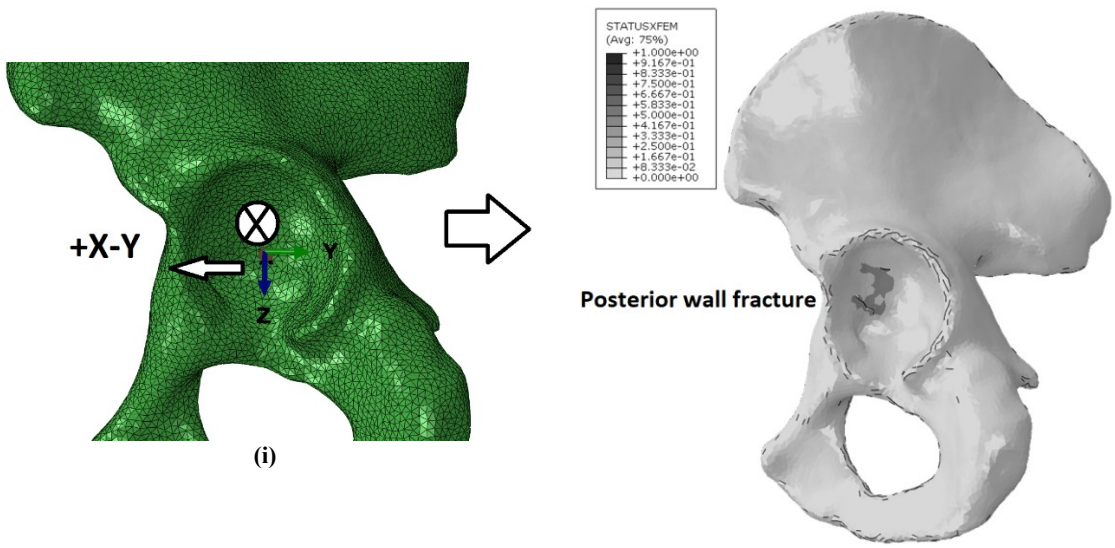
+X-Y
Y
Z
STATUSXFEM
(Avg: 75%)
+1.000e+00
+9.167e-01
+8.333e-01
+7.500e-01
+6.667e-01
+5.833e-01
+5.000e-01
+4.167e-01
+3.333e-01
+2.500e-01
+1.667e-01
+8.333e-02
+0.000e+00
Posterior wall fracture

(i)

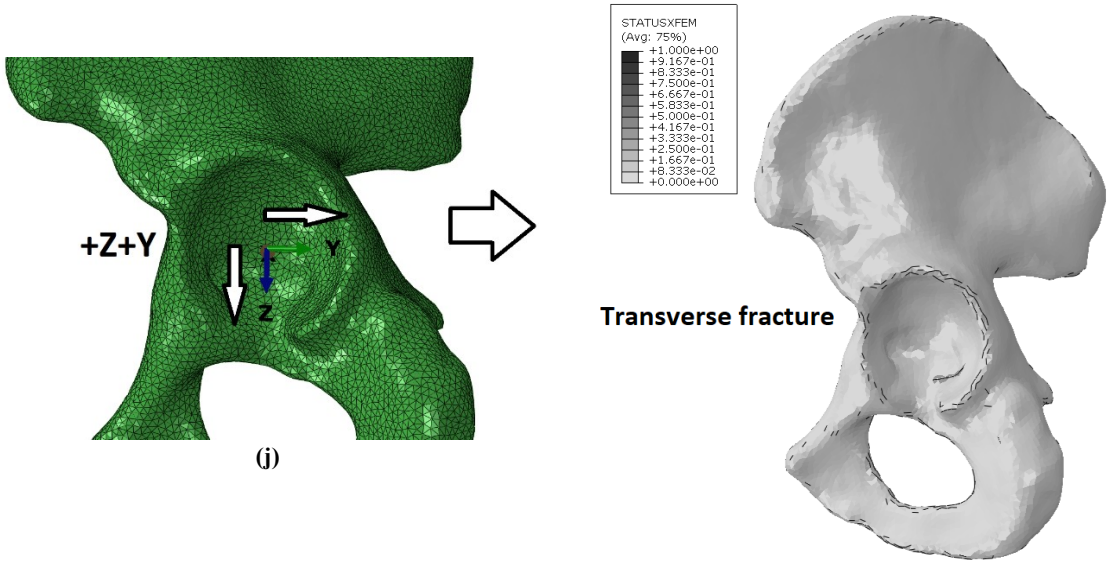
+Z+Y
Y
Z
STATUSXFEM
(Avg: 75%)
+1.000e+00
+9.167e-01
+8.333e-01
+7.500e-01
+6.667e-01
+5.833e-01
+5.000e-01
+4.167e-01
+3.333e-01
+2.500e-01
+1.667e-01
+8.333e-02
+0.000e+00
Transverse fracture

(j)

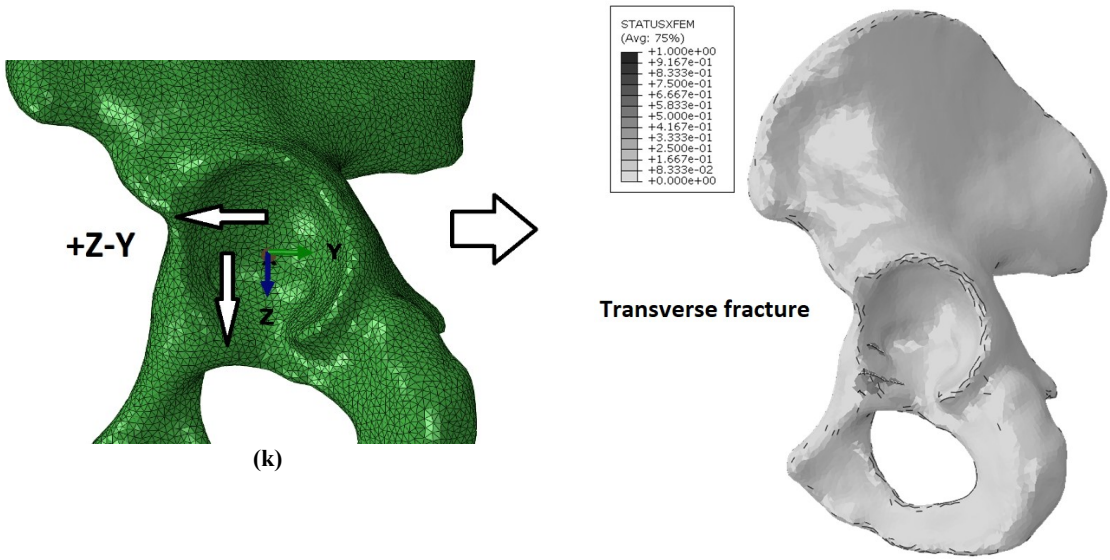

Figure 5.3. Different types of fractures from various loading conditions modeled by XFEM (a) anterior wall (b) posterior wall (c) transverse & anterior wall (d) posterior wall (e) transverse fracture (f) anterior wall (g) transverse fracture (h) transverse fracture (i) posterior wall (j) transverse fracture (k) transverse fracture

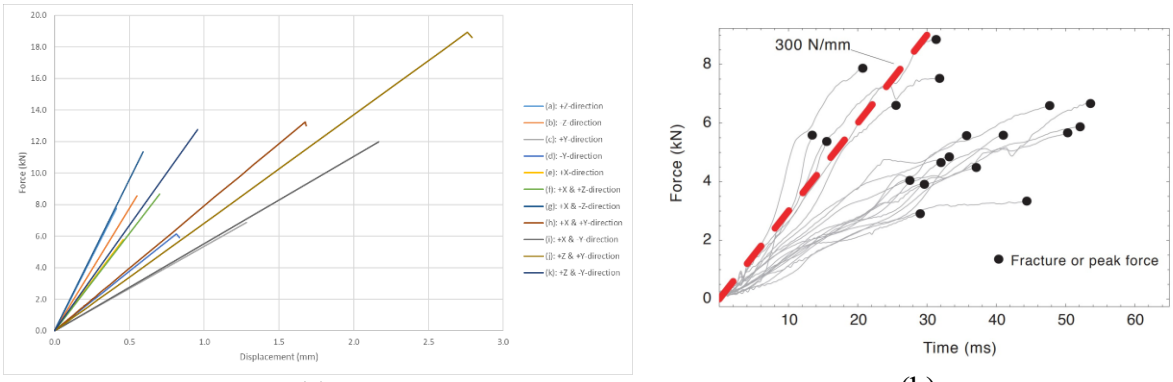

(a) (b)

Figure 5.4. (a) Load-displacement graphs of fractured pelvic bone obtained from XFEM simulations (b) Force-time graphs reported from experiments [194]

5.5 Discussion

In recent years, car manufacturers are providing and improving the protection of occupants' KTH complex in frontal and lateral impacts [129, 193, 194]. Also, various types of hip protector have been designed for elderly people to prevent hip and pelvic bone fractures which are investigated in several previous studies [196-198]. Recently, the XFEM technique has been considered a valuable analytical method to predict fractures in the KTH complex instead of relying on experimental test setups. As a result, the main aim of this study was to predict the

types of fracture and model fracture initiation and propagation in pelvic bones under various loading conditions.

In this study, 3D XFEM models of a hemi-pelvis were developed. The mechanical behaviors and failure parameters of cancellous and cortical tissues were re-implemented from previously published studies [40, 191] and were applied to the intact pelvic bone with specified tissue regions defined by CT-scan data. Boundary and loading conditions were specified in the models as well as the enrichment zones, which allow XFEM to initiate and propagate the multi-cracks anywhere within these regions. Various loading conditions were applied to the acetabulum nodes as a constant velocity (1 m/s) in various directions to model different types of fracture in the bone. The fracture type, the load-displacement curves, and the maximum force at the fracture point were extracted and shown in Figs.5.3 and 5.4.

Rupp et al. investigated the fracture in the KTH complex in several experimental studies [193, 194, 199-201] to develop a new KTH failure criteria in frontal motor-vehicle impacts. They used a device to measure the hip fracture force with human cadavers. In Table 5.4, the results of 19 experimental tests containing the fracture type in the pelvic bone and maximum force at fracture point are mentioned. Also, the types of fracture obtained from XFEM models and reported in Table 5.4, are shown in Fig.5.5.

Table 5.4. Type of fracture in pelvic bones and maximum force at fracture point from experimental tests [193, 194]

Test Number	Force at fracture (kN)	Fracture type
1	5.59	Acetabulum (“T-type fracture”), inferior ramus
2	5.37	Acetabulum (transverse, posterior wall)
3	4.85	Acetabulum (posterior wall)
4	4.49	No injury
5	7.52	Femoral neck
6	7.87	Femoral neck
7	6.60	Acetabulum (posterior wall), pubic rami
8	6.67	Acetabulum (posterior coloumn, anterior hemi-transverse fx.) pubic rami
9	3.34	Iliac wing, pubic rami

10	4.65	Femoral neck
11	5.59	Acetabulum (posterior wall/column), inferior pubic ramus
12	4.79	Acetabulum (transverse posterior wall), inferior pubic ramus
13	5.57	Acetabulum (posterior wall)
14	4.04	Acetabulum (posterior wall/ column)
15	8.85	Acetabulum (posterior rim)
16	3.91	Acetabulum (transverse posterior wall), pubic rami
17	5.67	Acetabulum ("T-type" with comminuted posterior wall)
18	5.87	Acetabulum (posterior rim)
19	6.6	Acetabulum (posterior wall, anterior/superior rim)
Mean	5.70	
SD	1.38	

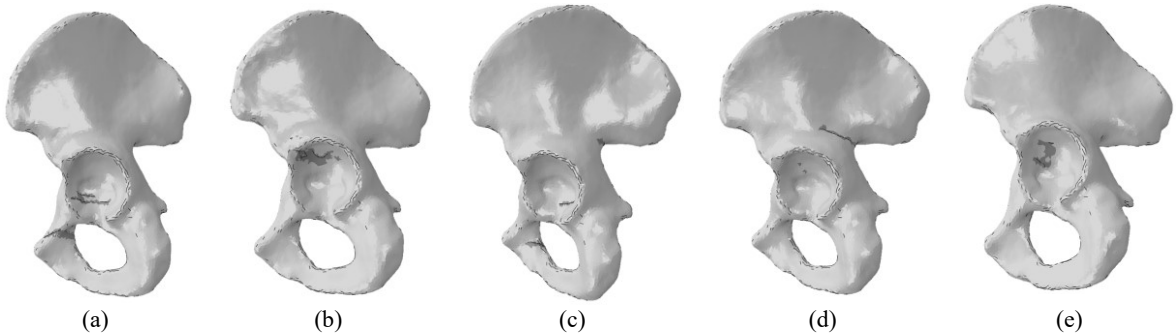

Figure 5.5. The types of fracture obtained from XFEM models and reported in Table 5.4 (a) anterior wall fracture (b) posterior wall fracture (c) transverse and anterior wall fracture (d) transverse fracture and (e) posterior wall fracture [202]

As reported in [193, 194], all conditions in the experimental tests were similar. However, there are different types of fractures in pelvic bones. After an analysis of experimental outputs, it was revealed that the fracture types in the pelvic bones are dependent on several parameters such as the density of the pelvic bones, the impact intensity and impact direction from femur head to acetabulum in the unstable conditions of the impact loads [129]. As it indicated in Table 5.4, in 14 tests out of 19 experiments, the fracture occurred in acetabulum which contained two T-type fractures, seven posterior wall or column fractures, three transverse fractures and two posterior rim fractures [193, 194]. The maximum and the average fracture force were determined to be 8.85kN and 5.7 ± 1.38kN respectively [193, 194].

A comparison of obtained fracture types in the XFEM models in the present study with the experimental tests from Rupp et al. [193, 194] indicates that the impact direction from the femur head to acetabulum causes different types of fractures. However, it should be noted that the XFEM models in the present study did not run to the end of simulation in most cases and thus the cracks were not propagated through the whole bone. Nevertheless, the crack initiation seen with these models provides a good indication of the location and initial pattern of the fractures.

The maximum fracture force (18.6kN) obtained from XFEM models (Fig.5.4) was higher than the values reported in the previous experimental studies [193, 194] (8.85kN), but this discrepancy can be explained by several reasons. Firstly, mechanical characteristics of bone tissues are different based on the density of specimens and anatomical locations of the specimens [147, 157, 178-181]. One limitation is that the cortical and cancellous specimens of the studies referenced here [40, 191] were selected from the femur and forearm respectively and not the pelvic bone. With proper mechanical and failure behaviors of cortical and cancellous tissues (by the specimens extracted from human pelvic bones), the results of our XFEM model might have a better agreement with experimental results. Secondly, the experimental tests were conducted on KTH complex and the measured impact intensity on the pelvic bone in the tests might be affected by the knee and thigh. However, the impact intensity was considered to be consistent in all XFEM models. Thirdly, based on additional literature [83-85], the fully constrained boundary conditions utilized in XFEM models are extremely simplified. Considering more realistic boundary conditions (using muscular and ligament attachments) might help to improve the FE results compared to the experimental results.

Early car designers and researchers focused on head, neck and chest injuries because of the importance of these areas as most life-threatening regions of human body in the frontal car crashes [203]. Using seatbelts and implementation of airbags highly reduced the head and thorax injuries in the car accidents [203]. Design improvement of the cars for more appropriate protection of lower extremities to prevent various types of pelvic bone fracture is a particular concern of automotive safety engineers [203]. The results of the current study revealed that different types of fracture in the pelvic bones can be caused by the various loading conditions in unstable conditions of high-rate impact loads. With proper mechanical and failure behaviors

of cortical and cancellous tissues, the XFEM model of the pelvic bone is capable of predicting the fracture initiation and propagation in the bone. In future work, the XFEM model of cancellous and cortical tissues can be assigned to other bones in human body so that the failure mechanism in such bones can be investigated.

Currently, modeling the branching in a single element by XFEM technique is impractical due to the limitation of this technique [134]. Because of this limitation, not all fracture types in pelvic bone can be represented with an XFEM model.

Chapter 6 : Optimization of fixation plates for T-shaped pelvic bone fractures

6.1 Abstract

Objective: To evaluate and optimize the mechanical stability and stress shielding of the fixation system in T-shaped acetabular fracture by conjunction of Finite Element Analysis (FEA) and Design of Experiment (DoE).

Method: FE models of (1) an intact pelvic bone and (2) a T-style fractured pelvic bone fixed by a reconstruction plate and screws were developed. Three design factors including plate thickness, plate material and the number of screws were studied to determine their influences on biomechanical responses of fixation system. For the statistical analysis, a fractional factorial design was considered. Ten FE models based on the matrix of levels definition have been developed. An analysis of variance (ANOVA) technique was employed to define the significant variables related to biomechanical responses and finally the optimized design factors were determined.

Results: It was observed that plate material and its thickness are the main effective variables (with $p<0.05$) on most of investigated biomechanical responses of fixation system. The results revealed that reducing 62.5% of the stiffness of the plate material resulted in a 24.1% decrease of the stability of the fixed bone and 10.8% decrease of the average of stress shielding rate. Also, reducing 22.2% of the plate thickness from 4.5mm to 3.5mm caused a decrease of 8.6% in the mechanical stability and an 8.1% decrease in the average stress shielding rate. Reducing the number of screws from 11 to 7 screws had no effect on the average of crack opening and stress shielding rate.

Conclusion: The results revealed that the plate material and its thickness are the most effective parameters in the design of optimal fixation plates. Also, increasing the number of screws has no significant effect on most of the responses that can be considered by the surgeons in pelvic

fracture fixation. Finally, combination of DoE and FEA is capable to reduce the number of FE models and runs without sacrificing the required results accuracy.

6.2 Introduction

Pelvic bone has a significant role in human body skeleton because of its duties to linking the upper body to the lower extremities, weight bearing, transferring the weight to the lower limbs and protecting the inner organs of that area [1, 2, 8].

Damage and fracture of the pelvic bone or acetabulum is a common type of fracture especially in motor-vehicle crashes [6]. One type of pelvic bone fracture is called T-shaped or T-style fracture. This type of fracture is a combination of a transverse fracture and a vertical fracture in the acetabulum [204]. T-shaped acetabular fracture represents 3%-12% of all types of pelvic bone fractures [204] and 7% of pelvic fractures with two or more fractures within the acetabulum [5]. Since, T-shaped fracture classifies as one of the complicated fractures of pelvic bones [5], this type of fracture was considered to be investigated in current research.

The fixation of T-shaped fractures is explained in the book by Tile et al. [5] which is a reference for the surgeons working on pelvic bones. Also, there are numerous studies [76-82] that have been dedicated to evaluating the functional outcomes of operative treatment of such injuries. However, to the best of our knowledge, there is only one study [4] that has investigated the fixation system of T-shaped fracture in the pelvic bone by FE analysis. Fan et al. [4] evaluated three different fixation systems of T-shaped fracture by FE analysis and obtained the optimized fixation system for treatment of the injured bone.

The geometrical configuration and material selection for reconstruction plates and lag screws play a significant role in generating the biomechanical performances such as reliable internal fixation, and in the reduction of stress shielding and implant loosening [31-36, 152, 205]. Screw configurations such as the number of screws, their placement in the locking plates, and the length and diameter of screws have previously been investigated [34]. The shape, thickness, and width of the locking plates have been optimized for different applications [32, 33]. The optimal material selection and implant design, such as using porous structures in the implants,

have been investigated previously for reduction of stress shielding and acceleration of fracture healing [31, 152]. In the study by Mehboob and Change [35] a combination of Design of Experiments (DoE), Finite Element Analysis (FEA) and the Taguchi method was utilized to design and optimize a composite fixation plate for a damaged tibia. Further, other studies investigated and optimized the fixation plate-screws parameters using a combination of DoE and FE analysis [31-36]. In the previous work [31-36], the optimization of fixation plate-screws was related to various bones in human body skeleton aside from the pelvic bone. To the best of our knowledge, there is no study to optimize the characteristics of fixation plates related to a damaged pelvic bone.

The objective of the current study was to evaluate and optimize of mechanical stability and stress shielding of a fixation system in a T-shaped acetabular fracture by conjunction of FEA and DoE. The objectives were achieved through the following specific aims: The FE model of an intact pelvic bone (right hemi-pelvis) and a T-shaped damaged bone fixed by a plate and screws were developed. Several design factors were considered to evaluate their effects on biomechanical responses of fixation system. The statistical analysis has been conducted on the outputs of FE models and the main significant factors have been determined. Finally, the optimized design factors were obtained.

6.3 Methods

6.3.1 FE model of T-Shaped fracture bone and an intact bone

Two FE models of a right hemi-pelvis were developed in this study. The first considered an intact pelvic bone and the second modeled simulated a T-shaped fractured bone fixed by a reconstruction plate and screws. (the fracture model is shown in Fig.6.1). The FE model of intact pelvic bone was developed as a reference to compare with the outputs obtained from the fixed bone model with the plate and screws. i.e. the stresses obtained from fixed pelvic bone model ideally should have almost the same values computed from the intact pelvic bone model.

Cortical and cancellous tissue material properties were considered in both models, and the thickness of the cortical layer was assumed to be constant at 2.5mm [25]. The cortical and

cancellous bones were modeled as solid parts. The plate in the T-shaped fracture model was modeled as a shell part. The screws were generated as solid parts, neglecting the screws heads. The effect of the screw heads was considered in an interaction definition between the plate and cortical bone.

The mechanical characteristics of the bone tissues, plate with different materials, and screws are indicated in Table 6.1. The number of screws, the thickness of plate and the plate material were changed in further simulations related to the DoE model. The material of screws was selected to be 316L stainless steel in all simulations and various lengths of screws were considered to simulate bicortical fixations. Tie constraints was utilized at the tissue interface to ensure that no relative displacement occurs between the inner surface of cortical bone and outer surface of cancellous bone. Also, tie constraint were defined between the plate and the cortical bone surface (in the areas of the screw heads) and at the screw and bones tissues interface [4, 7, 51, 206]. There is no defined contact or constraint between the screws and the plate. Rough contact was defined between the pieces of fractured bone to allow interactions to occur between the pieces at their interfaces. A static/general step in ABAQUS/Standard (Dassault Systemes Simulia Corp, Providence, RI, USA) was utilized as the solver. C3D4 (A 4-node linear tetrahedron), C3D8R (An 8-node linear brick, reduced integration) and S4R (A 4-node shell, reduced integration) elements were selected for bone tissues, screws, and the fixation plate respectively. The loading and boundary conditions were defined to be the same in all simulations as shown in Fig.6.2. Both models were loaded under double limb standing position by a value of 600N, which represents the upper body weight.

Table 6.1. Mechanical characteristics of bone tissues, plate and screws

Material		**Young's modulus (MPa)**			**Poisson's ratio**	
Cancellous Bone [191]		370			0.18	
Cortical Bone [40]		4500			0.3	
Plate, Nitinol alloy (NiTi) [4]		105000			0.37	
Plate, SS 316 [51]		280000			0.33	
Screws, SS 316 [51]		280000			0.33	
Material	**E1 (MPa)**	**E2=E3 (MPa)**	**Nu12=Nu 13**	**Nu23**	**G12=G23 (MPa)**	**G13 (MPa)**
Plate, E-glass/epoxy [51]	15000	7000	0.25	0.3	6000	7000

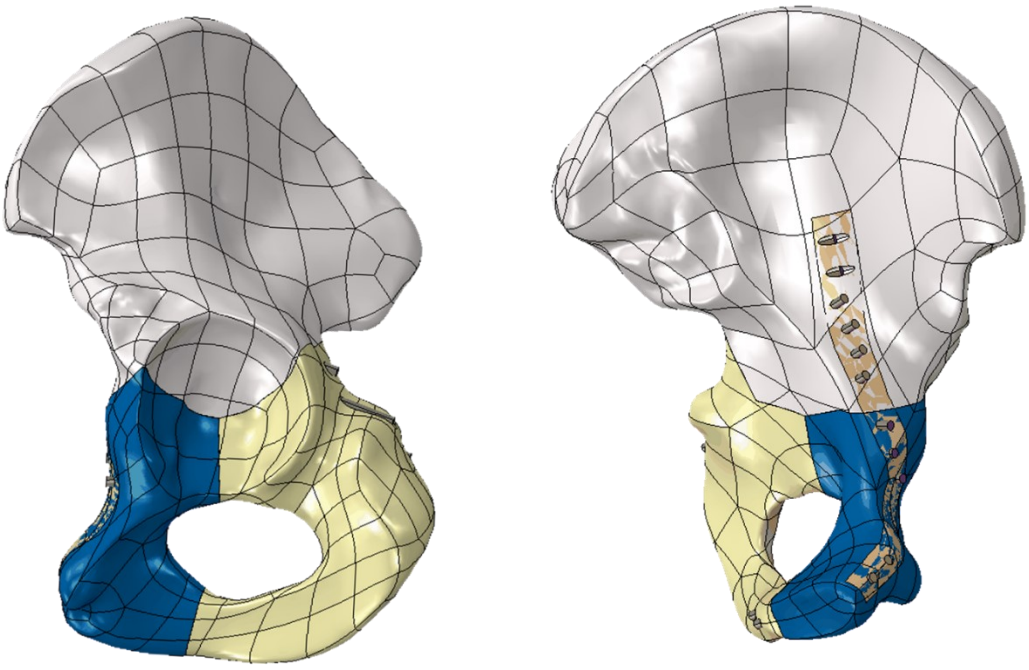

Figure 6.1. T-shaped fracture pelvic bone model fixed by reconstruction plate and screws

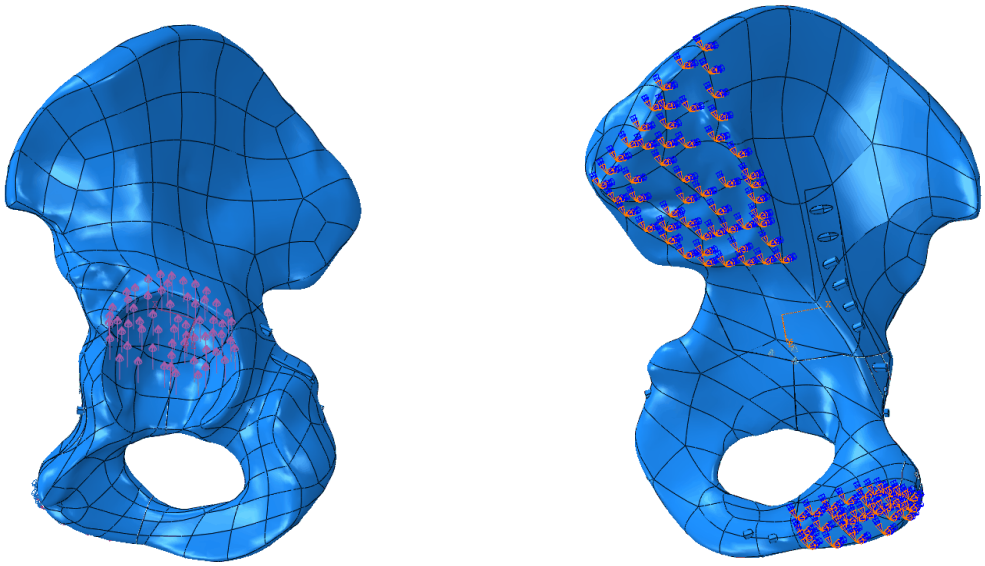

Figure 6.2. Loading and boundary conditions in the T-shaped fracture model

6.3.2 Design of experiments model

In this section, the developed FE model of T-shaped fractured bone fixed by a reconstruction plate and screws was utilized in statistical analysis to evaluate and optimize the design factors of fixation system. Three design factors including plate thickness, plate material, and the number of screws were selected from the literature [207-210] as the parameters of interest to optimize the mechanical stability and stress shielding of the fixation system in a damaged pelvic bone. Three levels were utilized for each of the design factors, which are determined based on the evaluated fixation systems reported in previous studies [4-7] to treat the T-shaped fracture bone and other types of fractures in pelvic bones. Table 6.2 shows the design factors and their dimensions at each level.

For the statistical analysis, a $3^{(3-1)}$ fractional factorial design was considered, and the matrix of corresponding levels and the number of runs has been designed and created by STATISTICA 12 software (StatSoft Inc., Tulsa, OK, USA). (the matrix is listed in Table 6.3). Fractional factorial methods have been recommended for biomechanical analysis yielding similar answers with less computational effort [153]. Nine FE models were developed by modification of FE model of fixed pelvic bone from previous section and corresponding to the features, listed in Table 6.3. Also, the outputs of the first developed FE model of the fixed pelvic bone from previous section (in total 10 FE models) has been utilized to be analyzed for optimization of the fixation system.

Biomechanical responses including crack opening, stress shielding rate, bone displacement, and maximum stresses in the bone, plate and screws were selected to evaluate the mechanical stability and stress shielding of the fixation system. The stress shielding rate was computed based on Equation 6.1 [211]. The rest of them were obtained from FE models directly.

$$Stress\ Shielding\ rate\ (\%) = \left(1 - {}^{\sigma}/_{\sigma_o}\right) \times 100 \tag{6.1}$$

Where σ and σ_o are the stresses computed from FE models for the treated bone and intact bone, respectively [211]. ANOVA technique in statistical analysis software (STATISTICA 12) has been employed to evaluate the output parameters and define the significant variables related to

the biomechanical response. Finally, the optimal value of each design factor was determined, and the responses of the DoE model and the FE model related to optimal values were compared to evaluate the DoE model.

Table 6.2. Design factors and their dimensions at each level

Design factor	Levels		
	-1	0	+1
Plate material	Composite (e-glass/epoxy)	NiTi (Nitinol)	316L stainless steel
Plate thickness (mm)	2.5	3.5	4.5
Number of screws	7	9	11

Table 6.3. Matrix of corresponding levels and number of runs

Run	Plate thickness	Number of screws	Plate material
1	-1 (2.5 mm)	-1 (7 Screws)	-1 (Composite)
2	-1 (2.5 mm)	0 (9 Screws)	0 (Nitinol)
3	-1 (2.5 mm)	1 (11 Screws)	1 (Stainless steel)
4	0 (3.5 mm)	-1 (7 Screws)	0 (Nitinol)
5	0 (3.5 mm)	0 (9 Screws)	1 (Stainless steel)
6	0 (3.5 mm)	1 (11 Screws)	-1 (Composite)
7	1 (4.5 mm)	-1 (7 Screws)	1 (Stainless steel)
8	1 (4.5 mm)	0 (9 Screws)	-1 (Composite)
9	1 (4.5 mm)	1 (11 Screws)	0 (Nitinol)
10	0 (3.5 mm)	1 (11 Screws)	1 (Stainless steel)

6.4 Results

Table 6.4 demonstrates the matrix of level definition which is completed by response data from the FE models.

The maximum von Mises stress and displacement from FE model of intact bone were determined to be 25.9MPa and 0.0678mm, respectively, and are demonstrated in Fig.6.3 (a) and (b) respectively. Figs.6.4 and 6.5 show the influences of the design factors on the biomechanical responses in chart form, showing the no-interactions and 2-way interactions in the DoE model respectively. These plots are for identification of factors with the strongest effect on biomechanical responses ($p<0.05$). Fig.6.4 demonstrates that the plate material and its thickness have the dominant influence on the crack opening, displacement, stress shielding rate and the maximum stress in the bone and plate. The plate material is the most influential design factor, and the plate thickness is the second most influential design factor on the responses. The variation of the number of screws had no specific influence on the responses in the Fig.6.4. Additionally, no dominant influence factor in the maximum stress of the screws is observed in Fig.6.4 (c). Therefore, the DoE model including 2-way interaction was conducted and the charts of influential factors were generated, which are shown in Fig.6.5. It can be observed in Fig.6.5 that plate material and its thickness are dominant influential factors in all response variables. Also, Fig.6.6 (c) demonstrates that the number of screws, the plate thickness and the linear interaction of these factors have the strongest effect on the stress of screws. The most influential design factors were determined from Figs.6.4 and 6.5 and the mean plots of dominant factors on the biomechanical responses are shown in Fig.6.6. As it can be seen in Fig.6.6 (c), there is no specific pattern between the design factors and stresses in the screws and the DoE model requires considering the 2-way interaction. The surface plot of stress in screws versus two main effective factors including the number of screws and plate thickness was generated and is shown in Fig.6.7(a). Fig.6.7 (a) reveals that the lowest plate thickness (2.5mm) and lowest number of screws (7 screws) cause the highest stress in the screws, that logically seems to be true. The surface plots of other biomechanical responses including crack opening, displacement, stress shielding rate and the maximum stress in the bone and plate with considering of 2-way interaction are demonstrated in Fig.6.7(b)-(f).

Table 6.4. Level definitions and response data from FE models

Plate thickness (mm)	Number of screws	Plate material	Stress in Bone (MPa)	Stress in Plate (MPa)	Stress in Screws (MPa)	Displacement (mm)	Crack opening (mm)	Stress shielding rate (%)
2.5	7	Composite	18.42	7.95	22.47	0.1016	0.0656	27.2
2.5	9	NiTi	16.2	26.08	19.9	0.0987	0.0566	36.0
2.5	11	316L SS	15.21	35.3	19.41	0.0934	0.0452	39.9
3.5	7	NiTi	15.84	22.32	20.94	0.0921	0.0498	37.4
3.5	9	316L SS	14.53	36.43	21.95	0.0883	0.0383	42.6
3.5	11	Composite	18.06	7.79	20.25	0.1048	0.0642	28.6
4.5	7	316L SS	13.76	23.81	19.42	0.0824	0.0349	45.6
4.5	9	Composite	17.27	6.70	20.15	0.1035	0.0641	31.7
4.5	11	NiTi	14.97	17.52	19.86	0.0911	0.0413	40.8
3.5	11	316L SS	14.39	28.33	20.89	0.0886	0.0377	43.1

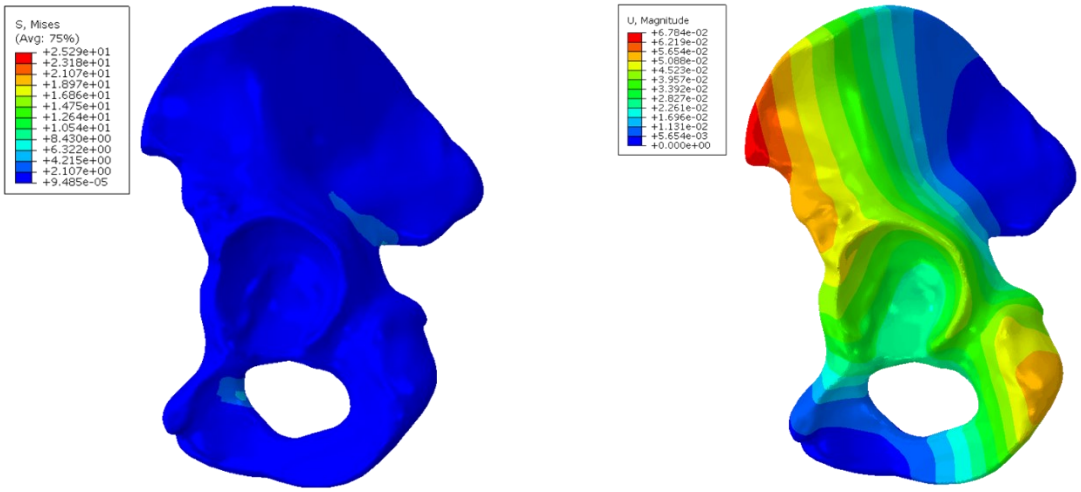

(a) **(b)**

Figure 6.3. Maximum von Mises stress (a) and displacement (b) in the intact bone

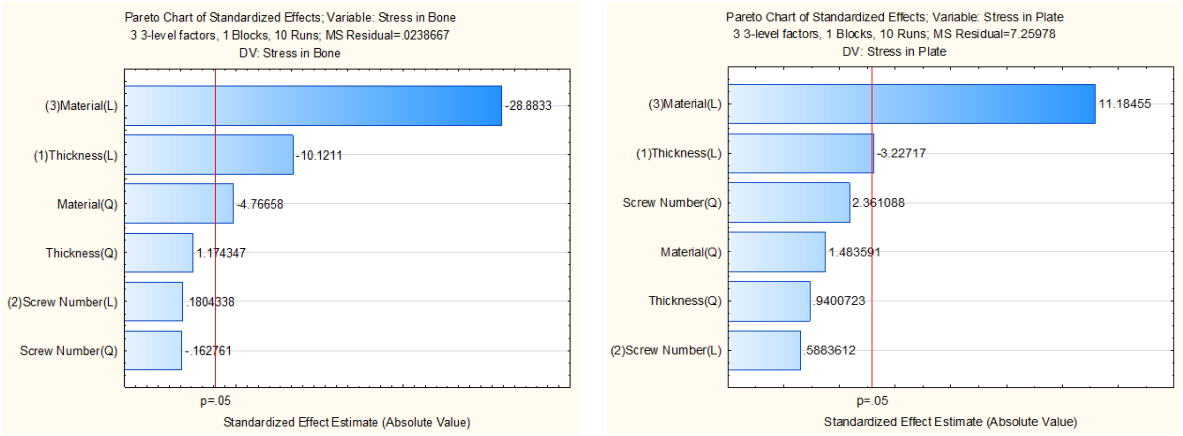

(a) **(b)**

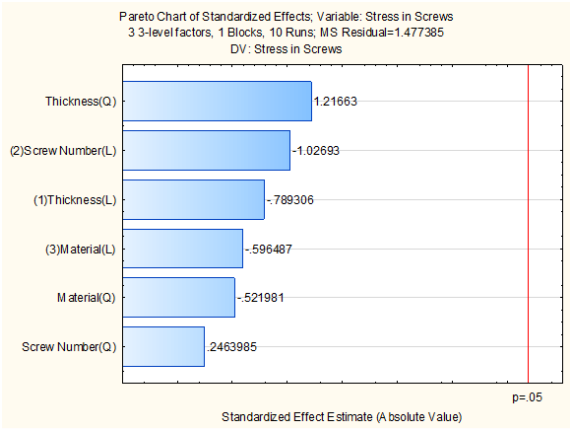

(c)

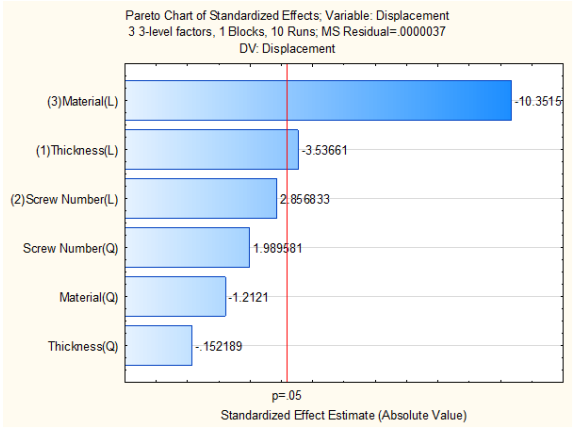

(d)

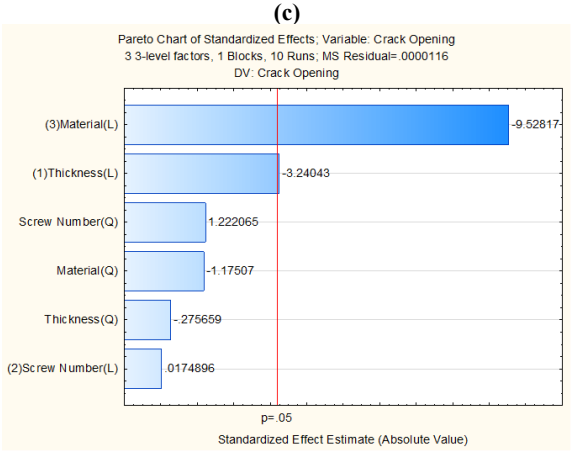

(e)

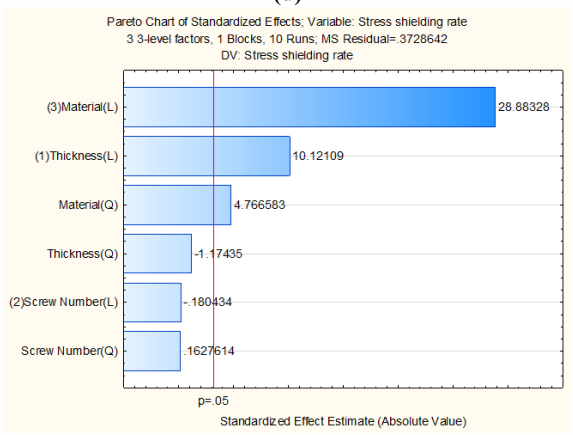

(f)

Figure 6.4. Pareto chart of effects (including no interaction in DoE model) for (a) Bone stress(MPa) (b) plate stress(MPa) (c) screws stress(MPa) (d) displacement(mm) (e) crack opening(mm) (f) stress shielding ratio(%)

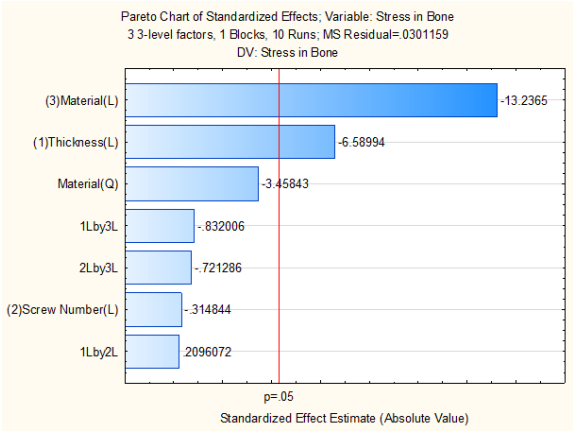

(a)

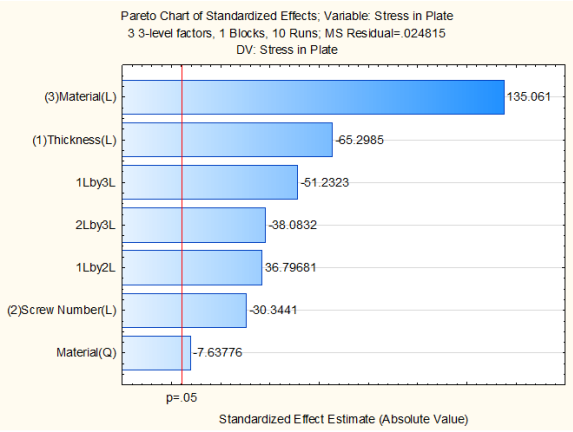

(b)

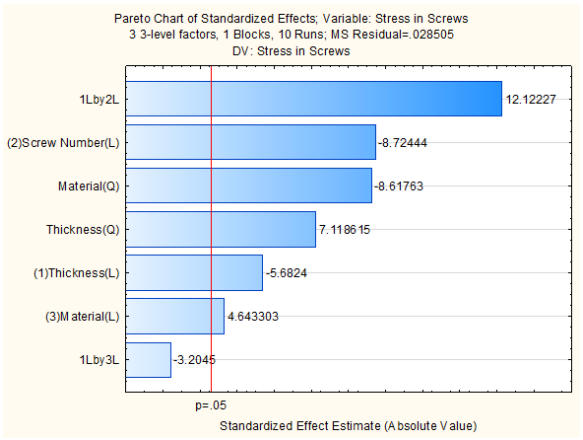

(c)

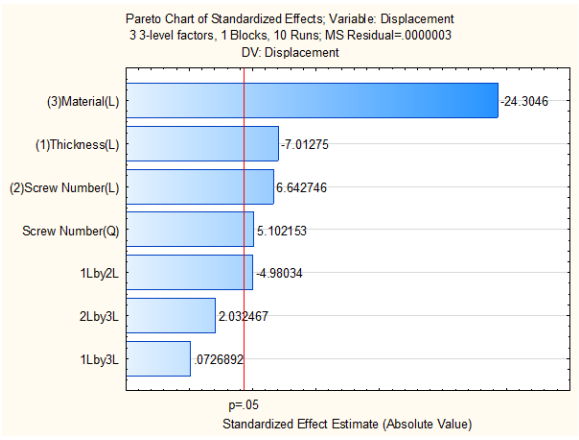

(d)

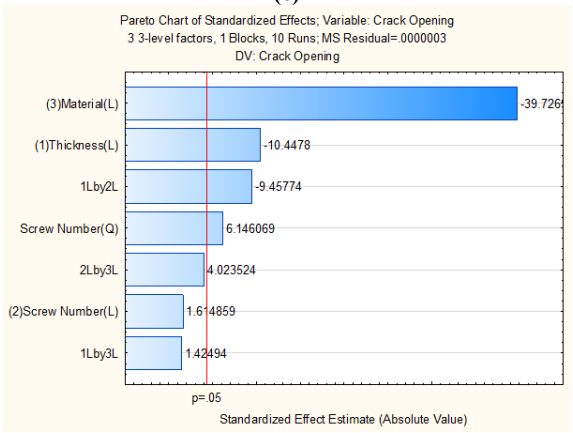

(e)

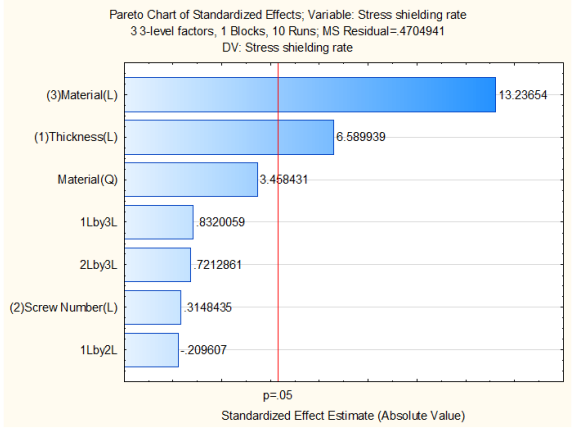

(f)

Figure 6.5. Pareto chart of effects (including 2-way interaction in DoE model) for (a) Bone stress(MPa) (b) plate stress(MPa) (c) screws stress(MPa) (d) displacement(mm) (e) crack opening(mm) (f) stress shielding ratio(%)

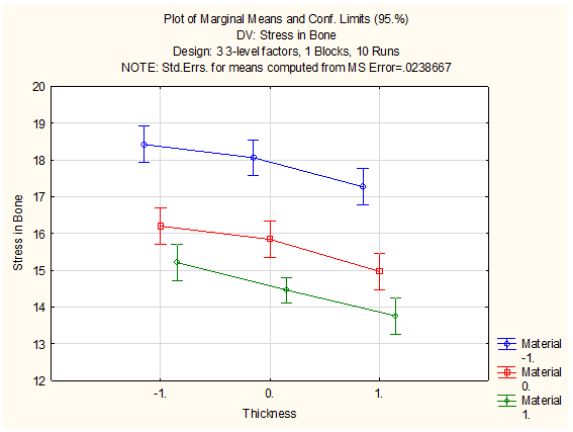

(a)

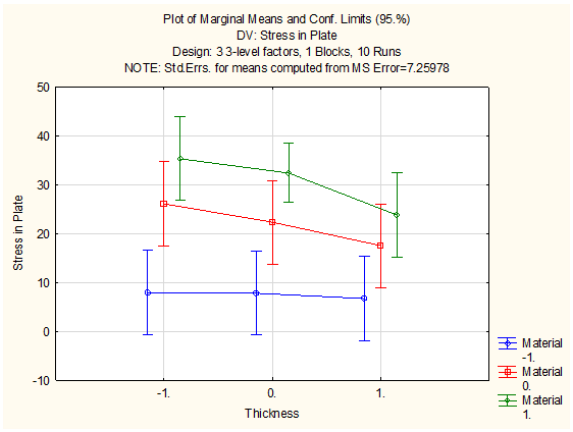

(b)

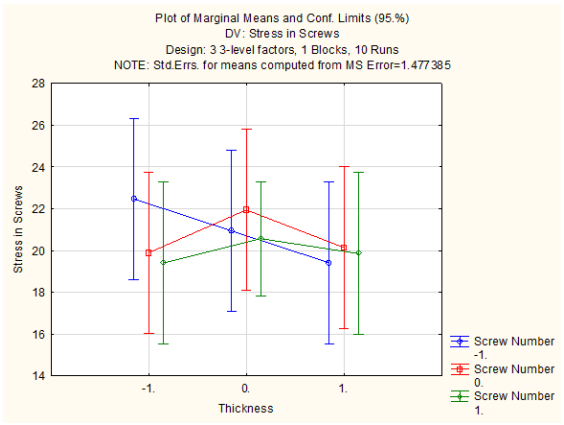

(c)

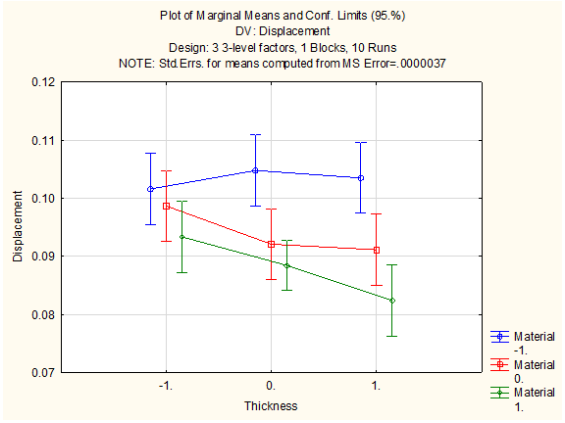

(d)

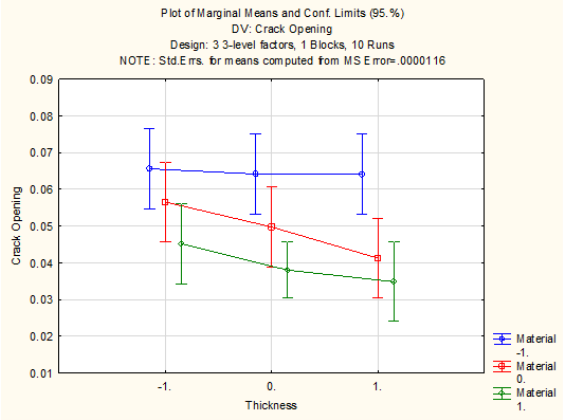

(e)

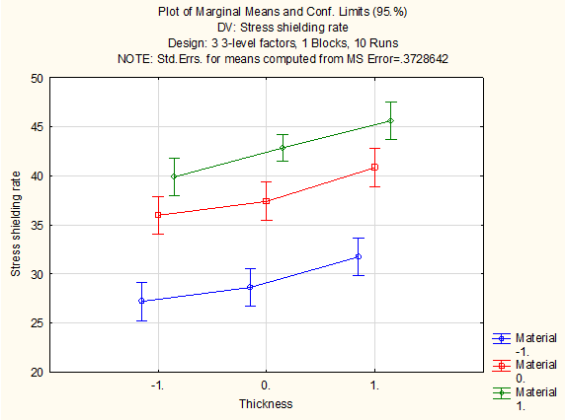

(f)

Figure 6.6. Means plot of dominant factors for (a) Bone stress (b) plate stress (c) screws stress (d) displacement (e) crack opening (f) stress shielding ratio

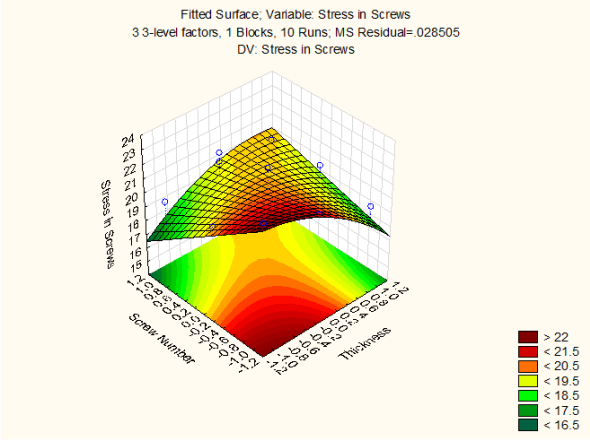

(a)

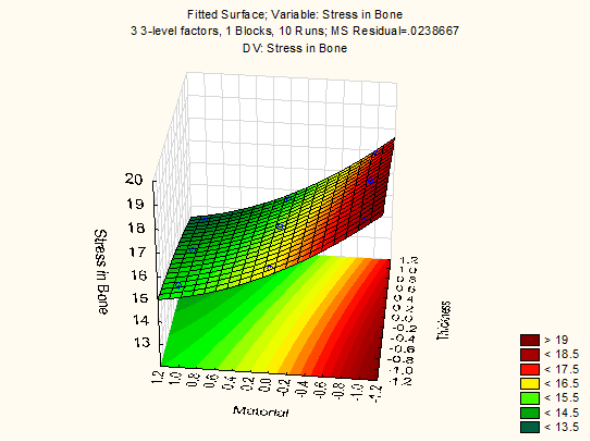

(b)

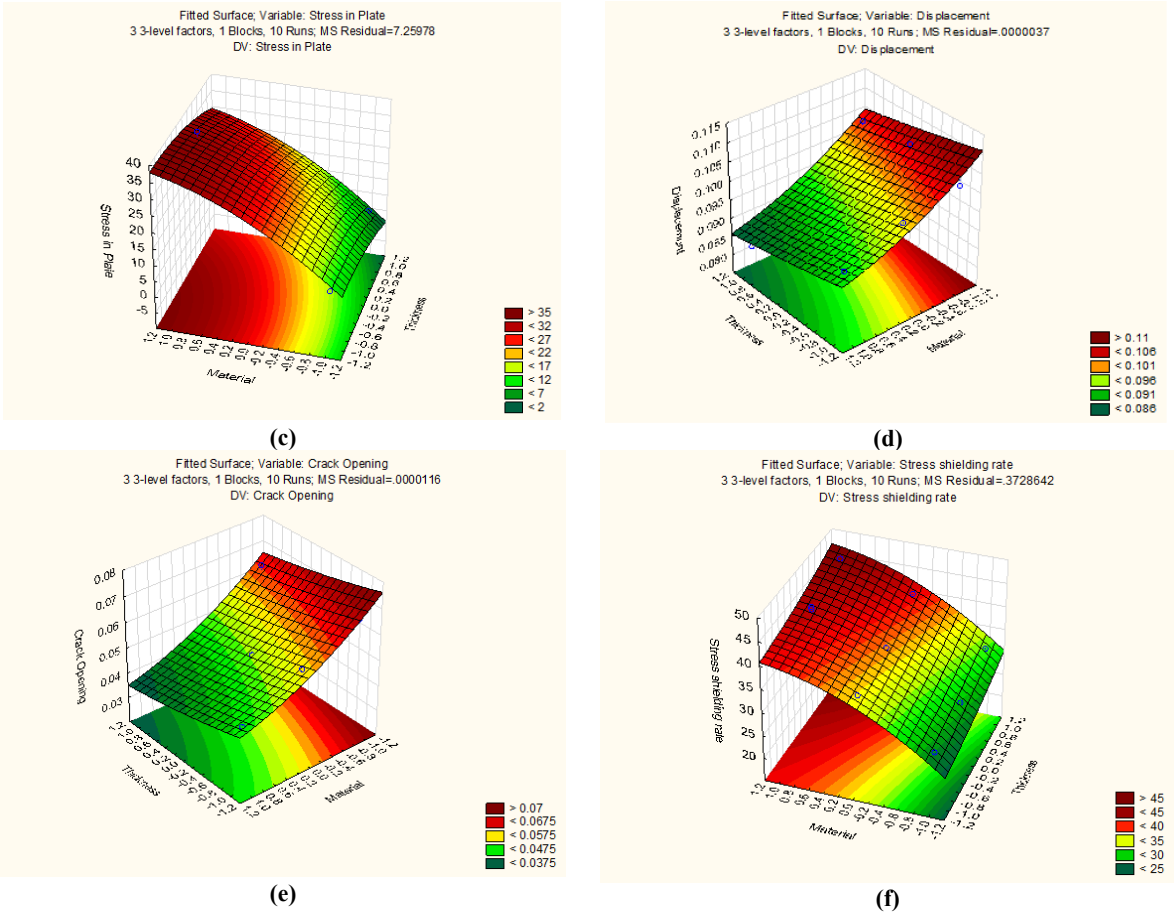

Figure 6.7. surface plot of biomechanical responses vs. effective factors: (a) stress in screws vs. the number of screws and plate thickness; (b) stress in bone vs. plate material and plate thickness; (c) stress in plate vs. plate material and plate thickness; (d) displacement vs. plate material and plate thickness; (e) crack opening vs. plate material and plate thickness; (f) stress shielding rate vs. plate material and plate thickness

To calculate the optimized values of design factors, ANOVA tables and effect estimates tables were generated, and regression equations were obtained to describe each responding variable. The regression equations of crack opening, stress shielding rate, bone displacement, and maximum stresses in the bone and the plate are listed in Equations 6.2-6.6 respectively. In Equations 6.2-6.6, the interaction between the variables has been neglected. As mentioned before, it was observed no dominant factor (with $p<0.05$) for stress in screws in the DoE model with no interaction and it is required to consider the DoE model with 2-way interaction between design factors. Therefore, Equations 6.2-6.6 were recalculated with considering 2-way interaction in the DoE model and the updated equations are listed in Equations 6.7-6.11. The regression equation for stress in the screws with 2-way interaction is indicated in Equation 6.12.

$$CO = 0.05 - 0.013M - 0.0045T \quad (6.2)$$

$$SSR = 36.7 + 6.85M + 2.52T + 1M^2 \quad (6.3)$$

$$D = 0.095 - 0.008M - 0.003T \quad (6.4)$$

$$SB = 16 - 1.73M - 0.64T - 0.26M^2 \quad (6.5)$$

$$SP = 20 + 11.7M - 3.5T \quad (6.6)$$

$$CO = 0.05 - 0.015M - 0.0035T - 0.005(M * T) + 0.002(SN)^2 \quad (6.7)$$

$$SSR = 36.6 + 6.7M + 2.75T \quad (6.8)$$

$$D = 0.095 - 0.009M - 0.002T + 0.002(SN) + 0.001(SN)^2 - 0.003(T * (SN)) \quad (6.9)$$

$$SB = 16 - 1.7M - 0.7T \quad (6.10)$$

$$SP = 20.4 + 15.6M - 6.25T - 7.7(M * T) - 5.4\big(M * (SN)\big) + 6.9\big(T * (SN)\big) - 2.7(SN) - 0.6M^2 \quad (6.11)$$

$$SS = 20.5 + 1.6\big(T * (SN)\big) - 0.8(SN) - 0.6M^2 + 0.4T^2 - 0.4T + 0.4M \quad (6.12)$$

Where CO is crack opening (mm), SSR is stress shielding rate (%), D is displacement (mm), SB is stress in bone (MPa), SP is stress in plate (MPa), SS is stress in screws (MPa), M is plate material (Level -1, 0, 1), T is plate thickness (Level -1, 0, 1) and SN is the number of screws (Level -1, 0, 1).

All the regression Equations 6.2-6.12 should be considered simultaneously to obtain the optimized values of design parameters. The Equations 6.2-6.12 except Equations 6.5,6.10 and 6.12 should be minimized and Equations 6.5 and 6.10 should be maximized up to the stress in the intact bone, the value of which is 25.9 MPa. The SS value obtained from Equation 6.12 should be in the middle range of minimum and maximum. The equations and their conditions were entered to the Wolfram Mathematica software (Wolfram Research Inc., Champaign, IL, USA) and Level 0 (between the three levels of -1, 0 and 1) was determined for M and T to satisfy the conditions of all equations. By looking at the equations, it is apparent that an increase in M and T will decrease the values of CO and D in Equations 6.2,6.4,6.7 and 6.9, while

increasing SSR in Equations 6.3 and 6.8. To minimize all these equations together, Level 0 should be the value of M and T. Also, increasing M and T has a negative effect on maximizing the Equations 6.5 and 6.10 and Level 0 satisfies the condition of these equations as well. SN only appears in Equations 6.7,6.9,6.11 and 6.12 and variation of the number of screws has no specific effect or has very little influence on the values of responses. SN was selected to be Level -1, since drilling the lower number of holes in the pelvic bone will be more convenient for the surgeons and will help to increase the speed of bone healing. By looking at Table 6.2, it is apparent that the NiTi plate with 3.5mm thickness and 7 screws can be a balance between the stress shielding and mechanical stability of the fixation system, thus this was chosen as the optimized plate fixation system.

The results of DoE model for the NiTi plate with 3.5mm thickness and 7 screws were compared to the outputs of FE model from Table 6.4 to evaluate the DoE model and the regression equations. The results of FE model and DoE model (with no interaction and 2-way interaction) for NiTi plate with the thickness of 3.5mm and 7 screws are indicated in the Table 6.5. As it can be seen, the results of DoE model with 2-way interaction are in an excellent agreement with the outputs of FE model.

Table 6.5. Results of DoE and FE models for NiTi plate with 3.5mm thickness and 7 screws

	Stress in Bone (MPa)	Stress in Plate (MPa)	Stress in Screws (MPa)	Displacement (mm)	Crack opening (mm)	Stress shielding rate (%)
DoE model (No interaction)	16.0	20.0	-	0.095	0.05	36.6
DoE model (2-way interaction)	16.0	23.1	21.3	0.094	0.05	36.7
FE model	15.8	22.3	20.9	0.092	0.05	37.4

6.5 Discussion

In this study, the FE model of an intact pelvic bone and a T-style fractured bone fixed by a reconstruction plate and screws were developed. The intact pelvic bone model was developed to be used as a reference for comparing the responses of the treated pelvic bone (i.e. displacement and maximum stresses in the bone). The number of screws, the thickness, and the material of the fixation plate were considered as design factors to assess the effects of variables on biomechanical responses such as crack opening, stress shielding rate, bone displacement,

and maximum stresses in the bone, plate and screws. For the statistical analysis, a three-level fractional factorial design using ANOVA technique was utilized and ten FE models were generated based on the matrix of levels definition. The matrix of level definition was completed by response data from the FE models. The effective factors related to each biomechanical response were defined by the DoE model including no-interaction and 2-way interaction between the design factors. Also, ANOVA tables and effect estimates tables were generated, and regression equations were obtained to describe each responding variable. The investigating of the regression equations revealed that Level 0 of plate material and its thickness is a balance between stress shielding and mechanical stability. The number of screws had no specific influence on the responses and logically, drilling the lower number of holes will be the best selection for choosing the number of screws; therefore, Level -1 was considered for the number of screws. The results of the FE model and DoE model for NiTi plate with 3.5mm thickness with 7 screws were compared to validate the results of DoE model. A good agreement was observed between the results of FE model and DoE model.

The DoE model revealed that the plate material and its thickness are the first and second influential design factors to optimize the fixation system, respectively. The composite plate has the lowest stiffness, highest crack opening/displacement and the lowest stress shielding rate between three selected materials. On the contrary, the stainless-steel plate has the highest stiffness, lowest crack opening/displacement and highest stress shielding rate between all three materials. The results proved that a material with the stiffness in the middle ground of the highest and lowest stiffness such as NiTi can reduce the stress shielding rate without sacrificing essential mechanical stability of the fixation system. Reducing 62.5% of the stiffness of plate material (i.e. changing the material from stainless steel to NiTi), resulted in a decrease of 24.1% in the stability of the fixed bone (i.e. an increase in the average of crack opening) and a decrease of 10.8% of the average of stress shielding rate. As mentioned before, plate thickness is the second influential design factor and affects the same as plate material on the stress shielding rate and mechanical stability of fixation system. Reducing 22.2% of the plate thickness from 4.5mm to 3.5mm resulted in a decrease of 8.6% in the mechanical stability (i.e. an increase in the average of crack opening) and a decrease of 8.1% in the average of stress shielding rate. Contrary to the results for plate material and plate thickness, the it was found that increasing

the number of screws had no significant effect on most of responses such as crack opening, stress shielding rate, bone displacement, and maximum stress in the bone and plate. Reducing the number of screws from 11 to 7 screws had no effect on the average crack opening (0.05 mm for both number of screws) and a little influence on stress shielding rate (~36% for both number of screws). This is an important finding that can be considered by surgeons working on reconstruction of pelvic fractures. However, one limitation is that the effect of less than 7 screws was not studied. Future work could look at optimizing how few screws could be used to still obtain satisfactory results.

It was previously reported [152] that the plate material has an effective performance in reducing the stress shielding and in ensuring the stability of fixation system. In that study [152], the investigation of previously published studies revealed that the special design of fixation plates such as porous plates made by titanium-based alloys might have a better performance in reducing stress shielding without sacrificing essential mechanical stability of the fixation system. Also, several studies [35, 207, 208] investigated the effect of plate thickness in the fixation of different bones and the authors suggested various optimal thickness values based on the plate material, the bones, and the loading conditions of the bones. In another study [208], the various design factors including the number of screws for fixation of distal radius fracture were evaluated. The outputs of that study [208] revealed that the number of screws has no significant effect in fixation of a damaged bone under axial and torsional loading while the number of screws is an effective variable to fix a bone under bending. Our work also shows that modifying the screws between 7-11 had no significant effect. However future work could evaluate the minimum number of screws to use and still provide sufficient fixation.

The objective of this study was to evaluate and optimize the fixation system in T-shaped acetabular fracture. The mechanical stability and stress shielding of fixation systems were assessed by a conjunction of FEA and DoE. The design factors included plate thickness, plate material and the number of screws to determine their influences on biomechanical responses including crack opening, stress shielding rate, bone displacement, and maximum stresses in the bone, plate and screws. The results revealed that plate material and its thickness are the first and second influential parameters on the optimization of fixation system respectively. Also, the

optimized values of fixation plate and the number of screws were obtained by a hybrid model of FEA/DoE. Finally, the hybrid model of FEA and DoE was shown to be a valuable tool to reduce the number of FE models and runs, leading to a significant reduction in the required computational procedure without sacrificing the required results accuracy.

Chapter 7 : Summary and Conclusions

7.1 Summary

In this research, computer modeling was used to investigate micro and macro bone fracture mechanism then to design and optimize the fixation system of a T-shaped fracture pelvic bone. Finite Element Method (FEM) is a very beneficial tool to solve the engineering problems, and to model failure characteristics of solid materials. Recently, the extended finite element method (XFEM) employs fracture mechanics to simulate fracture mechanism in the bulk materials by allowing cracks initiation and propagation through the elements. In this research, the XFEM technique has been implemented to model fracture mechanism in the pelvic bones.

According to the objectives of this research, a comprehensive literature review has been conducted. First, the anatomy of pelvic bones and the types of pelvic bone fracture have been studied. Also, the fixation systems of pelvic bone fractures including T-shaped fracture have been reviewed. Second, the studies related to FE analysis of pelvis ring and pelvic bone have been investigated. The main purpose of conducting this section was a comprehensive coverage of the literature related to fracture modeling of the pelvic bone and its fixation system by FEA. Third, XFEM technique, the knowledge behind this technique and the XFEM formulation have been studied. Fourth and fifth, the studies related to fracture mechanism in the bone tissues including cortical and cancellous tissues on the macro- and micro-scales have been explored. Finally, a review has been conducted related to the material selection and geometrical configuration of reconstruction plates and lag screws. The review covers DoE and Taguchi techniques to optimize the parameters of fixation system related to various bones in human body skeleton.

It was concluded from the literature that considering both cortical and cancellous tissues simultaneously in the fracture modeling of the bones is one of the requirements in developing a realistic modeling. For the cancellous bone modeling, one of the previously published three-point bending test results of a single trabecula were replicated using two different XFEM

approaches (elastic-plastic-fracture; EPF and elastic-fracture; EF) that considered different configurations of the elasto-plastic properties of bone from which the best approach to fit the experimental data was identified. The behavior of a single trabecula was then used in 2D and 3D XFEM models to quantify the strength of trabecular tissue of the forearm along three perpendicular anatomical axes. The stiffness values determined in 2D XFEM in the three anatomical directions were much lower than those reported in literature and varied in both direction as well as tensile/compressive behavior. This suggests that the full 3D network should be considered to more accurately capture the stiffness of cancellous bone. Consequently, the 3D XFEM micro-scale models of cancellous bone specimens were developed. The material behaviors of the bone specimen along all anatomical directions were estimated and the intermediate values of material properties were determined. Additionally, the hysteresis graphs of the specimen were extracted to find the best material model similar to the micro-scale bone. Cast iron plasticity was then selected as a material model to develop an equivalent macro-model. The parameters of the cast iron plasticity model were then selected based on the intermediate material properties of cancellous bone and were assigned to the equivalent macro model. The stress-strain curves of the equivalent model versus those of the micro-scale bone specimen were compared to each other and demonstrated a good agreement. For the cortical bone modeling, previously published materials and failure characteristics of cortical bone have been re-implemented on macro-scale level to be utilized in pelvic bone fracture modeling.

Thus far, material behaviors and failure parameters of cortical and cancellous bones have been estimated. Also, an equivalent model from cancellous tissue in micro-scale level has been developed and evaluated with micro-scale modeling of cancellous specimen. The developed cancellous and cortical models were assigned to an intact pelvic bone with specified cortical and cancellous tissues. Various loading conditions have been applied to the acetabulum, and different types of fracture in pelvic bone have been modeled. The predicated types of fracture and the maximum force at fracture have been compared to those acquired from previously published experimental tests. The types of fracture that have been modeled were similar to the fractures in the experimental tests. However, the fully fracture modeling of the pelvic bone was impractical as simulation runs were time-consuming to be solved.

Finally, the mechanical stability and stress shielding of fixation system in T-shaped acetabular fracture were evaluated and optimized by conjunction of FEA and DoE. In other to do so, the FE model of an intact pelvic bone and a T-shaped damaged bone fixed by plate and screws were developed. Three design factors include plate thickness, plate material and the number of screws were considered to evaluate their effects on biomechanical responses of the bone, implant and the screws. For the statistical analysis, a fractional factorial design at three-levels using Analysis of variance (ANOVA) was utilized. The results revealed that the plate material and its thickness are the most effective parameters in the design of optimal fixation plates. Also, it was observed that the screws number has no specific influence on the responses of fixation system. Additionally, the hybrid model of FEA and DoE proves to be a valuable tool to reduce the number of FE models and runs, leading to a significant reduction in the computational costs without sacrificing the required results accuracy.

7.2 Conclusions

The conclusions of this research can be indicated as following:

- With proper parameters, XFEM is capable of simulating the ductile behavior of cancellous bone.
- Cancellous bone is an orthotropic material that can be simulated using a cast iron plasticity model.
- XFEM model of cancellous bone is able to quantify the tensile strength of trabecular tissue in the various anatomical directions reporting an increased strength in the longitudinal direction of forearm cancellous bone tissue.
- XFEM of cancellous bone proves to be a valuable tool to predict the mechanical characteristics of cancellous bones and to model the fractures in the bone specimen.
- XFEM model of cancellous tissue is capable of replicating the micro-scale behavior in FE analysis simulations without the need for individual trabecula, leading to a reduction in computational resources without sacrificing model accuracy.

- The results of pelvic bone fracture modeling revealed that different types of fracture in the pelvic bones can be caused by the various loading conditions in unstable conditions of high-rate impact loads.
- With proper mechanical and failure behaviors of cortical and cancellous tissues, XFEM model of pelvic bone is capable of predicting the fracture in the bone.
- XFEM models of cancellous and cortical tissues can be assigned to other bones in human body skeleton so that the failure mechanism in such bones can be investigated.
- For design and optimization of fixation system in T-shaped pelvic bone fracture, plate material and plate thickness are the most effective parameters.
- Increasing the number of screws to fix a T-shaped pelvic bone fracture has no significant effect on the most of biomechanical responses such as crack opening, stress shielding rate, bone displacement and maximum stress in bone and plate. This achievement can be considered by the surgeons of pelvic bones.
- For design and optimization of fixation system in T-shaped pelvic bone fracture, the hybrid model of FEA and DoE proves to be a valuable tool to reduce the number of FE models and runs, leading to a significant reduction in the computational costs without sacrificing the required results accuracy.

7.3 Future Considerations

As a result of this research, there are several further investigations in following areas:

1. The size of cancellous bone specimen has been used in this research was considered to be 1.75mm according to the limitations of ABAQUS software to model fracture in the specimen with the larger size specimens. Utilizing the specimen with the larger size and finer mesh might help to improve the results of cancellous bone.

2. Develop the 3D modeling and experimental tests on the specimens with various densities to correlate tensile and compressive strength and stiffness with density.

3. Calibrate the cancellous and cortical XFEM models with several specimens from various bones in different locations of human body skeleton and validate the calibrated models with the experimental tests from the same samples.

4. In this research, the results revealed that cancellous bone is an orthotropic material with various behaviors in three anatomical directions, and such result was consistent with those obtained in the literature. However, the cast iron plasticity model can be used for isotropic materials with the same behaviors in all directions. To utilize the built-in material model for developing the equivalent specimen, the cancellous bone was considered to be initially isotropic with the intermediate material properties from three axial directions, which is a limitation of the present work. At the next step, an equivalent model with orthotropic behaviors in three anatomical directions like cancellous bone in micro-scale can be developed and utilized in the pelvic bone fracture modeling.

5. Mechanical characteristics of bone tissues including elastic modulus and ultimate strength are different in various directions based on the volume fraction or density of specimens, fabric orientation of the bone and anatomical locations of the specimens. The cortical and cancellous specimens of this research were not selected from the pelvic bone. With proper mechanical and failure behaviors of cortical and cancellous tissues (by the specimens extracted from human pelvic bone), the results of XFEM model of pelvic bone might have a better agreement with experimental results.

6. Develop the XFEM model of pelvic bone based on the CT scan data of a pelvic bone sample, assign the material properties of pelvic bone tissues from the samples extracted from the pelvic bone sample, and finally validate the XFEM model with the same sample that the model was created based on.

7. XFEM model of cancellous and cortical tissues with proper mechanical and failure behaviors can be assigned to other bones in human body skeleton so that the failure mechanism in such bones can be investigated.

8. From the literature, it can be concluded that fully constrained boundary conditions utilized in XFEM models of pelvic bone are extremely simplified. Considering more realistic boundary conditions (e.g., using muscular and ligaments) might help to improve the FE results compared to the experimental results.

9. Develop the failure and fracture model to design products to evaluate their performance.

10. Develop the models in micro and macro scales with nonhomogeneous mechanical properties.

11. Considering viscoelastic effects in the modeling of pelvic bone under high-rate impact loads.

12. Model the stress fractures in the weight-bearing bones (e.g., leg and foot).

13. Considering comprehensive design factors for DoE model to define and optimize the effective factors. The design factors that can be optimized include, but are not limited to, (1) screw configurations such as the placement of screws in the locking plates, the length and diameter of screws; (2) further reduction in screw number and (3) the shape, length and width of the locking plates.

14. Develop a hybrid of FEA/DoE to investigate the performance of porous locking plates with different material selections to reduce the stress shielding effects in the fixed bone.

References

1. Lee, C.-H., C.-C. Hsu, and P.-Y. Huang, *Biomechanical study of different fixation techniques for the treatment of sacroiliac joint injuries using finite element analyses and biomechanical tests.* Computers in biology and medicine, 2017. **87**: p. 250-257.
2. Liu, D., et al., *Design and biomechanical study of a novel adjustable hemipelvic prosthesis.* Medical Engineering and Physics, 2016. **38**(12): p. 1416-1425.
3. Shim, V., et al., *Finite element analysis of acetabular fractures—development and validation with a synthetic pelvis.* Journal of biomechanics, 2010. **43**(8): p. 1635-1639.
4. Fan, Y., et al., *Biomechanical analysis of the fixation system for T-shaped acetabular fracture.* Computational and mathematical methods in medicine, 2015. **2015**.
5. Tile, M., D. Helfet, and J. Kellam, *Fractures of the pelvis and acetabulum*. 2003: Lippincott Williams & Wilkins.
6. Lei, J., et al., *Biomechanical analysis of the fixation systems for anterior column and posterior hemi-transverse acetabular fractures.* Acta Orthopaedica et Traumatologica Turcica, 2017.
7. Lei, J., et al., *The influence of pelvic ramus fracture on the stability of fixed pelvic complex fracture.* Computational and mathematical methods in medicine, 2015. **2015**.
8. Shi, D., et al., *3-D finite element analysis of the influence of synovial condition in sacroiliac joint on the load transmission in human pelvic system.* Medical engineering & physics, 2014. **36**(6): p. 745-753.
9. Wang, J.P., et al. *3D finite elemental analysis on treatment of sacral fractures with different internal fixation implants*. in *Applied Mechanics and Materials*. 2013. Trans Tech Publ.
10. Ireland, A., et al., *3D surface imaging in dentistry-what we are looking at.* British dental journal, 2008. **205**(7): p. 387.
11. Han, S., et al., *Alternative mechanical evaluation method for ceramic hip joint implants utilizing finite element analysis under in vivo-like conditions.* Journal of Biomechanical Science and Engineering, 2012. **7**(4): p. 336-348.
12. Dawson, J.M., B.V. Khmelniker, and M.P. McAndrew, *Analysis of the structural behavior of the pelvis during lateral impact using the finite element method.* Accident Analysis & Prevention, 1999. **31**(1): p. 109-119.
13. Linstrom, N.J., et al., *Anatomical and biomechanical analyses of the unique and consistent locations of sacral insufficiency fractures.* Spine, 2009. **34**(4): p. 309.
14. Snedeker, J.G., M.H. Muser, and F.H. Walz, *Assessment of pelvis and upper leg injury risk in car-pedestrian collisions: comparison of accident statistics, impactor tests and a human body finite element model.* Stapp car crash journal, 2003. **47**: p. 437.
15. Song, W., D. Zhou, and Y. He, *The biomechanical advantages of bilateral lumbo-iliac fixation in unilateral comminuted sacral fractures without sacroiliac screw safe channel: A finite element analysis.* Medicine, 2016. **95**(40).
16. Liu, D., et al., *Biomechanical analysis of a novel hemipelvic endoprosthesis during ascending and descending stairs.* Proceedings of the Institution of Mechanical Engineers, Part H: Journal of Engineering in Medicine, 2016. **230**(10): p. 962-975.
17. Song, W., D. Zhou, and Y. He, *Biomechanical characteristics of fixation methods for floating pubic symphysis.* Journal of orthopaedic surgery and research, 2017. **12**(1): p. 38.
18. Salasek, M., et al., *Biomechanical comparison of a transiliac internal fixator and two iliosacral screws in transforaminal sacral fractures: a finite element analysis.* Acta of bioengineering and biomechanics, 2015. **17**(1).
19. Ma, Z., J. Chen, and F. Lan, *BIOMECHANICAL RESPONSE AND INJURY OF OCCUPANT'S PELVIS IN SIDE IMPACTS: EFFECTS OF THE FEMORAL HEAD AND LOADING CONDITIONS.* Journal of Mechanics in Medicine and Biology, 2014. **14**(06): p. 1440001.

20. Li, Z., et al., *Biomechanical response of the pubic symphysis in lateral pelvic impacts: a finite element study.* Journal of Biomechanics, 2007. **40**(12): p. 2758-2766.
21. Lee, C.-H., C.-C. Hsu, and P.-Y. Huang, *Biomechanical study of different fixation techniques for the treatment of sacroiliac joint injuries using finite element analyses and biomechanical tests.* Computers in Biology and Medicine, 2017.
22. Zhang, L., et al., *Biomechanical study of four kinds of percutaneous screw fixation in two types of unilateral sacroiliac joint dislocation: a finite element analysis.* Injury, 2014. **45**(12): p. 2055-2059.
23. Kaku, N., et al., *Biomechanical study of load transfer of the pubic ramus due to pelvic inclination after hip joint surgery using a three-dimensional finite element model.* Journal of Orthopaedic Science, 2004. **9**(3): p. 264-269.
24. Li, Z., et al., *A biomechanical study of periacetabular defects and cement filling.* Journal of biomechanical engineering, 2007. **129**(2): p. 129-136.
25. Böhme, J., et al., *Clinical implementation of finite element models in pelvic ring surgery for prediction of implant behavior: a case report.* Clinical Biomechanics, 2012. **27**(9): p. 872-878.
26. Bodzay, T., I. Flóris, and K. Váradi, *Comparison of stability in the operative treatment of pelvic injuries in a finite element model.* Archives of orthopaedic and trauma surgery, 2011. **131**(10): p. 1427-1433.
27. Zhao, Y., et al., *Comparison of stability of two kinds of sacro-iliac screws in the fixation of bilateral sacral fractures in a finite element model.* Injury, 2012. **43**(4): p. 490-494.
28. Majumder, S., A. Roychowdhury, and S. Pal, *Simulation of hip fracture in sideways fall using a 3D finite element model of pelvis–femur–soft tissue complex with simplified representation of whole body.* Medical engineering & physics, 2007. **29**(10): p. 1167-1178.
29. Majumder, S., A. Roychowdhury, and S. Pal, *Effects of trochanteric soft tissue thickness and hip impact velocity on hip fracture in sideways fall through 3D finite element simulations.* Journal of biomechanics, 2008. **41**(13): p. 2834-2842.
30. Majumder, S., A. Roychowdhury, and S. Pal, *Effects of body configuration on pelvic injury in backward fall simulation using 3D finite element models of pelvis–femur–soft tissue complex.* Journal of biomechanics, 2009. **42**(10): p. 1475-1482.
31. Grujicic, M., et al., *Design-optimization and material selection for a proximal radius fracture-fixation implant.* Journal of materials engineering and performance, 2010. **19**(8): p. 1090-1103.
32. Huang, S.-F., L.-J. Lo, and C.-L. Lin, *Biomechanical optimization of a custom-made positioning and fixing bone plate for Le Fort I osteotomy by finite element analysis.* Computers in biology and medicine, 2016. **68**: p. 49-56.
33. Gutwald, R., R. Jaeger, and F.M. Lambers, *Customized mandibular reconstruction plates improve mechanical performance in a mandibular reconstruction model.* Computer methods in BiomeChaniCs and BiomediCal engineering, 2017. **20**(4): p. 426-435.
34. Sheng, W., et al., *Finite Element-and Design of Experiment-Derived Optimization of Screw Configurations and a Locking Plate for Internal Fixation System.* Computational and mathematical methods in medicine, 2019. **2019**.
35. Mehboob, H. and S.-H. Chang, *Optimal design of a functionally graded biodegradable composite bone plate by using the Taguchi method and finite element analysis.* Composite Structures, 2015. **119**: p. 166-173.
36. Wee, H., et al., *Finite element-derived surrogate models of locked plate fracture fixation biomechanics.* Annals of biomedical engineering, 2017. **45**(3): p. 668-680.
37. Ali, A.A., et al., *Specimen-specific modeling of hip fracture pattern and repair.* Journal of biomechanics, 2014. **47**(2): p. 536-543.
38. Abdel-Wahab, A.A., A.R. Maligno, and V.V. Silberschmidt, *Micro-scale modelling of bovine cortical bone fracture: analysis of crack propagation and microstructure using X-FEM.* Computational Materials Science, 2012. **52**(1): p. 128-135.

39. Abdel-Wahab, A., S. Li, and V.V. Silberschmidt, *Modelling fracture processes in bones*, in *Computational Modelling of Biomechanics and Biotribology in the Musculoskeletal System*. 2014, Elsevier. p. 268-302.
40. Feerick, E.M., X.C. Liu, and P. McGarry, *Anisotropic mode-dependent damage of cortical bone using the extended finite element method (XFEM).* Journal of the mechanical behavior of biomedical materials, 2013. **20**: p. 77-89.
41. Li, S., A. Abdel-Wahab, and V.V. Silberschmidt, *Analysis of fracture processes in cortical bone tissue.* Engineering Fracture Mechanics, 2013. **110**: p. 448-458.
42. Budyn, É. and T. Hoc, *Multiple scale modeling for cortical bone fracture in tension using X-FEM.* European Journal of Computational Mechanics/Revue Européenne de Mécanique Numérique, 2007. **16**(2): p. 213-236.
43. Li, S., et al., *Fracture process in cortical bone: X-FEM analysis of microstructured models.* International Journal of Fracture, 2013. **184**(1-2): p. 43-55.
44. Budyn, E., T. Hoc, and J. Jonvaux, *Fracture strength assessment and aging signs detection in human cortical bone using an X-FEM multiple scale approach.* Computational Mechanics, 2008. **42**(4): p. 579-591.
45. Feerick, E.M. and J.P. McGarry, *Cortical bone failure mechanisms during screw pullout.* Journal of biomechanics, 2012. **45**(9): p. 1666-1672.
46. Budyn, E. and T. Hoc, *Multi-scale modeling of human cortical bone: aging and failure studies.* MRS Online Proceedings Library Archive, 2006. **975**.
47. Besdo, S. and D. Vashishth, *Extended Finite Element models of introcortical porosity and heterogeneity in cortical bone.* Computational Materials Science, 2012. **64**: p. 301-305.
48. Abdel-Wahab, A.A. and V.V. Silberschmidt, *Numerical modelling of impact fracture of cortical bone tissue using X-FEM.* Journal of Theoretical and Applied Mechanics, 2011. **49**: p. 599-619.
49. Abdel-Wahab, A.A., A. Maligno, and V.V. Silberschmidt, *Dynamic properties of cortical bone tissue: Izod tests and numerical study.* Computers Materials and Continua, 2010. **19**(3): p. 217.
50. Ural, A. and S. Mischinski, *Multiscale modeling of bone fracture using cohesive finite elements.* Engineering Fracture Mechanics, 2013. **103**: p. 141-152.
51. Chakladar, N., L.T. Harper, and A. Parsons, *Optimisation of composite bone plates for ulnar transverse fractures.* journal of the mechanical behavior of biomedical materials, 2016. **57**: p. 334-346.
52. Idkaidek, A., S. Koric, and I. Jasiuk, *Fracture analysis of multi-osteon cortical bone using XFEM.* Computational Mechanics, 2017: p. 1-14.
53. Marco, M., et al., *Numerical Modelling of Femur Fracture and Experimental Validation Using Bone Simulant.* Annals of biomedical engineering, 2017. **45**(10): p. 2395-2408.
54. Giambini, H., et al., *Specimen-specific vertebral fracture modeling: a feasibility study using the extended finite element method.* Medical & biological engineering & computing, 2016. **54**(4): p. 583-593.
55. Burr, D.B. and M.R. Allen, *Basic and applied bone biology*. 2013: Academic Press.
56. Budyn, E. and T. Hoc, *Analysis of micro fracture in human Haversian cortical bone under transverse tension using extended physical imaging.* International Journal for Numerical Methods in Engineering, 2010. **82**(8): p. 940-965.
57. Jonvaux, J., T. Hoc, and E. Budyn, *Analysis of micro fracture in human Haversian cortical bone under compression.* International journal for numerical methods in biomedical engineering, 2012. **28**(9): p. 974-998.
58. Idkaidek, A. and I. Jasiuk, *Cortical bone fracture analysis using XFEM–case study.* International journal for numerical methods in biomedical engineering, 2017. **33**(4).
59. Abaqus, *Abaqus user manual (version 6.14).* 2014.
60. Lee, C.-S., et al., *A new constitutive model for simulation of softening, plateau, and densification phenomena for trabecular bone under compression.* Journal of the mechanical behavior of biomedical materials, 2017. **65**: p. 213-223.

61. Hosseini, H.S., et al., *An over-nonlocal implicit gradient-enhanced damage-plastic model for trabecular bone under large compressive strains.* International journal for numerical methods in biomedical engineering, 2015. **31**(11).
62. Hosseini, H.S., D.H. Pahr, and P.K. Zysset, *Modeling and experimental validation of trabecular bone damage, softening and densification under large compressive strains.* Journal of the mechanical behavior of biomedical materials, 2012. **15**: p. 93-102.
63. Pawlikowski, M., K. Jankowski, and K. Skalski, *New microscale constitutive model of human trabecular bone based on depth sensing indentation technique.* Journal of the mechanical behavior of biomedical materials, 2018. **85**: p. 162-169.
64. Hambli, R., *Apparent damage accumulation in cancellous bone using neural networks.* Journal of the mechanical behavior of biomedical materials, 2011. **4**(6): p. 868-878.
65. Gupta, A., et al., *Constitutive modeling and algorithmic implementation of a plasticity-like model for trabecular bone structures.* Computational Mechanics, 2007. **40**(1): p. 61-72.
66. Schwiedrzik, J., et al., *Experimental validation of a nonlinear μFE model based on cohesive-frictional plasticity for trabecular bone.* International journal for numerical methods in biomedical engineering, 2016. **32**(4): p. e02739.
67. Harrison, N.M., et al., *Failure modelling of trabecular bone using a non-linear combined damage and fracture voxel finite element approach.* Biomechanics and modeling in mechanobiology, 2013. **12**(2): p. 225-241.
68. Kelly, N., et al., *An experimental and computational investigation of the post-yield behaviour of trabecular bone during vertebral device subsidence.* Biomechanics and modeling in mechanobiology, 2013. **12**(4): p. 685-703.
69. Tomar, V., *Modeling of dynamic fracture and damage in two-dimensional trabecular bone microstructures using the cohesive finite element method.* Journal of biomechanical engineering, 2008. **130**(2): p. 021021.
70. Song, J.-H., H. Wang, and T. Belytschko, *A comparative study on finite element methods for dynamic fracture.* Computational Mechanics, 2008. **42**(2): p. 239-250.
71. Lee, H., et al., *Application of element deletion method for numerical analyses of cracking.* Journal of Achievements in Materials and Manufacturing Engineering, 2009. **35**(2): p. 154-161.
72. Johnson, P.R., N. Petrinic, and E. Süli, *Element-splitting for simulation of fracture in 3D solid continua.* Computational Plasticity VIII, Fundamentals and Applications, Owen, DRJ, Oñate, E., Suárez, B.(Eds.), Part, 2005. **1**: p. 507-512.
73. Mohammed El Sallah, Z., et al., *Numerical simulation of the femur fracture with and without prosthesis under static loading using extended finite element method (X-FEM).* Journal of Mechanical Engineering, 2017. **14**(1): p. 97-112.
74. Tran, T., H. Lee, and S. Lim, *Modelling porous structures by penalty approach in the extended finite element method.* Computer methods in biomechanics and biomedical engineering, 2013. **16**(4): p. 347-357.
75. Hammond, M.A., et al., *Mechanics of linear microcracking in trabecular bone.* Journal of biomechanics, 2019. **83**: p. 34-42.
76. Giannoudis, P., et al., *Operative treatment of displaced fractures of the acetabulum: a meta-analysis.* The Journal of bone and joint surgery. British volume, 2005. **87**(1): p. 2-9.
77. Masse, A., et al., *Surgical dislocation technique for the treatment of acetabular fractures.* Clinical Orthopaedics and Related Research®, 2013. **471**(12): p. 4056-4064.
78. Siebenrock, K.A., et al., *Surgical dislocation of the femoral head for joint debridement and accurate reduction of fractures of the acetabulum.* Journal of orthopaedic trauma, 2002. **16**(8): p. 543-552.
79. Theumann, N., et al., *Traumatic injuries: imaging of pelvic fractures.* European radiology, 2002. **12**(6): p. 1312-1330.
80. Hadjicostas, P.T. and F.W. Thielemann, *The use of trochanteric slide osteotomy in the treatment of displaced acetabular fractures.* Injury, 2008. **39**(8): p. 907-913.

81. Sagi, H.C., A. Afsari, and D. Dziadosz, *The anterior intra-pelvic (modified rives-stoppa) approach for fixation of acetabular fractures.* Journal of orthopaedic trauma, 2010. **24**(5): p. 263-270.
82. Bhandari, M., et al., *Predictors of clinical and radiological outcome in patients with fractures of the acetabulum and concomitant posterior dislocation of the hip.* The Journal of bone and joint surgery. British volume, 2006. **88**(12): p. 1618-1624.
83. Phillips, A., et al., *Finite element modelling of the pelvis: inclusion of muscular and ligamentous boundary conditions.* Medical engineering & physics, 2007. **29**(7): p. 739-748.
84. Watson, P.J., et al., *The effect of boundary constraints on finite element modelling of the human pelvis.* Medical Engineering & Physics, 2017. **43**: p. 48-57.
85. Hu, P., et al., *Influence of Different Boundary Conditions in Finite Element Analysis on Pelvic Biomechanical Load Transmission.* Orthopaedic surgery, 2017. **9**(1): p. 115-122.
86. Hao, Z., et al., *The effect of boundary condition on the biomechanics of a human pelvic joint under an axial compressive load: a three-dimensional finite element model.* Journal of biomechanical engineering, 2011. **133**(10): p. 101006.
87. Dalstra, M. and R. Huiskes, *Load transfer across the pelvic bone.* Journal of biomechanics, 1995. **28**(6): p. 715-724.
88. Dalstra, M., R. Huiskes, and L. Van Erning, *Development and validation of a three-dimensional finite element model of the pelvic bone.* of the pel\ic bone and design criteria for acetabular prostheses, 1995: p. 37.
89. Anderson, A.E., et al., *Subject-specific finite element model of the pelvis: development, validation and sensitivity studies.* Journal of biomechanical engineering, 2005. **127**(3): p. 364-373.
90. Ivanov, A., et al. *Finite element modeling and analysis of human pelvis*. in *Conference of Bioengineering Division of American Society of Mechanical Engineering*. 2007.
91. Eichenseer, P.H., D.R. Sybert, and J.R. Cotton, *A finite element analysis of sacroiliac joint ligaments in response to different loading conditions.* Spine, 2011. **36**(22): p. E1446-E1452.
92. Idelsohn, S., et al., *COMBINED FINITE ELEMENT AND MUSCULOSKELETAL MODELS FOR ANALYSIS OF PELVIS THROUGHOUT THE GAIT CYCLE.* 2015.
93. Kuraria, S. and V. Kumar, *Three Dimensional Finite Element Analysis of Pelvic Bone.* 2016.
94. Zant, N., et al., *In vitro fatigue failure of cemented acetabular replacements: a hip simulator study.* Journal of biomechanical engineering, 2008. **130**(2): p. 021019.
95. Watson, P.J., M.J. Fagan, and C.A. Dobson, *Sensitivity to model geometry in finite element analyses of reconstructed skeletal structures: Experience with a juvenile pelvis.* Proceedings of the Institution of Mechanical Engineers, Part H: Journal of Engineering in Medicine, 2015. **229**(1): p. 9-19.
96. Watson, P., et al., *Validation of a morphometric reconstruction technique applied to a juvenile pelvis.* Proceedings of the Institution of Mechanical Engineers, Part H: Journal of Engineering in Medicine, 2011. **225**(1): p. 48-57.
97. Mei, J., et al., *Femur performed better than tibia in autologous transplantation during hemipelvis reconstruction.* World journal of surgical oncology, 2014. **12**(1): p. 1.
98. Kumar, A.Y., et al., *SYMMETRY OF THE PELVIS USING VOLUME AND DEVIATION ANALYSIS.* 2016.
99. Ali, S., et al. *Pelvic ring fractures: External fixation comparative numerical structural analysis*. in *Biomedical Engineering Conference (CIBEC), 2014 Cairo International*. 2014. IEEE.
100. Frydrýšek, K., et al., *Design of external fixators used in traumatology and orthopaedics–treatment of fractures of pelvis and its acetabulum.* Procedia Engineering, 2012. **48**: p. 164-173.
101. Zhao, Y., et al., *Mechanical comparison between lengthened and short sacroiliac screws in sacral fracture fixation: a finite element analysis.* Orthopaedics & Traumatology: Surgery & Research, 2013. **99**(5): p. 601-606.

102. Bodzay, T., et al., *How bilateral iliolumbar fusion increases the stability of horizontal osteosynthesis in unstable pelvic ring injuries?* Archives of orthopaedic and trauma surgery, 2013. **133**(7): p. 947-952.
103. Fu, S., et al., *Comparison of the risk of breakage of two kinds of sacroiliac screws in the treatment of bilateral sacral fractures.* European Spine Journal, 2014. **23**(7): p. 1558-1567.
104. Sztrinkai, G., et al., *Further development of our finite element pelvic model to compare fixation methods for pelvic fractures.* Eklem Hastalik Cerrahisi, 2014. **25**(1): p. 8-14.
105. Bodzay, T., et al., *Does surgically fixation of pubic fracture increase the stability of the operated posterior pelvis?* Eklem Hastalik Cerrahisi, 2014. **25**(2): p. 91-95.
106. Sztrinkai, G., et al., *Intrapelvic acetabulum surgery: does the positioning of the plate fixation play a role in the stability of the osteosynthesis?* Eklem Hastaliklari ve Cerrahisi-Joint Diseases and Related Surgery, 2015. **26**(3): p. 126-130.
107. Garcıa, J., et al., *Three-dimensional finite element analysis of several internal and external pelvis fixations.* Journal of biomechanical engineering, 2000. **122**(5): p. 516-522.
108. Shim, V., et al., *An efficient and accurate prediction of the stability of percutaneous fixation of acetabular fractures with finite element simulation.* Journal of biomechanical engineering, 2011. **133**(9): p. 094501.
109. Jia, Y., et al. *Finite element analysis of pelvic reconstruction using fibular transplantation fixed with rod-screw system after type I resection*. in *Bioinformatics and Biomedical Engineering, 2007. ICBBE 2007. The 1st International Conference on*. 2007. IEEE.
110. Chen, B., et al. *A Computational-Biomechanical Evaluation of Three Different Functional-Reconstructions with Internal Fixation Following Resection of Peri-Acetabular Tumors*. in *Bioinformatics and Biomedical Engineering, 2008. ICBBE 2008. The 2nd International Conference on*. 2008. IEEE.
111. Mei, J., Y. Chen, and M. Ni. *Biomechanical Study on the Stability and Finite-Element Analysis of Stress Distribution in Reconstructed Pelvis with Autograft After Hindquarter Amputation*. in *Bioinformatics and Biomedical Engineering, 2009. ICBBE 2009. 3rd International Conference on*. 2009. IEEE.
112. Baoqing, P., et al. *Finite element analysis of acetabular transverse fracture reconstruction treated with different internal fixation methods*. in *Optoelectronics and Image Processing (ICOIP), 2010 International Conference on*. 2010. IEEE.
113. Liao, S.-h., R.-f. Tong, and M. Tang. *Computer aided design and evaluation of new anatomic fixation system on entire pelvic model*. in *2009 SIAM/ACM Joint Conference on Geometric and Physical Modeling*. 2009. ACM.
114. Yao, F., et al., *Comparison of biomechanical characteristics and pelvic ring stability using different fixation methods to treat pubic symphysis diastasis: a finite element study.* Medicine, 2015. **94**(49).
115. Liu, X.-M., et al., *Finite element analysis of the stability of combined plate internal fixation in posterior wall fractures of acetabulum.* International journal of clinical and experimental medicine, 2015. **8**(8): p. 13393.
116. Chen, H., et al., *Parallel analysis of finite element model controlled trial and retrospective case control study on percutaneous internal fixation for vertical sacral fractures.* BMC musculoskeletal disorders, 2013. **14**(1): p. 217.
117. Andrishak, D., et al., *SCREW FIXATION IN DUAL PUBIC RAMI PELVIC FRACTURES.* 2016.
118. Kikuchi, Y., Y. Takahashi, and F. Mori, *Full-scale validation of a human FE model for the pelvis and lower limb of a pedestrian*. 2008, SAE Technical Paper.
119. Van Rooij, L., et al., *A finite element lower extremity and pelvis model for predicting bone injuries due to knee bolster loading*. 2004, SAE Technical Paper.
120. Ikeda, M. and Y. Takahashi, *Investigation on Pelvis Injury Indices Using a Human Finite Element Model.* SAE International Journal of Passenger Cars-Mechanical Systems, 2010. **3**(2010-01-1169): p. 821-829.

121. Silvestri, C. and M. Ray, *Development of a finite element model of the knee-thigh-hip of a 50th percentile male including ligaments and muscles.* International Journal of crashworthiness, 2009. **14**(2): p. 215-229.
122. Shen, M., et al., *Finite element modelling of 10-year-old child pelvis and lower extremities with growth plates for pedestrian protection.* International journal of vehicle safety, 2015. **8**(3): p. 263-286.
123. Majumder, S., A. Roychowdhury, and S. Pal, *Three-dimensional finite element simulation of pelvic fracture during side impact with pelvis–femur–soft tissue complex.* International journal of crashworthiness, 2008. **13**(3): p. 313-329.
124. Yue, N. and C.D. Untaroiu, *A numerical investigation on the variation in hip injury tolerance with occupant posture during frontal collisions.* Traffic injury prevention, 2014. **15**(5): p. 513-522.
125. Gunji, Y., M. Okamoto, and Y. Takahashi. *Examination of human body mass influence on pedestrian pelvis injury prediction using a human FE model*. in *Proceedings of the International Research Council on the Biomechanics of Injury conference*. 2012. International Research Council on Biomechanics of Injury.
126. Kim, J.-E., et al., *Finite element model development of a child pelvis with optimization-based material identification.* Journal of Biomechanics, 2009. **42**(13): p. 2191-2195.
127. Hirabayashi, S., et al., *Simulation study on mechanisms of hip fractures in backward falls.* Journal of Biomechanical Science and Engineering, 2013. **8**(4): p. 328-343.
128. Untaroiu, C.D., et al. *The strain distribution and force transmission path through pubic rami during lateral pelvic impacts*. in *International Mechanical Engineering Congress and Exposition, IMECE2008-67791*. 2008.
129. Majumder, S., A. Roychowdhury, and S. Pal, *Dynamic response of the pelvis under side impact load–a three-dimensional finite element approach.* International journal of crashworthiness, 2004. **9**(1): p. 89-103.
130. Kim, J.E., et al., *Childhood obesity as a risk factor for bone fracture: a mechanistic study.* Obesity, 2013. **21**(7): p. 1459-1466.
131. Song, R., et al., *DYNAMIC SIMULATION OF LUMBAR VERTEBRAE AND PELVIS IN HUMAN FALLS.* Acta Medica, 2016. **32**: p. 593.
132. Shim, V., et al., *Development of a Patient-Specific Finite Element Model for Predicting Implant Failure in Pelvic Ring Fracture Fixation.* Computational and mathematical methods in medicine, 2017. **2017**.
133. Besnault, B., et al., *A parametric finite element model of the human pelvis*. 1998, SAE Technical Paper.
134. Documentation, A., *Version 6.14-2.* Dassault Systémes Simulia Corp., Providence, RI, 2014.
135. Hambli, R., *Micro-CT finite element model and experimental validation of trabecular bone damage and fracture.* Bone, 2013. **56**(2): p. 363-374.
136. Niebur, G.L., et al., *High-resolution finite element models with tissue strength asymmetry accurately predict failure of trabecular bone.* Journal of biomechanics, 2000. **33**(12): p. 1575-1583.
137. Nagaraja, S., T.L. Couse, and R.E. Guldberg, *Trabecular bone microdamage and microstructural stresses under uniaxial compression.* Journal of biomechanics, 2005. **38**(4): p. 707-716.
138. Kosmopoulos, V. and T.S. Keller, *Finite element modeling of trabecular bone damage.* Computer Methods in Biomechanics and Biomedical Engineering, 2003. **6**(3): p. 209-216.
139. Van der Linden, J., et al., *Mechanical consequences of bone loss in cancellous bone.* Journal of Bone and Mineral Research, 2001. **16**(3): p. 457-465.
140. Kadir, M.R.A., A. Syahrom, and A. Öchsner, *Finite element analysis of idealised unit cell cancellous structure based on morphological indices of cancellous bone.* Medical & biological engineering & computing, 2010. **48**(5): p. 497-505.

141. Müller, R. and P. Rüegsegger, *Analysis of mechanical properties of cancellous bone under conditions of simulated bone atrophy.* Journal of biomechanics, 1996. **29**(8): p. 1053-1060.
142. Lucchinetti, E., D. Thomann, and G. Danuser, *Review Micromechanical testing of bone trabeculae-potentials and limitations.* Journal of Materials Science, 2000. **35**(24): p. 6057-6065.
143. Pal, S., *Design of artificial human joints & organs*. 2016: Springer.
144. Stölken, J. and J. Kinney, *On the importance of geometric nonlinearity in finite-element simulations of trabecular bone failure.* Bone, 2003. **33**(4): p. 494-504.
145. Thurner, P.J., et al., *High-speed photography of compressed human trabecular bone correlates whitening to microscopic damage.* Engineering fracture mechanics, 2007. **74**(12): p. 1928-1941.
146. Bayraktar, H.H., et al., *Comparison of the elastic and yield properties of human femoral trabecular and cortical bone tissue.* Journal of biomechanics, 2004. **37**(1): p. 27-35.
147. Gong, H., et al., *Apparent-and tissue-level yield behaviors of L4 vertebral trabecular bone and their associations with microarchitectures.* Annals of biomedical engineering, 2016. **44**(4): p. 1204-1223.
148. Ridha, H. and P.J. Thurner, *Finite element prediction with experimental validation of damage distribution in single trabeculae during three-point bending tests.* Journal of the mechanical behavior of biomedical materials, 2013. **27**: p. 94-106.
149. Jungmann, R., et al., *Local strain and damage mapping in single trabeculae during three-point bending tests.* Journal of the mechanical behavior of biomedical materials, 2011. **4**(4): p. 523-534.
150. Ural, A. and D. Vashishth, *Anisotropy of age-related toughness loss in human cortical bone: a finite element study.* Journal of biomechanics, 2007. **40**(7): p. 1606-1614.
151. Ural, A. and D. Vashishth, *Cohesive finite element modeling of age-related toughness loss in human cortical bone.* Journal of biomechanics, 2006. **39**(16): p. 2974-2982.
152. Li, J., et al., *Materials evolution of bone plates for internal fixation of bone fractures, a review.* Journal of Materials Science & Technology, 2019.
153. Dar, F.H., J.R. Meakin, and R.M. Aspden, *Statistical methods in finite element analysis.* Journal of biomechanics, 2002. **35**(9): p. 1155-1161.
154. O'Brien, F.J., D. Taylor, and T.C. Lee, *The effect of bone microstructure on the initiation and growth of microcracks.* Journal of Orthopaedic Research, 2005. **23**(2): p. 475-480.
155. Hambli, R., A. Bettamer, and S. Allaoui, *Finite element prediction of proximal femur fracture pattern based on orthotropic behaviour law coupled to quasi-brittle damage.* Medical engineering & physics, 2012. **34**(2): p. 202-210.
156. Chevalier, Y., et al., *A patient-specific finite element methodology to predict damage accumulation in vertebral bodies under axial compression, sagittal flexion and combined loads.* Computer methods in biomechanics and biomedical engineering, 2008. **11**(5): p. 477-487.
157. Gong, H., M. Zhang, and Y. Fan, *Micro-finite element analysis of trabecular bone yield behavior—effects of tissue nonlinear material properties.* Journal of Mechanics in Medicine and Biology, 2011. **11**(03): p. 563-580.
158. Nalla, R.K., J. Kinney, and R.O. Ritchie, *Mechanistic fracture criteria for the failure of human cortical bone.* Nature materials, 2003. **2**(3): p. 164.
159. Keaveny, T.M., et al., *Differences between the tensile and compressive strengths of bovine tibial trabecular bone depend on modulus.* Journal of biomechanics, 1994. **27**(9): p. 1137-1146.
160. Keaveny, T.M., E.F. Wachtel, and D.L. Kopperdahl, *Mechanical behavior of human trabecular bone after overloading.* Journal of Orthopaedic Research, 1999. **17**(3): p. 346-353.
161. Keaveny, T.M., et al., *Biomechanics of trabecular bone.* Annual review of biomedical engineering, 2001. **3**(1): p. 307-333.
162. Wolfram, U., H.-J. Wilke, and P.K. Zysset, *Damage accumulation in vertebral trabecular bone depends on loading mode and direction.* Journal of biomechanics, 2011. **44**(6): p. 1164-1169.
163. MacNeil, J.A. and S.K. Boyd, *Bone strength at the distal radius can be estimated from high-resolution peripheral quantitative computed tomography and the finite element method.* Bone, 2008. **42**(6): p. 1203-1213.

164. Ren, W., et al., *Two-dimensional X-ray CT image based meso-scale fracture modelling of concrete.* Engineering Fracture Mechanics, 2015. **133**: p. 24-39.
165. Zhou, J., L. Qi, and A.M. Gokhale, *Generation of Three-Dimensional Microstructure Model for Discontinuously Reinforced Composite by Modified Random Sequential Absorption Method.* Journal of Engineering Materials and Technology, 2016. **138**(2): p. 021001.
166. López, C.M., I. Carol, and A. Aguado, *Meso-structural study of concrete fracture using interface elements. I: numerical model and tensile behavior.* Materials and structures, 2008. **41**(3): p. 583-599.
167. Wu, D., et al., *Young's modulus of trabecular bone at the tissue level: a review.* Acta biomaterialia, 2018.
168. Rieger, R., J.-C. Auregan, and T. Hoc, *Micro-finite-element method to assess elastic properties of trabecular bone at micro-and macroscopic level.* Morphologie, 2018. **102**(336): p. 12-20.
169. Yamada, S., S. Tadano, and S. Fukuda, *Nanostructure and elastic modulus of single trabecula in bovine cancellous bone.* Journal of biomechanics, 2014. **47**(14): p. 3482-3487.
170. Szabó, M., M. Taylor, and P. Thurner, *Mechanical properties of single bovine trabeculae are unaffected by strain rate.* Journal of biomechanics, 2011. **44**(5): p. 962-967.
171. Carretta, R., et al., *Novel method to analyze post-yield mechanical properties at trabecular bone tissue level.* Journal of the mechanical behavior of biomedical materials, 2013. **20**: p. 6-18.
172. Alnaas, W., *Nonlinear finite element analysis of quasi-brittle materials*. 2016, Cardiff University.
173. Lang, C., et al., *A simple and efficient preconditioning scheme for heaviside enriched XFEM.* Computational Mechanics, 2014. **54**(5): p. 1357-1374.
174. Krueger, R., *Development and Applications of Benchmark Examples for Static Delamination Propagation Predictions.* 2013.
175. Nawathe, S., et al., *Theoretical effects of fully ductile versus fully brittle behaviors of bone tissue on the strength of the human proximal femur and vertebral body.* Journal of biomechanics, 2015. **48**(7): p. 1264-1269.
176. Nawathe, S., F. Juillard, and T.M. Keaveny, *Theoretical bounds for the influence of tissue-level ductility on the apparent-level strength of human trabecular bone.* Journal of biomechanics, 2013. **46**(7): p. 1293-1299.
177. Røhl, L., et al., *Tensile and compressive properties of cancellous bone.* Journal of biomechanics, 1991. **24**(12): p. 1143-1149.
178. Charlebois, M., M. Pretterklieber, and P.K. Zysset, *The role of fabric in the large strain compressive behavior of human trabecular bone.* Journal of biomechanical engineering, 2010. **132**(12): p. 121006.
179. Ford, C.M. and T.M. Keaveny, *The dependence of shear failure properties of trabecular bone on apparent density and trabecular orientation.* Journal of biomechanics, 1996. **29**(10): p. 1309-1317.
180. Schwiedrzik, J., et al., *Experimental validation of a nonlinear μFE model based on cohesive-frictional plasticity for trabecular bone.* International journal for numerical methods in biomedical engineering, 2016. **32**(4).
181. Frost, H.M., *Wolff's Law and bone's structural adaptations to mechanical usage: an overview for clinicians.* The Angle Orthodontist, 1994. **64**(3): p. 175-188.
182. Verhulp, E., et al., *Indirect determination of trabecular bone effective tissue failure properties using micro-finite element simulations.* Journal of biomechanics, 2008. **41**(7): p. 1479-1485.
183. Morgan, E.F. and T.M. Keaveny, *Dependence of yield strain of human trabecular bone on anatomic site.* Journal of biomechanics, 2001. **34**(5): p. 569-577.
184. Morgan, E.F., H.H. Bayraktar, and T.M. Keaveny, *Trabecular bone modulus–density relationships depend on anatomic site.* Journal of biomechanics, 2003. **36**(7): p. 897-904.
185. Salem, M., et al., *Prediction of Failure in Cancellous Bone using XFEM.* International journal for numerical methods in biomedical engineering.

186. Loweletal, G., *The quality of trabecular bone evaluated with micro-computed tomography, FEA and mechanical testing.* Bone research in biomechanics, 1997. **40**: p. 97.
187. Hou, F.J., et al., *Human vertebral body apparent and hard tissue stiffness.* Journal of biomechanics, 1998. **31**(11): p. 1009-1015.
188. Morgan, E.F., et al., *Contribution of inter-site variations in architecture to trabecular bone apparent yield strains.* Journal of biomechanics, 2004. **37**(9): p. 1413-1420.
189. Bayraktar, H.H. and T.M. Keaveny. *A computational investigation of the nonlinear behavior of human trabecular bone*. in *Transactions of the 12th annual pre-ORS symposium on computational methods in orthopaedic biomechnics*. 2004.
190. Bayraktar, H., *Nonlinear micro finite element analysis of human trabecular bone.* Circle 141-Abaqus Inc, 2004: p. 22-25.
191. Salem, M., et al., *An equivalent constitutive model of cancellous bone with fracture prediction.* Journal of biomechanical engineering, 2020.
192. Ghosh, R., et al., *Finite element analysis of a hemi-pelvis: the effect of inclusion of cartilage layer on acetabular stresses and strain.* Computer methods in biomechanics and biomedical engineering, 2015. **18**(7): p. 697-710.
193. Rupp, J.D., C.A. Flannagan, and S.M. Kuppa, *An injury risk curve for the hip for use in frontal impact crash testing.* Journal of biomechanics, 2010. **43**(3): p. 527-531.
194. Rupp, J.D., et al., *The tolerance of the human hip to dynamic knee loading*. 2002, SAE Technical Paper.
195. Lerner, Z.F. and R.C. Browning, *Compressive and shear hip joint contact forces are affected by pediatric obesity during walking.* Journal of biomechanics, 2016. **49**(9): p. 1547-1553.
196. Parker, M.J., W.J. Gillespie, and L.D. Gillespie, *Hip protectors for preventing hip fractures in older people.* Cochrane database of systematic reviews, 2005(3).
197. Kannus, P., et al., *Prevention of hip fracture in elderly people with use of a hip protector.* New England journal of medicine, 2000. **343**(21): p. 1506-1513.
198. Minns, R., et al., *Are hip protectors correctly positioned in use?* Age and ageing, 2007. **36**(2): p. 140-144.
199. Rupp, J.D., et al. *Comparison of the inertial response of the THORNT, Hybrid III, and unembalmed cadaver to simulated knee-to-knee-bolster impacts*. in *Proceedings of the 19th International Technical Conference on the Enhanced Safety of Vehicles, Paper*. 2005.
200. Rupp, J.D., et al. *Development of new criteria for assessing the risk of knee-thigh-hip injury in frontal impacts using Hybrid III femur force measurements*. in *Proceedings of the 21st International Technical Conference on the Enhanced Safety of Vehicles (Paper 09-0306)*. 2009.
201. Rupp, J.D., et al., *Comparison of Knee/Femur Force-Deflection Response of the THOR, Hybrid III, and Human Cadaver to Dynamic Frontal Impact Knee Loading.* National Highway Traffic Safety Administration, 2003.
202. Porta, D.J., *Biomechanics of impact injury*, in *Forensic Medicine of the Lower Extremity*. 2005, Springer. p. 279-310.
203. Rupp, J.D. and L.W. Schneider, *Injuries to the hip joint in frontal motor-vehicle crashes: biomechanical and real-world perspectives.* Orthopedic Clinics, 2004. **35**(4): p. 493-504.
204. Martín, O., et al., *The T-Shaped Fractures of the Acetabulum.* J Trauma Treat, 2016. **5**(303): p. 2167-1222.1000303.
205. Mehboob, H. and S.-H. Chang, *Evaluation of the development of tissue phenotypes: Bone fracture healing using functionally graded material composite bone plates.* Composite Structures, 2014. **117**: p. 105-113.
206. Lei, J., et al., *Biomechanical analysis of the fixation systems for anterior column and posterior hemi-transverse acetabular fractures.* Acta orthopaedica et traumatologica turcica, 2017. **51**(3): p. 248-253.

207. Kim, J.-D., et al., *Design optimization of a xenogeneic bone plate and screws using the Taguchi and finite element methods.* International Journal of Precision Engineering and Manufacturing, 2011. **12**(6): p. 1119-1124.
208. Chen, A.C.-Y., et al., *Design optimisation and experimental evaluation of dorsal double plating fixation for distal radius fracture.* Injury, 2013. **44**(4): p. 527-534.
209. Armstrong, J.E., et al., *Preliminary investigation of the biomechanics of internal fixation of sagittal split osteotomies with miniplates using a newly designed in vitro testing model.* Journal of oral and maxillofacial surgery, 2001. **59**(2): p. 191-195.
210. Liew, A.S., et al., *Effect of screw placement on fixation in the humeral head.* Journal of shoulder and elbow surgery, 2000. **9**(5): p. 423-426.
211. Piao, C., et al., *Stress shielding effects of two prosthetic groups after total hip joint simulation replacement.* Journal of orthopaedic surgery and research, 2014. **9**(1): p. 71.

Appendix A: Input file of failure modeling in Cancellous Bone using XFEM

A piece of input file of failure modeling (EPF model) in Cancellous Bone using XFEM:

```
*Heading
** Job name: Job-1 Model name: Model-1
** Generated by: Abaqus/CAE 6.14-2
*Preprint, echo=NO, model=NO, history=NO, contact=NO
**
** PARTS
**
*Part, name="Part-2-mesh-2,5mm"
*Node
      1,  -1.15838826, -0.801203549
      2,  -1.20887756,  -0.77740097
      3,  -1.16939187, -0.825496793
      4,  -1.12624943,  -0.77616173
      5,  -1.17697728, -0.714144468
      6,  -1.10875821, -0.833007336
      7,  -1.04743433, -0.731905639
      8,  -1.09115517, -0.676542401
      9,   -1.1324867, -0.631123364
     10,  -1.03315902, -0.839324534
     11,  -0.97689116, -0.712469101
     12,  -1.00999081, -0.691532016
     13,  -1.03497875, -0.661644757
     14,  -1.03468156, -0.623265266
     15,  -1.10193431, -0.594139695
     16, -0.966211855, -0.878381252
     17, -0.859121859, -0.727213919
     18,   -0.9123469, -0.694425404
     19,  -1.01574028,  -0.56374383
     20,  -1.07135892, -0.510055304
     21,  -1.10037541, -0.539265573
     22, -0.933855653, -0.977519214
     23,  -0.84850949, -0.978651881
     24, -0.803513348, -0.760111809
     25, -0.750811875, -0.518502772
     26, -0.890177846, -0.575671375
     27, -0.887831092, -0.627361476
     28, -0.694175422, -0.657165706
     29, -0.929427862, -0.543973148
     30, -0.897898078, -0.427301824
     31, -0.987417102, -0.395211875
     32,  -1.07696438, -0.289503604
     33,  -1.09214306, -0.158129454
     34,  -1.20715177, -0.373482347
     35,  -1.20617723, -0.162365749
     36, -0.926642895,  -1.04012012
     37, -0.846910536,  -1.03333569
     38, -0.787304521, -0.425554276
```

```
      39, -0.521771967, -0.609121144
      40, -0.528864622, -0.497859538
      41,  -0.58853364,  -0.46899128
      42,  -1.20493841,  0.105946951
      43,  -1.10119426,  0.127868444
      44,  -1.01737821, 0.0553725027
      45,  -0.91443342,  -1.25041413
      46, -0.789507806,  -1.25217462
      47, -0.582555294, -0.309374869
      48, -0.686084986, -0.301149517
      49, -0.378441036,  -0.54448837
      50, -0.431479037, -0.466632009
      51, -0.453684241, -0.627414465
      52,  -1.04497874,  0.204421759
      53,  -1.11810124,  0.287217468
      54,  -1.20421839,  0.261949927
      55, -0.865629435,  0.105773315
      56, -0.877890348,  0.184317186
      57, -0.604726553, -0.0281622671
      58, -0.676941097, -0.0240137037
      59,  -0.29274562,  -0.58817935
      60, -0.229710162,  -0.48799926
      61, -0.305602491, -0.376221597
      62, -0.385078698, -0.711435914
      63, -0.292408317, -0.665867865
      64,  -1.15342665,  0.469136775
      65,   -1.2032553,  0.470552474
      66,  -0.67576474,  0.120193966
      67,  -0.71541357,  0.205231547
      68, -0.722537041, 0.0804074183
      69, -0.596850336,  0.139763743
      70,  -0.12715286, -0.454362422
.
.
.
.
.
  15511, -0.232261568, -0.0284877066
  15512, -0.227967024, -0.036658518
  15513, -0.203694239, -0.0319121033
  15514,  -0.20802173, -0.0214332081
  15515, -0.211508185, -0.0104652923
  15516, -0.212130204, -0.033973407
  15517, -0.216033608, -0.0237779506
  15518, -0.219647944, -0.0133308135
  15519, -0.220322967, -0.035270907
  15520,  -0.22415249, -0.0259527583
  15521, -0.227904215, -0.0160335284
*Element, type=CPS4R
    1,   265,     1,   266,  3845
    2,  3845,   266,   267,  3844
    3,  3844,   267,   268,  3843
    4,  3843,   268,   269,  3842
    5,  3842,   269,   270,  3841
```

```
 6,   270,   271,  3846,  3841
 7,   271,     2,   272,  3846
 8,   272,   273,  3847,  3846
 9,   273,   274,  3848,  3847
10,   274,   275,  3849,  3848
11,   275,   276,  3850,  3849
12,   276,     3,   264,  3850
13,  3846,  3847,  3842,  3841
14,  3847,  3848,  3843,  3842
15,  3848,  3849,  3844,  3843
16,  3849,  3850,  3845,  3844
17,  3850,   264,   265,  3845
18,     2,   271,  3851,   292
19,   271,   270,  3852,  3851
20,   270,   269,  3853,  3852
21,   269,   268,  3854,  3853
22,   268,   267,  3855,  3854
23,   267,   266,  3856,  3855
24,   266,     1,   277,  3856
25,   292,  3851,  3857,   291
26,  3851,  3852,  3858,  3857
27,  3852,  3853,  3859,  3858
28,  3853,  3854,  3860,  3859
29,  3854,  3855,  3861,  3860
30,  3855,  3856,  3862,  3861
31,  3856,   277,   278,  3862
32,   291,  3857,  3863,   290
33,  3857,  3858,  3864,  3863
34,  3858,  3859,  3865,  3864
35,  3859,  3860,  3866,  3865
36,  3860,  3861,  3867,  3866
37,  3861,  3862,  3868,  3867
38,  3862,   278,   279,  3868
39,   290,  3863,  3869,   289
40,  3863,  3864,  3870,  3869
41,  3864,  3865,  3871,  3870
42,  3865,  3866,  3872,  3871
43,  3866,  3867,  3873,  3872
44,  3867,  3868,  3874,  3873
45,  3868,   279,   280,  3874
46,   289,  3869,  3875,   288
47,  3869,  3870,  3876,  3875
48,  3870,  3871,  3877,  3876
49,  3871,  3872,  3878,  3877
50,  3872,  3873,  3879,  3878
51,  3873,  3874,  3880,  3879
52,  3874,   280,   281,  3880
53,   288,  3875,   287,     5
54,  3875,  3876,   286,   287
55,  3876,  3877,   285,   286
56,  3877,  3878,   284,   285
57,  3878,  3879,   283,   284
58,  3879,  3880,   282,   283
59,  3880,   281,     4,   282
```

```
   60,   296,     4,   281,  3885
.
.
.
.
.
14140, 15516, 15517, 15520, 15519
14141, 15517, 15518, 15521, 15520
14142, 15518,  3821,  3820, 15521
14143, 15509, 15519, 15512, 15506
14144, 15519, 15520, 15511, 15512
14145, 15520, 15521, 15510, 15511
14146, 15521,  3820,  3819, 15510
14147,  3819,   262,  3834, 15510
14148, 15510,  3834,  3835, 15511
14149, 15511,  3835,  3836, 15512
14150, 15512,  3836,  3837, 15506
*Nset, nset=_PickedSet2_#1, internal, generate
     1,  15521,      1
*Elset, elset=_PickedSet2_#1, internal, generate
     1,  14150,      1
*Nset, nset=_PickedSet3_#1, internal, generate
     1,  15521,      1
*Elset, elset=_PickedSet3_#1, internal, generate
     1,  14150,      1
*Orientation, name=Ori-2
1., 0., 0., 0., 1., 0.
3, 0.
** Section: Section-1
*Solid Section, elset=_PickedSet2_#1, orientation=Ori-2,
material=Material-1
,
*End Part
**
**
** ASSEMBLY
**
*Assembly, name=Assembly
**
*Instance, name="Part-2-mesh-2,5mm-1", part="Part-2-mesh-2,5mm"
0.06803285320282,    -0.005451,           0.
*End Instance
**
*Nset, nset=Set-3, instance="Part-2-mesh-2,5mm-1"
  188,  189,  190,  199,  200,  209,  211,  212,  225, 2838, 2839,
2840, 2841, 2842, 2867, 2868
 2869, 2870, 2871, 2872, 2873, 2874, 2875, 2876, 2990, 2991, 2992,
2993, 2994, 2995, 2996, 2997
 2998, 2999, 3000, 3001, 3160, 3161, 3162, 3163, 3164, 3165, 3166,
3167, 3168, 3169, 3170, 3171
 3172, 3173, 3174, 3175, 3176, 3177, 3178, 3407, 3408, 3409, 3410,
3411, 3412, 3413, 3414, 3415
 3416, 3417, 3418, 3419, 3420, 3421, 3422, 3423, 3424
*Nset, nset=Set-4, instance="Part-2-mesh-2,5mm-1"
```

```
   34,   35,   42,   54,   65,   75,   85,  101,  572,  573,  586,
587,  588,  589,  590,  591
  592,  593,  594,  595,  596,  597,  598,  599,  600,  680,  681,
682,  683,  684,  685,  686
  687,  688,  689,  690,  691,  692,  693,  694,  695,  696,  697,
698,  699,  858,  859,  860
  861,  862,  863,  864,  865,  866,  867,  868, 1049, 1050, 1051,
1052, 1053, 1054, 1055, 1056
 1057, 1058, 1059, 1060, 1061, 1062, 1063, 1064, 1065, 1066, 1207,
1208, 1209, 1210, 1211, 1212
 1213, 1214, 1215, 1216, 1217, 1218, 1219, 1220, 1319, 1320, 1321,
1322, 1323, 1324, 1325, 1326
 1327, 1580, 1581, 1582, 1583, 1584, 1585, 1586, 1587, 1588, 1589,
1590, 1591, 1592, 1593, 1594
*Elset, elset=_PickedSet53, internal, instance="Part-2-mesh-2,5mm-1"
 6468, 6469, 6470, 6471, 6472, 6473, 6474, 6475, 6476, 6477, 6478,
6479, 6480, 6481, 6482, 6483
 6484, 6485, 6486, 6487, 6488, 6489, 6490, 6491, 6492, 6493, 6495,
6496, 6497, 6498, 6499, 6500
 6501, 6502, 6503, 6504, 6505, 6506, 6509, 6510, 6511, 6512, 6513,
6514, 6515, 6516, 6517, 6518
 6519, 6522, 6523, 6524, 6525, 6526, 6527, 6528, 6529, 6530, 6531,
6532, 6535, 6536, 6537, 6538
 6539, 6540, 6541, 6542, 6543, 6544, 6545, 6549, 6550, 6551, 6552,
6553, 6554, 6555, 6556, 6557
 6558, 6562, 6563, 6564, 6565, 6566, 6567, 6568, 6569, 6570, 6571,
6575, 6576, 6577, 6578, 6579
 6580, 6581, 6582, 6583, 6584, 6588, 6589, 6590, 6591, 6592, 6593,
6594, 6595, 6596, 6597, 6601
 6602, 6603, 6604, 6605, 6606, 6607, 6608, 6609, 6610, 6721, 6722,
6723, 6724, 6725, 6726, 6727
 6728, 6729, 6730, 6731, 6732, 6733, 6734, 6735, 6736, 6737, 6738,
6739, 6740, 6741, 6742, 6743
 6744, 6745, 6746, 6747, 6748, 6749, 6750, 6751, 6752, 6753, 6754,
6755, 6756, 6757, 6758, 6759
 6760, 6761, 6762, 6763, 6764, 6765, 6766, 6767, 6768, 6769, 6770,
6771, 6772, 6773, 6774, 6775
 6776, 6777, 6778, 6779, 6780, 6781, 6782, 6783, 6784, 6785, 6786,
6787, 6788, 6789, 6790, 6791
 6792, 6793, 6794, 6795, 6796, 6797, 6798, 6799, 6800, 6801, 6802,
6803, 6804, 6805, 6806, 6807
 6808, 6809, 6810, 6811, 6812, 6813, 6814, 6815, 6816, 6817, 6818,
6819, 7268, 7269, 7270, 7271
 7272, 7273, 7274, 7275, 7277, 7278, 7279, 7280, 7281, 7282, 7283,
7284, 7286, 7287, 7288, 7289
 7290, 7291, 7292, 7293, 7295, 7296, 7297, 7298, 7299, 7300, 7301,
7302, 7304, 7305, 7306, 7307
 7308, 7309, 7310, 7311, 7313, 7314, 7315, 7316, 7317, 7318, 7319,
7320, 7322, 7323, 7324, 7325
 7326, 7327, 7328, 7329, 7331, 7332, 7333, 7334, 7335, 7336, 7337,
7338, 7340, 7341, 7342, 7343
 7344, 7345, 7346, 7347, 7349, 7350, 7351, 7352, 7353, 7354, 7355,
7356, 7357, 7358, 7359, 7360
 7361, 7362, 7363, 7364, 7365
```

```
*Elset, elset=_PickedSet54, internal, instance="Part-2-mesh-2,5mm-1"
 4621, 4622, 4623, 4624, 4625, 4626, 4627, 4628, 4629, 4630, 4631,
5373, 5374, 5375, 5376, 5377
 5378, 5379, 5380, 5381, 5382, 5383, 5384, 5385, 5386, 5387, 5388,
5389, 5390, 5391, 5392, 5393
 5394, 5395, 5396, 5397, 5398, 5399, 5400, 5401, 5402, 5403, 5404,
5405, 5406, 5407, 5408, 5409
 5410, 5411, 5412, 5413, 5414, 5415, 5416, 5417, 5418, 5419, 5420,
5421, 5422, 5423, 5424, 5425
 5426, 5427, 5428, 5429, 5430, 5431, 5432, 5433, 5434, 5435, 5436,
5437, 5438, 5439, 5440, 5441
 5442, 5443, 5444, 5445, 5446, 5447, 5448, 5449, 5450, 5451, 5452,
5453, 5454, 5455, 5456, 5457
 5458, 5459, 5460, 5461, 5462, 5463, 5464, 5465, 5466, 5467, 5468,
5469, 5470, 5471, 6251, 6252
 6253, 6254, 6255, 6256, 6257, 6258, 6259, 6265, 6266, 6267, 6268,
6269, 6270, 6271, 6272, 6273
 6279, 6280, 6281, 6282, 6283, 6284, 6285, 6286, 6287, 6293, 6294,
6295, 6296, 6297, 6298, 6299
 6300, 6301, 6307, 6308, 6309, 6310, 6311, 6312, 6313, 6314, 6315,
6321, 6322, 6323, 6324, 6325
 6326, 6327, 6328, 6329, 6335, 6336, 6337, 6338, 6339, 6340, 6341,
6342, 6343, 6349, 6350, 6351
 6352, 6353, 6354, 6355, 6356, 6357, 6363, 6364, 6365, 6366, 6367,
6368, 6369, 6370, 6371
*Elset, elset=_PickedSet55, internal, instance="Part-2-mesh-2,5mm-1"
 7519, 7520, 7521, 7522, 7523, 7524, 7525, 7526, 7527, 7528, 7529,
7530, 7531, 7532, 7533, 7534
 7535, 7536, 7538, 7539, 7540, 7541, 7542, 7544, 7545, 7546, 7547,
7548, 7550, 7551, 7552, 7553
 7554, 7555, 7556, 7557, 7558, 7559, 7560, 7561, 7562, 7563, 7564,
7565, 7566, 7567, 7568, 7569
 7570, 7571, 7572, 7573, 7574, 7575, 7576, 7577, 7578, 7579, 7581,
7582, 7583, 7584, 7585, 7586
 7588, 8360, 8361, 8362, 8363, 8364, 8365, 8366, 8367, 8368, 8369,
8370, 8371, 8372, 8373, 8374
 8375, 8376, 8377, 8378, 8379, 8380, 8381, 8382, 8383, 8384, 8385,
8386, 8387, 8388, 8389, 8390
 8391, 8392, 8393, 8394, 8395, 8396, 8397, 8398, 8399, 8400, 8401,
8402, 8403, 8404, 8405, 8406
 8407, 8408, 8409, 8410, 8411, 8412, 8413, 8414, 8415, 8416, 8417,
8418, 8419, 8420, 8421, 8422
 8423, 8424, 8425, 9266, 9267, 9268, 9269, 9270, 9271, 9272, 9273,
9274, 9275, 9276, 9277, 9278
 9279, 9280, 9281, 9282, 9283, 9284, 9285, 9287, 9288, 9289, 9290,
9291, 9292, 9293, 9294, 9295
 9297, 9298, 9299, 9300, 9301, 9302, 9303, 9304, 9305, 9308, 9309,
9310, 9311, 9312, 9313, 9314
 9315, 9318, 9319, 9320, 9321, 9322, 9323, 9324, 9325, 9328, 9329,
9330, 9331, 9332, 9333, 9334
 9335, 9338, 9339, 9340, 9341, 9342, 9343, 9344, 9345, 9348, 9349,
9350, 9351, 9352, 9353, 9354
 9355, 9358, 9359, 9360, 9361, 9362, 9363, 9364, 9365, 9368, 9369,
9370, 9371, 9372, 9373, 9374
```

```
 9375, 9743
*Elset, elset=_PickedSet56, internal, instance="Part-2-mesh-2,5mm-1"
  9826,  9827,  9828,  9831,  9832,  9833,  9836,  9837,  9838,  9841,
9842,  9843,  9844,  9845,  9846,  9847
  9848,  9849,  9850,  9851,  9852,  9853,  9854,  9855,  9856,  9857,
9858,  9859,  9860,  9861,  9866,  9867
 11073, 11074, 11075, 11076, 11077, 11078, 11079, 11080, 11081, 11082,
11083, 11084, 11085, 11086, 11087, 11088
 11089, 11090, 11091, 11092, 11093, 11094, 11095, 11096, 11097, 11098,
11099, 11100, 11101, 11102, 11103, 11104
 11105, 11106, 11107, 11108, 11109, 11110, 11111, 11112, 11113, 11114,
11115, 11116, 11117, 11118, 11119, 11120
 11121, 11122, 11123, 11124, 11125, 11126, 11127, 11128, 11129, 11130,
11131, 11132, 11133, 11134, 11135, 11136
 11137, 11138, 11139, 11140, 11141, 11142, 11143, 11144, 11145, 11146,
11147, 11148, 11149, 11150, 11151, 11152
 11153, 11154, 11155, 11156, 11157, 11158, 11159, 11160, 11161, 11162,
11163, 11164, 11165, 11166, 11167, 11168
 11169, 11170, 11171, 11172, 11863, 11870, 11871, 11872, 11873, 11878,
11879, 11880, 11881, 11882, 11883, 11884
 11885, 11886, 11887, 11888, 11889, 11890, 11891, 11892, 11893, 11894,
11895, 11896, 11897, 11898, 11899, 11900
 11901, 11902, 11903, 11904, 11905, 11906, 11907, 11908, 11909, 11910,
11911, 11912, 11913, 11914, 11915, 11916
 11917, 11918, 11919, 11920, 11921, 11922, 11923, 11924, 11925, 11926,
11927, 11928, 11929, 11930, 11931, 11932
 11933, 11934, 11935, 11936, 11937, 11938, 11939, 11940, 11941, 11942,
11943, 11944, 11945, 11946, 11947, 11948
 11949, 11950, 11951, 11952, 11953, 11954, 11955, 11956, 11957, 11958,
11959, 11960, 11961, 11962, 11963, 11964
 11965, 11966, 11967, 11968, 11969, 11970, 11971, 11972, 11973, 11974,
11975, 11976, 11977, 11978, 11979, 11980
 11981, 11982, 11983, 11984, 11985, 11986, 11987, 11988, 11989, 11990,
11991, 11992, 11993, 11994, 11995, 11996
 11997, 11998, 11999, 12000, 12001, 12002, 12003, 12004, 12005, 12006,
12007, 12008, 12009, 12010, 12011, 12012
 12013, 12014, 12015, 12016, 12017, 12018, 12019, 12020, 12021, 12022,
12023, 12024, 12025, 12026, 12027, 12028
 12029, 12030, 12031, 12032, 12033, 12034, 12035, 12036, 12037, 12038,
12039, 12040, 12041, 12042, 12043
*Elset, elset=_PickedSet57, internal, instance="Part-2-mesh-2,5mm-1"
 6611, 6612, 6613, 6614, 6632, 6637, 6642, 6643, 6656, 6657, 6658,
6659, 6660, 6661, 6662, 6663
 6664, 6665, 6856, 6857, 6858, 6859, 6860, 6861, 6862, 6863, 6864,
6865, 6866, 6867, 6868, 6869
 6870, 6871, 6872, 6873, 6874, 6875, 6876, 6877, 6878, 6879, 6880,
6881, 6882, 6883, 6884
*Elset, elset=_PickedSet58, internal, instance="Part-2-mesh-2,5mm-1"
 1370, 1371, 1372, 1373, 1374, 1375, 1376, 1377, 1378, 1379, 1380,
1381, 1382, 1383, 1384, 1385
 1386, 1387, 1388, 1389, 1390, 1391, 1392, 1422, 1436, 1437, 1547,
1548, 1551, 1552, 1553, 1554
 1555, 1556, 1557, 1558, 1559, 1560, 1561, 1562, 1563, 1564, 1565,
1566, 1567, 1568, 1569, 1570
```

```
 1571, 1572, 1573, 1574, 1575, 2205, 2206, 2208, 2209, 2210, 2211,
2212, 2213, 2214, 2215, 2216
 2217, 2218, 2219, 2220, 2221, 2222, 2223, 2224, 2225, 2226, 2227,
2228, 2229, 2230, 2231, 2232
 2233, 2234, 2235, 2236, 2237, 2238, 2239, 2240, 2241, 2242, 2243,
2244, 2245, 2246, 2247, 2248
 2249, 2250, 2251, 2252, 2254, 2256
*Elset, elset=_PickedSet59, internal, instance="Part-2-mesh-2,5mm-1"
 8706, 8707, 8708, 8709, 8710, 8711, 8712, 8713, 8714, 8715, 8716,
8717, 8718, 8719, 8720, 8721
 8722, 8723, 8724, 8725, 8726, 8727, 8728, 8729, 8730, 8731, 8732,
8733, 8734, 8735, 8736, 8737
 8738, 8739, 8740, 8741, 8742, 8743, 8744, 8745, 8746, 8747, 8748,
8749, 8750, 8751, 8752, 8753
 8754, 8755, 8756, 8757, 8758, 8759, 8760, 8761, 8762, 8763, 8764,
8765, 8766, 8767, 8768, 8769
 8770, 8771, 8772, 8773, 8774, 8775, 8776, 8777, 8778, 8779, 8780,
8781, 8782, 8783, 8784, 8785
 8786, 8787, 8788, 8789, 8790, 8791, 8792, 8793, 8794, 8795, 8796,
8797, 8798, 8799, 8800, 8801
 8802, 8803, 8804, 8805, 8806, 8807, 8808, 8809, 8810, 8811, 8812,
8813, 8814, 8815, 8816, 8817
 8818, 8819, 8820, 8821, 8822, 8823, 8824, 8825, 8826, 8827, 8828,
8829, 8830, 8831, 8832, 8833
 8834, 8835, 8836, 8837, 8838, 8839, 8840, 8841, 8842, 8843, 8844,
8845, 8846, 8847, 8848, 8849
 8850, 8851, 8852, 8853, 8854, 8855, 8856, 8857, 8858, 8859, 8860,
8861, 8862, 8863, 8864, 8865
 8866, 8867, 8868, 8869, 8870, 8871, 8872, 8873, 8874, 8875, 8876,
8877, 8878, 8879, 8880, 8881
 8885, 8886, 8887, 8888, 8889, 8890, 8891, 8892, 8893, 8894, 8895,
8896, 8897, 8906, 8907, 8908
 8909, 8910, 8911, 8912, 8913, 8925, 8926, 8927, 8928, 8929, 8944,
8945, 9546, 9547, 9548, 9551
 9552, 9553, 9554, 9555, 9556, 9557, 9558, 9559, 9560, 9561, 9562,
9563, 9564, 9565, 9566, 9567
 9568, 9569, 9570, 9571, 9572, 9573, 9574, 9575, 9576, 9577, 9578,
9579, 9580
*Elset, elset=_PickedSet60, internal, instance="Part-2-mesh-2,5mm-1"
  9790,  9791,  9792,  9793, 10631, 10632, 10633, 10634, 10635, 10636,
10637, 10638, 10639, 10640, 10641, 10642
 10643, 10644, 10645, 10646, 10647, 10648, 10649, 10650, 10651, 10652,
10653, 10654, 10655, 10656, 10657, 10658
 10659, 10660, 10661, 10662, 10663, 10664, 10665, 10666, 10667, 10668,
10669, 10670, 10671, 10672, 10673, 10674
 10675, 10676, 10677, 10678, 10679, 10680, 10681, 10682, 10683, 10684,
10685, 10686, 10687, 10688, 10689, 10690
 10691, 10692, 10693, 10694, 10695, 10696, 10697, 10698, 10699, 10700,
10701, 10702, 10703, 10704, 10705, 10706
 10707, 10708, 10709, 10710, 10711, 10712, 10713, 10714, 10715, 10716,
10717, 10718, 10719, 10720, 10721, 10722
 10723, 10724, 10725, 10726, 10727, 10728, 10729, 10730, 10731, 10732,
10733, 10734, 10735, 10736, 10737, 10738
```

```
 10739, 10740, 10741, 10742, 10743, 10744, 10745, 10746, 10747, 10748,
10749, 10750, 10751, 10752, 10753, 10754
 10755, 10756, 10757, 10758, 10759, 10760, 10761, 10762, 10763, 10764,
10765, 10766, 10767, 10768, 10769, 10770
 10771, 10772, 10773, 10774, 10775, 10776, 10777, 10778, 10779, 10780,
10781, 10782, 10783, 10784, 10785, 10786
 10787, 10788, 10789, 10790, 10791, 10792, 10793, 10794, 10795, 10796,
10797, 10798, 10799, 10800, 10801, 10802
 10803, 10804, 10805, 10806, 10807, 10808, 10809, 10810, 10811, 10812,
10813, 10814, 10815, 10816, 10817, 10818
 10819, 10820, 10821, 10822, 10823, 10824, 10825, 10826, 10827, 10828,
10829, 10830, 10831, 10832, 10833, 10834
 10835, 10836, 10837, 10838, 10839, 10840, 10841, 10842, 10843, 10844,
10845, 10846, 10847, 10848, 10849, 10850
 10851, 10852, 10853, 10854, 10855, 10856, 10857, 10858, 10859, 10860,
10861, 10862, 10863, 10864, 10865, 10866
 10867, 10868, 10869, 10870, 10871, 10872, 10873, 10874, 10875, 10876,
10877, 10878, 10879, 10880, 10881, 10882
 10883, 10884, 10885, 10886, 10887, 10888, 10889, 10890, 10891, 10892,
10893, 10894, 10895, 10896, 10897, 10898
 10899, 10900, 10901, 10902, 10903, 10904, 10905, 10906, 10907, 10908,
10909, 10910, 10911, 10912, 10913, 10914
 10915, 10916, 10917, 10918, 10919, 10920, 10921, 10922, 10923, 10924,
10925, 10926, 10927, 10928, 10929, 10930
 10931, 10932, 10933, 10934, 10935, 10936, 10937, 10938, 10939, 10940,
10941, 10942, 10943, 10944, 10945, 10946
 10947, 10948, 10949, 10950, 10951, 10952, 10953, 10954, 10955, 10956,
10957, 10958, 10959, 10960, 10961, 10962
 10963, 10964, 10965, 10966, 10967, 10968
*Elset, elset=_PickedSet61, internal, instance="Part-2-mesh-2,5mm-1"
 7207, 7208, 7209, 7210, 7211, 7212, 7213, 7214, 7215, 7216, 7217,
7218, 7219, 7220, 7221, 7222
 7367, 7368, 7369, 7370, 7845, 7846, 7847, 7848, 7854, 7855, 7856,
7857, 7863, 7864, 7865, 7866
 7872, 7873, 7874, 7875, 7881, 7882, 7883, 7884, 7890, 7891, 7892,
7893, 7899, 7900, 7901, 7902
 7903, 7904, 7905, 7906, 7907, 7908, 7909, 7910, 7912, 8017, 8018,
8019, 8020, 8021, 8022, 8023
 8024, 8025, 8028, 8029, 8030, 8031, 8032, 8033, 8034, 8035, 8039,
8040, 8041, 8042, 8043, 8044
 8045, 8046, 8050, 8051, 8052, 8053, 8054, 8055, 8056, 8057, 8061,
8062, 8063, 8064, 8065, 8066
 8067, 8072, 8073, 8074, 8075, 8076, 8077, 8078, 8083, 8084, 8085,
8086, 8087, 8088, 8089, 8227
 8228, 8229, 8230, 8231, 8232, 8233, 8234, 8235, 8238, 8239, 8240,
8241, 8242, 8243, 8244, 8245
 8246, 8250, 8251, 8252, 8253, 8254, 8255, 8256, 8257, 8261, 8262,
8263, 8264, 8265, 8266, 8267
 8268, 8272, 8273, 8274, 8275, 8276, 8277, 8278, 8279, 8284, 8285,
8286, 8287, 8288, 8289, 8290
 8295, 8296, 8297, 8298, 8299, 8300, 8301
*Enrichment, name=Crack-4, type=PROPAGATION CRACK, elset=_PickedSet53
*Enrichment, name=Crack-7, type=PROPAGATION CRACK, elset=_PickedSet54
*Enrichment, name=Crack-8, type=PROPAGATION CRACK, elset=_PickedSet55
```

```
*Enrichment, name=Crack-11, type=PROPAGATION CRACK, elset=_PickedSet56
*Enrichment, name=Crack-18, type=PROPAGATION CRACK, elset=_PickedSet57
*Enrichment, name=Crack-19, type=PROPAGATION CRACK, elset=_PickedSet58
*Enrichment, name=Crack-22, type=PROPAGATION CRACK, elset=_PickedSet59
*Enrichment, name=Crack-24, type=PROPAGATION CRACK, elset=_PickedSet60
*Enrichment, name=Crack-25, type=PROPAGATION CRACK, elset=_PickedSet61
*End Assembly
**
** MATERIALS
**
*Material, name=Material-1
*Damage Initiation, criterion=MAXPE, position=COMBINED, tolerance=0.5
 0.38,
*Damage Evolution, type=ENERGY
 1e-07,
*Damage Stabilization
1e-06
*Elastic
2000., 0.3
*Plastic
80.,   0.
83., 0.34
** ----------------------------------------------------------------
**
** STEP: Step-1
**
*Step, name=Step-1, nlgeom=YES, inc=1000000
*Static, stabilize=2e-05, allsdtol=0.005, continue=NO
0.01, 1., 1e-50, 0.1
**
** BOUNDARY CONDITIONS
**
** Name: BC-1 Type: Displacement/Rotation
*Boundary
Set-3, 1, 1, 1.
Set-3, 2, 2
Set-3, 6, 6
** Name: BC-2 Type: Displacement/Rotation
*Boundary
Set-4, 1, 1
Set-4, 2, 2
Set-4, 6, 6
**
** CONTROLS
**
*Controls, reset
*Controls, parameters=time incrementation
16, 20, , , , , , 50, , ,
**
** OUTPUT REQUESTS
**
*Restart, write, frequency=0
**
** FIELD OUTPUT: F-Output-1
```

```
**
*Output, field
*Node Output
CF, PHILSM, PSILSM, RF, U
*Element Output, directions=YES
LE, PE, PEEQ, PEMAG, S, STATUSXFEM
*Contact Output
CDISP, CSTRESS
**
** HISTORY OUTPUT: H-Output-2
**
*Output, history
*Node Output, nset=Set-3
U1, U2, U3
**
** HISTORY OUTPUT: H-Output-3
**
*Node Output, nset=Set-4
RF1, RF2, RF3
**
** HISTORY OUTPUT: H-Output-1
**
*Output, history, variable=PRESELECT
*End Step
```

Appendix B: User subroutine UDMGINI code

The user defined subroutine UDMGINI code utilized in this study has been provided in the following:

```
       SUBROUTINE UDMGINI(FINDEX,NFINDEX,FNORMAL,NDI,NSHR,NTENS,PROPS,
      1 NPROPS,STATEV,NSTATEV,STRESS,STRAIN,STRAINEE,LXFEM,TIME,
      2 DTIME,TEMP,DTEMP,PREDEF,DPRED,NFIELD,COORDS,NOEL,NPT,
      3 KLAYER,KSPT,KSTEP,INC,KDIRCYC,KCYCLELCF,TIMECYC,SSE,SPD,
      4 SCD,SVD,SMD,JMAC,JMATYP,MATLAYO,LACCFLA,CELENT,DROT,ORI)
C
       INCLUDE 'ABA_PARAM.INC'
CC
       DIMENSION FINDEX(NFINDEX),FNORMAL(NDI,NFINDEX),COORDS(*),
      1 STRESS(NTENS),STRAIN(NTENS),STRAINEE(NTENS),PROPS(NPROPS),
      2 STATEV(NSTATEV),PREDEF(NFIELD),DPRED(NFIELD),TIME(2),
      3 JMAC(*),JMATYP(*),DROR(3,3),ORI(3,3)

       DIMENSION PE(3), ANPE(3,3), E(6)
       PE(1)=0.0
       PE(2)=0.0
       PE(3)=0.0
C
C ROTATE THE STRAIN TO GLOBAL SYSTEM IF THERE IS ORIENTATION
C
       CALL ROTSIG(STRAIN,ORI,E,2,NDI,NSHR)
       CALL SPRIND(E,PE,ANPE,2,NDI,NSHR)
       EPS1 = PE(1)
      EPS2 = PE(1)
       KMAX = 1
      KMIN = 1
      EPSABS = 0
       DO K1 = 2, NDI
          IF(PE(K1).GE.EPS1) THEN
             EPS1 = PE(K1)
             KMAX = K1
          ELSE IF(PE(K1).LT.EPS2) THEN
                  EPS2 = PE(K1)
                  KMIN = K1
          END IF
       END DO
      EPSABS = (-1)*EPS2
       IF(EPS1.LT.EPSABS) THEN
          FINDEX(2) = EPS2/PROPS(2)
       ELSE
         FINDEX(1) = EPS1/PROPS(1)
      END IF
       IF(EPS1.LT.EPSABS) THEN
          DO K1 = 1, NDI
             FNORMAL(K1,2) = ANPE(KMIN,K1)
          END DO
```

```
ELSE
   DO K1 = 1, NDI
   FNORMAL(K1,1) = ANPE(KMAX,K1)
   END DO
END IF
RETURN
END
```

Appendix C: Input file of failure modeling in 3D Cancellous Bone specimen using XFEM

A piece of input file of failure modeling in 3D Cancellous Bone specimen using XFEM:

```
*Heading
** Job name: Job-2 Model name: Job6
** Generated by: Abaqus/CAE 2017
*Preprint, echo=NO, model=NO, history=NO, contact=NO
**
** PARTS
**
*Part, name=PART-1
*Node
      1,  0.550000012,  0.508301973,     1.063797
      2,  0.550000012,  0.511321425,   1.08241236
      3,  0.550000012,  0.515941501,   1.37498844
      4,  0.550000012,  0.521607399,   1.23360991
      5,  0.550000012,  0.526500404,   1.19675064
      6,  0.550000012,  0.526548266,   1.31339109
      7,  0.550000012,  0.526881099,   1.27236247
      8,  0.550000012,  0.527424097,   1.10947692
      9,  0.550000012,  0.533798397,   1.42357171
     10,  0.550000012,  0.533815801,   1.08557844
     11,  0.550000012,    0.5342803,    1.1341058
     12,  0.550000012,  0.540143669,   1.34942102
     13,  0.550000012,  0.541185915,   1.16875291
     14,  0.550000012,  0.541900218,   1.39375961
     15,  0.550000012,  0.550782621,   1.06923532
     16,  0.550000012,  0.551912785,   1.23334193
     17,  0.550000012,  0.556919217,   1.30162776
     18,  0.550000012,  0.564598799,   1.20207274
     19,  0.550000012,  0.565680325,   1.26152349
     20,  0.550000012,  0.574441433,   1.37208152
     21,  0.550000012,  0.579189003,   1.41461217
     22,  0.550000012,     0.584454,   1.32872534
     23,  0.550000012,  0.594299316,   1.23796475
     24,  0.550000012,  0.594466686,   1.28536928
     25,  0.550000012,  0.612301826,   1.38779819
     26,  0.550000012,  0.616995156,   1.35040343
     27,  0.550000012,  0.622524917,   1.21853137
     28,  0.550000012,  0.624504685,   1.25935543
     29,  0.550000012,  0.627007902,   1.30704725
     30,  0.550000012,  0.647033334,   1.40243089
     31,  0.550000012,  0.650326908,    1.2369858
     32,  0.550000012,  0.654542804,   1.36341035
     33,  0.550000012,  0.655081749,   2.56148243
     34,  0.550000012,  0.659236193,   1.32601571
     35,  0.550000012,  0.659549057,   1.27669799
     36,  0.550000012,  0.670629859,   2.58834696
     37,  0.550000012,  0.674067497,   1.23074043
     38,  0.550000012,  0.683561385,   1.19039249
```

```
      39,  0.550000012,   0.68508321,   2.53493261
      40,  0.550000012,  0.687396884,   1.39104998
      41,  0.550000012,  0.692090273,   1.29837608
      42,  0.550000012,  0.692090273,   1.34715188
      43,  0.550000012,  0.699563503,   2.56517315
      44,  0.550000012,  0.702415884,   1.25772977
      45,  0.550000012,  0.704475105,   2.59370565
      46,  0.550000012,  0.704606056,   1.22033501
      47,  0.550000012,  0.711470187,   1.18301523
      48,  0.550000012,  0.722128391,   1.37641728
      49,  0.550000012,  0.722128391,   2.54183102
      50,  0.550000012,  0.725883126,   1.33089316
      51,  0.550000012,  0.731222272,   2.57579017
      52,  0.550000012,  0.732141018,   1.28103352
      53,  0.550000012,   0.73392874,   1.41448617
      54,  0.550000012,  0.735895813,   1.21816719
      55,  0.550000012,  0.744924664,   1.18177223
      56,  0.550000012,   0.75216639,   1.24634874
      57,  0.550000012,  0.752999306,   1.14547777
      58,  0.550000012,  0.761553288,   1.30487955
      59,  0.550000012,  0.762179077,   1.37641728
      60,  0.550000012,  0.771878779,   1.33902252
.
.
.
.
.
  22477,   1.02799845,    1.9587189,   2.59798217
  22478,   2.09818792,   1.68684053,   2.76523662
  22479,  0.842361152,   1.46664584,   2.16614556
  22480,   2.06427336,   1.58932364,   2.34574103
  22481,  0.581149042,  0.715667307,   2.53802276
  22482,   2.01109433,     1.613626,   2.30430174
  22483,   1.99393296,   1.97524786,   2.74292111
  22484,   1.26115561,   2.19182372,   2.11326909
  22485,  0.674788475,   1.70322561,   2.20922232
  22486,  0.762059093,  0.708972812,   2.57470369
  22487,   1.50344729,  0.582755983,   2.15535855
  22488,   2.24365187,   1.79963696,   1.07921267
  22489,   1.37145591,  0.769375265,   2.22563291
  22490,   1.01669753,   1.38236046,   2.51585436
  22491,   1.06148708,   1.82118225,   1.39299536
  22492,  0.814122081,  0.634509504,   2.01582003
  22493,   1.02733672,   1.77748513,   1.07861471
  22494,   1.98705316,   1.05367446,   1.70388567
  22495,   2.26180983,   1.24222398,   2.11876988
  22496,   1.06921208,   1.98457158,   2.25538087
  22497,   2.27046967,  0.571690619,   1.68206251
  22498,  0.751012146,   2.19309211,   1.79567659
  22499,   2.27148247,  0.625325382,   1.76212132
  22500,   2.00764704,   1.02609897,   1.13275051
  22501,   1.23711383,  0.793396413,   1.41538668
  22502,   1.83621264,  0.519468069,   1.08045065
  22503,   1.48956788,   0.52724874,   1.90750504
```

```
  22504,   1.58921421,    1.9751184,   2.24117279
  22505,   2.25807762,   1.26615512,    2.3715601
  22506,  0.856917143,  0.557284951,    2.5398469
  22507,   1.84950674,    1.1744734,   2.18177915
  22508,  0.620485127,   2.00977468,   1.07866836
  22509,   1.70977974,   1.32131279,   2.32947373
  22510,    1.8829999,  0.776603281,   1.94662285
  22511,  0.703161836,   1.02284074,   2.70184779
  22512,   1.40074515,  0.784251451,   2.29308796
  22513,   1.24433231,   2.15227461,   2.06890702
  22514,  0.885693848,    1.2912991,   2.06284952
  22515,    2.1796422,   1.98545313,   2.71681905
  22516,  0.939723313,    1.2642014,   2.08413577
  22517,    1.9000113,   1.96992493,   2.16779399
  22518,   1.53332031,   1.45282257,   2.71418691
  22519,   1.87502742,   2.02320528,   2.13879633
  22520,   2.04791093,   1.88819671,   2.13596511
  22521,   1.78895879,   2.11640644,   1.39854896
  22522,   2.07356429,   1.65593541,   2.64598274
  22523,   0.91733098,    1.3462404,   2.05715203
  22524,   1.75451088,   1.24620271,   2.21797276
  22525,  0.927335382,   1.12999463,   2.07578826
  22526,  0.706632972,  0.747108042,   2.03584838
  22527,   1.83240056,    2.0142169,   1.11648333
  22528,    1.7891165,    2.0517292,   1.22943819
  22529,    1.2294966,   2.17378139,   1.40477455
  22530,   1.94861448,   1.93584716,   2.17735052
  22531,   2.04323459,   1.86577737,   2.68365574
  22532,   1.80784833,   2.05417037,   1.28067017
  22533,  0.839983284,  0.616059721,   1.69283772
  22534,   1.22086596,   2.08236885,    1.3940469
  22535,  0.859092295,   1.27420855,   2.73663521
  22536,   1.96094227,   1.31021476,   2.11882496
  22537,    2.0379858,  0.882332087,   2.75820327
  22538,   1.95439112,   1.92656815,    2.0345819
  22539,   1.96752274,   1.90411472,   2.10286474
  22540,   2.25377488,  0.670993507,   1.81665874
  22541,   1.34448981,   0.84398973,   2.37610674
  22542,   1.99776423,   1.88596237,   2.04049015
  22543,   1.82260346,  0.870767772,   1.72121572
  22544,   2.00759673,     1.119555,   1.67909265
  22545,   1.79951942,   1.22751486,   2.20683265
  22546,   2.12349463,   1.66382492,   2.66834068
  22547,    1.8024931,   2.04968095,    1.1888119
  22548,   1.90084434,   1.93825877,   2.12264347
  22549,   2.05245519,  0.860283375,   2.71751928
  22550,  0.888634324,  0.653402925,   2.54687762
  22551,  0.662032247,   2.22106767,   1.19756663
  22552,   0.55773133,    2.1368556,   2.74986124
*Element, type=C3D4
 34437, 15779, 16042, 15739, 16278
 34438, 16042, 16087, 15739, 16278
 34439, 16125, 16042, 15779, 16278
 34440, 16281, 16125, 15779, 16278
```

```
 34441, 15645, 15976, 15795, 16304
 34442, 16050, 15976, 15645, 16304
 34443, 15846, 16294, 16279, 15817
 34444, 16309, 15798, 15743, 16291
 34445,  4438,  4775,  4493,  4585
 34446, 15798, 15866, 15743, 16291
 34447, 15792, 15743, 15866, 16291
 34448, 16295, 15866, 15798, 16291
 34449, 16309, 16295, 15798, 16291
 34450, 15846, 15792, 15866, 16291
 34451, 15672, 16298, 15585, 16288
 34452, 15969, 15672, 16288, 16286
 34453, 15846, 16294, 16291, 16279
 34454,   945,   865, 20967,     2
 34455, 15634, 16309, 15743, 16310
 34456, 15303, 15585, 15392, 16306
 34457,  4812,  4556,  4438,  4775
 34458, 15792, 15817, 15660, 16294
 34459,  5728,  5499,  5770,  5429
 34460, 15660, 15779, 15585, 16299
 34461, 15585, 16298, 15392, 16306
 34462, 16298, 16311, 15392, 16306
 34463, 15585, 16314, 15303, 15660
 34464, 16418, 15572, 15505, 16413
 34465, 16306, 16299, 15585, 16288
 34466, 15634, 15743, 15543, 16310
 34467, 15817, 16279, 16112, 16281
 34468, 19441, 19440,  6876,  7131
 34469, 16295, 16132, 15866, 16291
 34470, 15739, 16278, 16087, 16288
 34471, 16125, 15817, 16112, 16281
 34472, 16064, 16315, 15795, 16304
 34473, 16299, 16281, 15779, 16278
 34474, 15543, 15660, 15299, 16314
 34475, 16330, 16335, 15634, 16322
 34476, 16314, 15543, 15660, 16310
 34477, 19640,  7730,  7483,  7835
 34478, 16050, 15645, 15873, 16307
 34479, 16315, 15695, 15795, 15443
 34480, 15645, 15795, 15443, 16315
 34481, 15739, 16087, 15969, 16288
 34482, 15299, 15660, 15303, 16314
 34483, 15660, 16281, 16294, 15817
 34484, 16289, 15672, 15916, 16286
 34485, 15672, 16117, 15916, 16286
.
.
.
.
112026, 112027, 112028, 112029, 112030, 112031, 112033, 112034, 112036,
112037, 112038, 112039, 112040, 112041, 112042, 112043
 112044, 112045, 112046, 112047, 112048, 112049, 112050, 112051,
112052, 112053, 112054, 112055, 112056, 112057, 112058, 112060
```

112061, 112062, 112063, 112064, 112065, 112066, 112067, 112068,
112070, 112072, 112073, 112076, 112077, 112078, 112079, 112080
112083, 112084, 112088, 112089, 112090, 112091, 112092, 112095,
112096, 112097, 112098, 112099, 112100, 112101, 112102, 112104
112106, 112107, 112109, 112110, 112111, 112112, 112113, 112114,
112115, 112116, 112117, 112119, 112120, 112121, 112122, 112123
112124, 112125, 112126, 112128, 112129, 112130, 112131, 112132,
112133, 112134, 112135, 112136, 112137, 112138, 112139, 112140
112141, 112142, 112144, 112145, 112146, 112147, 112148, 112149,
112151, 112152, 112153, 112156, 112157, 112158, 112159, 112160
112161, 112163, 112165, 112170, 112171, 112172, 112174, 112175,
112176, 112178, 112179, 112181, 112182, 112183, 112184, 112185
112186, 112187, 112188, 112189, 112190, 112191, 112192, 112193,
112195, 112196, 112198, 112199, 112200, 112201, 112202, 112203
112204, 112206, 112208, 112211, 112212, 112214, 112215, 112216,
112217, 112221, 112224, 112228, 112231, 112232, 112238, 112239
112240, 112241, 112242, 112243, 112244, 112245, 112246, 112247,
112251, 112252, 112253, 112254, 112255, 112256, 112257, 112259
112260, 112261, 112262, 112263, 112264, 112265, 112266, 112267,
112268, 112269, 112273, 112274, 112275, 112276, 112277, 112278
112279, 112280, 112281, 112282, 112283, 112284, 112285, 112286,
112288, 112289, 112290, 112291, 112293, 112294, 112295, 112296
112297, 112298, 112300, 112302, 112303, 112304, 112305, 112306,
112307, 112308, 112309, 112310, 112312, 112313, 112314, 112316
112317, 112318, 112319, 112320, 112321, 112322, 112323, 112324,
112325, 112326, 112327, 112328, 112329, 112330, 112331, 112332
112333, 112334, 112335, 112336, 112337, 112338, 112340, 112341,
112342, 112344, 112346, 112347, 112348, 112350, 112352, 112353
112354, 112355, 112357, 112360, 112361, 112362, 112363, 112364,
112365, 112366, 112368, 112369, 112370, 112371, 112372, 112373
112377, 112378, 112381, 112382, 112383, 112384, 112385, 112386,
112387, 112388, 112389, 112390, 112391, 112392, 112393, 112394
112395, 112396, 112397, 112398, 112401, 112402, 112403, 112404,
112405, 112407, 112410, 112411, 112412, 112413, 112414, 112415
112416, 112417, 112418, 112419, 112421, 112422, 112424, 112425,
112426, 112427, 112428, 112429, 112430, 112431, 112432, 112433
112434, 112435, 112436, 112437, 112438, 112439, 112440, 112441,
112442, 112443, 112444, 112445, 112446, 112447, 112448, 112449
112450, 112451, 112452, 112453, 112454, 112455, 112456, 112457,
112458, 112460, 112461, 112462, 112463, 112464, 112465, 112466
112467, 112469, 112470, 112471, 112472, 112473, 112474, 112475,
112476, 112477, 112478, 112479, 112481, 112482, 112483, 112484
112485, 112486, 112487, 112488, 112489, 112490, 112491, 112492,
112493, 112494, 112495, 112496, 112497, 112498, 112499, 112500
112501, 112502, 112504, 112505, 112506, 112507, 112508, 112509,
112510, 112511, 112512, 112513, 112514, 112515, 112516, 112517
112518, 112519, 112521, 112522, 112523, 112524, 112526, 112527,
112528, 112529, 112530, 112531, 112533, 112534, 112535, 112537
112538, 112539, 112540, 112541, 112542, 112543, 112544, 112545,
112547, 112548, 112549, 112550, 112551, 112552, 112553, 112554
112555, 112556, 112558, 112559, 112561, 112563, 112565, 112566,
112567, 112568, 112569, 112570, 112571, 112572, 112573, 112574
112575, 112576, 112577, 112578, 112579, 112580, 112581, 112582,
112583, 112584, 112585, 112586, 112587, 112588, 112589, 112590

112591, 112592, 112593, 112594, 112595, 112596, 112597, 112598,
112599, 112600, 112601, 112602, 112603, 112604, 112605, 112606
112607, 112608, 112609, 112610, 112611, 112612, 112613, 112614,
112615, 112616, 112617, 112619, 112620, 112621, 112622, 112623
112624, 112625, 112626, 112627, 112628, 112629, 112630, 112631,
112632, 112633, 112634, 112635, 112636, 112637, 112638, 112640
112641, 112643, 112644, 112645, 112646, 112647, 112648, 112649,
112650, 112651, 112652, 112653, 112654, 112656, 112657, 112658
112659, 112660, 112661, 112662, 112663, 112664, 112665, 112666,
112667, 112668, 112670, 112671, 112672, 112673, 112674, 112675
112677, 112678, 112679, 112680, 112682, 112683, 112684, 112685,
112686, 112687, 112688, 112689, 112690, 112691, 112692, 112693
112694, 112695, 112697, 112698, 112700, 112701, 112702, 112703,
112704, 112705, 112706, 112707, 112708, 112709, 112710, 112711
112712, 112713, 112714, 112715, 112716, 112718, 112719, 112720,
112721, 112722, 112723, 112724, 112725, 112728, 112729, 112731
112732, 112734, 112735, 112736, 112737, 112738, 112739, 112740,
112741, 112743, 112744, 112745, 112747, 112748, 112749, 112750
112751, 112752, 112753, 112754, 112755, 112756, 112757, 112758,
112759, 112760, 112761, 112762, 112763, 112764, 112765, 112766
112767, 112768, 112769, 112770, 112771, 112772, 112773, 112774,
112775, 112776, 112777, 112778, 112779, 112780, 112781, 112782
112783, 112784, 112785, 112786, 112787, 112788, 112789, 112791,
112792, 112793, 112795, 112797, 112798, 112799, 112800, 112801
112803, 112804, 112805, 112806, 112807, 112808, 112809, 112811,
112813, 112814, 112815, 112816, 112817, 112818, 112819, 112820
112821, 112822, 112823, 112824, 112825, 112827, 112828, 112829,
112830, 112831, 112832, 112833, 112834, 112835, 112836, 112837
112838, 112839, 112840, 112841, 112843, 112844, 112846, 112847,
112850, 112851, 112852, 112853, 112854, 112855, 112856, 112857
112858, 112859, 112860, 112862, 112863, 112864, 112865, 112866,
112867, 112868, 112869, 112870, 112871, 112872, 112873, 112874
112875, 112876, 112877, 112878, 112879, 112880, 112881, 112882,
112883, 112884, 112890, 112891, 112892, 112893, 112895, 112897
112898, 112904, 112908, 112909, 112910, 112911, 112912, 112913,
112914, 112915, 112916, 112918, 112919, 112920, 112921, 112922
112923, 112925, 112926, 112927, 112928, 112929, 112931, 112932,
112933, 112934, 112935, 112936, 112937, 112938, 112940, 112941
112942, 112944, 112945, 112946, 112947, 112948, 112949, 112950,
112951, 112952, 112953, 112954, 112957, 112958, 112959, 112961
112962, 112963, 112964, 112965, 112966, 112967, 112968, 112969,
112970, 112971, 112972, 112974, 112978, 112979, 112982, 112983
112984, 112985, 112986, 112987, 112989, 112990, 112991, 112992,
112993, 112994, 112995, 112997, 113001, 113002, 113004, 113006
113007, 113008, 113009, 113010, 113011, 113013, 113014, 113016,
113017, 113018, 113019, 113022, 113023, 113025, 113026, 113027
113028, 113029, 113030, 113031, 113032, 113033, 113034, 113037,
113038, 113039, 113040, 113041, 113042, 113043, 113044, 113045
113046, 113047, 113048, 113049, 113050, 113051, 113052, 113053,
113054, 113055, 113056, 113057, 113059, 113060, 113062, 113063
113064, 113065, 113066, 113067, 113068, 113069, 113070, 113071,
113073, 113074, 113077, 113080, 113081, 113082, 113083, 113084
113085, 113086, 113087, 113089, 113091, 113092, 113093, 113094,
113095, 113096, 113097, 113098, 113099, 113100, 113101, 113102

113103, 113104, 113106, 113107, 113108, 113110, 113111, 113112,
113116, 113117, 113118, 113120, 113121, 113122, 113124, 113126
113127, 113128, 113130, 113131, 113133, 113134, 113135, 113136,
113137, 113138, 113139, 113140, 113141, 113142, 113144, 113145
113146, 113147, 113148, 113149, 113151, 113152, 113153, 113155,
113156, 113157, 113158, 113159, 113160, 113162, 113163, 113164
113165, 113166, 113167, 113168, 113170, 113171, 113172, 113173,
113174, 113175, 113176, 113177, 113178, 113179, 113180, 113181
113182, 113183, 113185, 113186, 113187, 113188, 113189, 113190,
113191, 113192, 113194, 113195, 113196, 113197, 113198, 113199
113200, 113201, 113202, 113203, 113204, 113205, 113207, 113208,
113209, 113210, 113211, 113212, 113215, 113216, 113217, 113218
113221, 113222, 113223, 113224, 113226, 113227, 113228, 113229,
113230, 113233, 113235, 113236, 113239, 113240, 113242, 113244
113246, 113248, 113249, 113250, 113251, 113252, 113253, 113254,
113255, 113257, 113258, 113259, 113260, 113261, 113262, 113263
113264, 113265, 113267, 113268, 113270, 113273, 113274, 113275,
113276, 113277, 113278, 113280, 113281, 113282, 113283, 113284
113285, 113286, 113287, 113288, 113289, 113290, 113291, 113292,
113293, 113294, 113295, 113296, 113297, 113298, 113300, 113301
113302, 113303, 113304, 113306, 113307, 113308, 113309, 113310,
113312, 113313, 113314, 113315, 113316, 113317, 113319, 113320
113322, 113323, 113324, 113325, 113326, 113327, 113329, 113331,
113333, 113334, 113335, 113337, 113338, 113341, 113342, 113343
113344, 113345, 113347, 113348, 113349, 113350, 113352, 113353,
113354, 113355, 113356, 113357, 113358, 113359, 113360, 113361
113365, 113367, 113371, 113372, 113373, 113374, 113375, 113376,
113377, 113378, 113379, 113380, 113381, 113382, 113383, 113384
113385, 113386, 113388, 113389, 113390, 113391, 113392, 113393,
113394, 113396, 113397, 113398, 113399, 113400, 113402, 113403
113404, 113405, 113406, 113407, 113408, 113409, 113411, 113412,
113414, 113415, 113416, 113417, 113418, 113419, 113420, 113421
113422, 113423, 113424, 113425, 113426, 113427, 113428, 113429,
113431, 113432, 113435, 113436, 113437, 113439, 113440, 113443
113444, 113445, 113446, 113447, 113448, 113449, 113450, 113451,
113452, 113453, 113454, 113455, 113456, 113457, 113458, 113459
113460, 113461, 113464, 113465, 113466, 113468, 113469, 113470,
113474, 113475, 113476, 113477, 113478, 113479, 113480, 113482
113483, 113484, 113485, 113486, 113487, 113488, 113489, 113490,
113493, 113496, 113498, 113499, 113502, 113503, 113505, 113506
113508, 113509, 113510, 113511, 113512, 113514, 113515, 113518,
113521, 113522, 113524, 113525, 113526, 113527, 113529, 113530
113531, 113532, 113533, 113535, 113538, 113539, 113541, 113544,
113545, 113547, 113548, 113549, 113550, 113551, 113552, 113554
113556, 113557, 113563, 113564, 113565, 113566, 113567, 113568,
113570, 113571, 113572, 113573, 113574, 113575, 113576, 113577
113578, 113579, 113580, 113582, 113583, 113586, 113587, 113588,
113589, 113590, 113591, 113593, 113594, 113595, 113596, 113603
113604, 113605, 113608, 113609, 113610, 113612, 113613, 113614,
113616, 113618, 113621, 113623, 113625, 113627, 113628, 113632
113634, 113635, 113636, 113637, 113638, 113639, 113640, 113641,
113643, 113645, 113646, 113648, 113650, 113651, 113653, 113654
113655, 113656, 113658, 113659, 113660, 113661, 113663, 113664,
113668, 113669, 113672, 113673, 113675, 113676, 113677, 113679

```
 113681, 113682, 113683, 113684, 113685, 113686, 113687, 113688,
113689, 113690, 113691, 113692, 113693, 113695, 113697, 113698
 113700, 113701, 113702, 113704, 113705, 113706, 113707, 113708,
113713, 113717, 113718, 113719, 113722, 113723, 113724, 113725
 113727,
*Enrichment, name=CRACK-1, type=PROPAGATION CRACK, elset=SET-3
*Enrichment, name=CRACK-2, type=PROPAGATION CRACK, elset=SET-4
*Enrichment, name=CRACK-3, type=PROPAGATION CRACK, elset=SET-5
*Enrichment, name=CRACK-4, type=PROPAGATION CRACK, elset=SET-6
*Enrichment, name=CRACK-5, type=PROPAGATION CRACK, elset=SET-7
*Enrichment, name=CRACK-6, type=PROPAGATION CRACK, elset=SET-8
*Enrichment, name=CRACK-7, type=PROPAGATION CRACK, elset=SET-9
*Enrichment, name=CRACK-8, type=PROPAGATION CRACK, elset=SET-10
*Enrichment, name=CRACK-9, type=PROPAGATION CRACK, elset=SET-11
*Enrichment, name=CRACK-10, type=PROPAGATION CRACK, elset=SET-12
*Enrichment, name=CRACK-11, type=PROPAGATION CRACK, elset=SET-13
*Enrichment, name=CRACK-12, type=PROPAGATION CRACK, elset=SET-14
*Enrichment, name=CRACK-13, type=PROPAGATION CRACK, elset=SET-15
*Enrichment, name=CRACK-14, type=PROPAGATION CRACK, elset=SET-16
*Enrichment, name=CRACK-15, type=PROPAGATION CRACK, elset=SET-17
*Enrichment, name=CRACK-16, type=PROPAGATION CRACK, elset=SET-18
*Enrichment, name=CRACK-17, type=PROPAGATION CRACK, elset=SET-19
*Enrichment, name=CRACK-18, type=PROPAGATION CRACK, elset=SET-20
*Enrichment, name=CRACK-19, type=PROPAGATION CRACK, elset=SET-21
*Enrichment, name=CRACK-20, type=PROPAGATION CRACK, elset=SET-22
*End Assembly
**
** MATERIALS
**
*Material, name=MATERIAL-1
*Damage Initiation, criterion=MAXPE, tolerance=0.6
 0.38,
*Damage Evolution, type=ENERGY
 0.0001,
*Damage Stabilization
1e-05
*Elastic
4100., 0.3
*Plastic
 166.5,   0.
 172.5, 0.34
**
** BOUNDARY CONDITIONS
**
** Name: Disp-BC-1 Type: Symmetry/Antisymmetry/Encastre
*Boundary
SET-2, ENCASTRE
** Name: Disp-BC-2 Type: Displacement/Rotation
*Boundary
SET-1, 1, 1
** Name: Disp-BC-3 Type: Displacement/Rotation
*Boundary
SET-1, 2, 2
** Name: Disp-BC-4 Type: Displacement/Rotation
```

```
*Boundary
SET-1, 3, 3
** Name: Disp-BC-5 Type: Displacement/Rotation
*Boundary
SET-1, 4, 4
** Name: Disp-BC-6 Type: Displacement/Rotation
*Boundary
SET-1, 5, 5
** Name: Disp-BC-7 Type: Displacement/Rotation
*Boundary
SET-1, 6, 6
** ----------------------------------------------------------------
**
** STEP: Step-1
**
*Step, name=Step-1, nlgeom=YES, inc=1000000
*Static, stabilize=0.0002, allsdtol=0.05, continue=NO
0.01, 1., 1e-50, 0.1
**
** BOUNDARY CONDITIONS
**
** Name: Disp-BC-1 Type: Symmetry/Antisymmetry/Encastre
*Boundary, op=NEW
** Name: Disp-BC-2 Type: Displacement/Rotation
*Boundary, op=NEW
** Name: Disp-BC-3 Type: Displacement/Rotation
*Boundary, op=NEW
** Name: Disp-BC-4 Type: Displacement/Rotation
*Boundary, op=NEW
** Name: Disp-BC-5 Type: Displacement/Rotation
*Boundary, op=NEW
** Name: Disp-BC-6 Type: Displacement/Rotation
*Boundary, op=NEW
** Name: Disp-BC-7 Type: Displacement/Rotation
*Boundary, op=NEW
** Name: Disp-BC-8 Type: Symmetry/Antisymmetry/Encastre
*Boundary, op=NEW
SET-2, ENCASTRE
** Name: Disp-BC-9 Type: Displacement/Rotation
*Boundary, op=NEW
SET-1, 1, 1, 1.
** Name: Disp-BC-10 Type: Displacement/Rotation
*Boundary, op=NEW
SET-1, 3, 3
** Name: Disp-BC-11 Type: Displacement/Rotation
*Boundary, op=NEW
SET-1, 4, 4
** Name: Disp-BC-12 Type: Displacement/Rotation
*Boundary, op=NEW
SET-1, 5, 5
** Name: Disp-BC-13 Type: Displacement/Rotation
*Boundary, op=NEW
SET-1, 6, 6
** Name: Disp-BC-14 Type: Displacement/Rotation
```

```
*Boundary, op=NEW
SET-1, 2, 2
**
** CONTROLS
**
*Controls, reset
*Controls, analysis=discontinuous
*Controls, parameters=time incrementation
, , , , , , , 100, , ,
**
** OUTPUT REQUESTS
**
*Restart, write, frequency=0
**
** FIELD OUTPUT: F-Output-1
**
*Output, field
*Contact Output
CDISP, CSTRESS
**
** FIELD OUTPUT: F-Output-2
**
*Node Output
CF, PHILSM, PSILSM, RF, U
**
** FIELD OUTPUT: F-Output-3
**
*Element Output, directions=YES
E, EE, IE, LE, MISES, PE, PEEQ, PEMAG, S, STATUS, STATUSXFEM
**
** HISTORY OUTPUT: H-Output-1
**
*Output, history
*Node Output, nset=SET-1
U1,
**
** HISTORY OUTPUT: H-Output-2
**
*Node Output, nset=SET-2
RF1,
**
** HISTORY OUTPUT: H-Output-3
**
*Output, history, variable=PRESELECT
*End Step
```